

ELECTRICAL AND OPTICAL CHARACTERISTICS OF
TWO-DIMENSIONAL HETEROJUNCTION DEVICE WITH GRAPHENE

A Dissertation

Presented to the Faculty of the Graduate School
of Cornell University

In Partial Fulfillment of the Requirements for the Degree of
Doctor of Philosophy

by

Joon Young Kwak

May 2015

© 2015 Joon Young Kwak

ELECTRICAL AND OPTICAL CHARACTERISTICS OF
TWO-DIMENSIONAL HETEROJUNCTION DEVICE WITH GRAPHENE

Joon Young Kwak, Ph. D.

Cornell University 2015

As transistor scaling has slowed down at advanced technology nodes due to physical limitations of silicon based devices, new device structures such as FinFET and ultrathin body (or FDSOI) transistors have been developed to continue improving their performances. Other endeavors include devices using new materials, e.g., two-dimensional (2D) crystal materials. In the past decade, graphene based devices as well as transistors have been a great interest due to its unique electrical, mechanical and optical properties. Along with graphene research, other 2D crystal materials like transition metal dichalcogenides (TMDC), individually or in combination with graphene, have been investigated, showing other intriguing properties. This thesis is based on 2D heterostructure in combination with graphene to understand the physics behind the device in electrical and optical perspectives.

The first theme of the thesis is electrical characteristics of MoS₂-graphene heterojunction devices. Experimental results on the heterojunction device indicate a high concentration of unintentional donors in natural MoS₂ to be $3.57 \times 10^{11} \text{ cm}^{-2}$, while the ionized donor concentration is determined to be $3.61 \times 10^{10} \text{ cm}^{-2}$, which implies the presence of deep donors. The high donor concentration and the resulting high electric field near the heterojunction interface suggest that the charge transport

mechanism is thermionic-field emission in a low bias region. Based on this model, the barrier height of the graphene-MoS₂ heterojunction is determined to be 0.23 eV.

The second theme of the thesis is optical characteristics of the heterojunction devices. The results from scanning photocurrent microscopy measurements with multiple bias conditions indicate a photothermal electric (PTE) effect is the dominant mechanism for photoresponse in a graphene-MoS₂ heterojunction. The photothermal voltage generated by the PTE effect is estimated to be 0.22–0.47 mV and induces the photocurrent. Photoresponses of 0.139 mA/W and 0.019 mA/W on the graphene-MoS₂ heterojunction area are observed with and without a bias of 0.3 V, respectively, using an 800 nm wavelength laser at 0.43 mW power.

BIOGRAPHICAL SKETCH

Joon Young Kwak received his B.S. and M.Eng. degrees in Electrical and Computer Engineering from Cornell University, Ithaca NY in 2004 and 2005, respectively. He was a circuit design engineer at Samsung Electronics in Korea, where he worked on NAND Flash Memory design and Analog/Mixed signal IC design from 2005 to 2009. In 2010, he entered Cornell as a Ph.D. student in Prof. Michael G. Spencer's research group, majoring in Electrical and Computer Engineering with minoring in Materials Science and Engineering; and conducted research on two-dimensional crystal materials and devices for his doctoral dissertation. He also received his M.S. degree from Cornell ECE in 2014. He was a recipient of the Irwin Jacobs Fellowship from Cornell in 2010 and the Lester Eastman Fellowship from Cornell in 2015.

To my Family and Parents

ACKNOWLEDGMENTS

First of all, I would like to express my sincere thanks to my committee chair Prof. Michael G. Spencer for his valuable advice and support during the Ph.D. program. He provided me such a great opportunity to pursue this interesting research. Without his extensive encouragement and guidance, I could not have completed this dissertation. Also, I am very grateful to Prof. Robert B. Van Dover and Prof. Ehsan Afshari for being my committee members. I had always enjoyable and insightful discussions with them about my research and they greatly enriched my work with valuable advices.

I thank my past and present fellow group members, Jeonghyun Hwang, Brian Calderon, Brian Schutter, Hussain Alsalman, Nini Munoz, Yanxin Ji, Dorr Campbell, Shriram Shivaraman, and Troy Richards who made my Ph.D. research experience very productive. A lot of helpful resources for my research also came from fruitful discussions with them. Also, I thank Haining Wang, Bill Schaff, Moonkyung Kim, and Prof. Farhan Rana for helpful discussions. I would like to thank Matthew Graham, Kin Fai Mak, Prof. Paul McEuen and Prof. Jiwoong Park for allowing me to use their lab facilities during my research. I am also thankful for CCMR (Cornell Center for Materials Research) and CNF (Cornell NanoScale Science & Technology Facility) support staff for offering me equipment training.

I appreciate my Korean friends in ECE, Wooram Lee, Jinsub Kim, Sung Kyun Park, Juhyun Baek, June Ho Hwang, Juhyung Joe, Doyoung Kim, Sung-Yun Park,

Changhyuk Lee, Eugene Hwang, Yoon Ho Lee, Gyuhwa Jeon, and Taejoon Song who made my life at Cornell more enjoyable.

I would like to acknowledge that the work in this dissertation was supported by the CCMR (DMR-1120296) and by the CNF (Grant ECCS-0335765), all supported by the NSF (National Science Foundation).

Finally, I owe a deep debt of gratitude to my wife, Yooumi Lee, for warmest love and encouragement. Without her sincere support, I would not be able to complete my dissertation. Both my daughter, Grace Daheun Kwak, and son, James Dongwoo Kwak, always give me true happiness in my life. Special thanks to my parents and parents-in-law for their love and support for this study. Especially, I thank to my father who has never lost faith in me and always been my role model in the field of engineering.

“Trust in the Lord with all your heart and lean not on your own understanding. In all your ways submit to him, and he will make your paths straight.”

Proverbs 3:5-6

TABLE OF CONTENTS

Biographical Sketch	v
Acknowledgements	vii
Table of Contents	ix
List of Figures	xii
List of Tables	xiv
1. Introduction	1
1.1. Motivation	1
1.2. Organization of the Thesis	2
1.3. Two-Dimensional Materials: Graphene and MoS ₂	3
1.3.1. Material properties	3
1.3.1.1. Structure and Bandgap	3
1.3.1.2. Electrical properties	5
1.3.1.3. Optical properties	6
1.3.2. Production methods of graphene and MoS ₂	7
1.3.2.1. Exfoliation method	7
1.3.2.2. Chemical vapor deposition method	8
1.3.2.3. Epitaxial growth method	8
1.3.3. Applications of graphene and MoS ₂	10
1.3.3.1. Graphene applications	10
1.3.3.2. MoS ₂ applications	12
1.4. Summary	12
2. Two-Dimensional Materials Transfer, Characterization, and Molybdenum Disulfide Absorption Coefficient	13
2.1. Introduction	13
2.2. Transfer methods of 2D materials	14
2.2.1. Exfoliation method	14
2.2.2. Thermal release tape method	15
2.2.3. Wet etching method	17
2.3. Characterization tools	19
2.3.1. Raman spectroscopy	19
2.3.1.1. Introduction	19
2.3.1.2. Raman peaks of a transferred graphene grown on Cu to a silicon wafer	21
2.3.1.3. Raman peaks of an exfoliated MoS ₂ flake	22
2.3.2. Atomic Force Microscope (AFM)	23
2.3.2.1. Introduction	23
2.3.2.2. AFM measurement results on exfoliated MoS ₂ flakes	24
2.3.2.3. AFM artifacts	25
2.3.3. Transmission Electron Microscopy (TEM)	28
2.3.3.1. Introduction	28

2.3.3.2. TEM imaging results on a single layer graphene	28
2.3.3.3. Graphene sample preparation for TEM	29
2.4. Absorption coefficient of MoS ₂	30
2.4.1. Raman spectra of several MoS ₂ flakes and their colors	31
2.4.2. Distance between the MoS ₂ Raman peaks (E _{2g} ¹ and A _{1g})	33
2.4.3. Estimation of MoS ₂ absorption coefficient	35
2.5. Summary	37
3. Device Fabrication using Two-Dimensional Materials	38
3.1. Introduction	38
3.2. Device fabrication process	39
3.2.1. Sample preparation	39
3.2.2. Mask design and fabrication	40
3.2.3. Drain and source metal contacts formation	42
3.2.4. Transistor channel formation	44
3.2.5. Global back gate metal contact formation	45
3.2.6. Gate dielectric deposition	45
3.2.6.1. Challenges for top gate dielectric deposition	46
3.2.6.2. High-k dielectric deposition	47
3.2.7. Top gate metal contact formation	48
3.2.8. Device annealing	49
3.2.9. List of CNF tools used for the device fabrication	49
3.3. Two-dimensional material based transistors	51
3.3.1. Graphene transistor	51
3.3.2. MoS ₂ transistor	55
3.4. Summary	57
4. Electrical Characteristics of Multilayer Molybdenum Disulfide-Graphene Heterojunction Device	59
4.1. Introduction	59
4.2. Device structure and fabrication	60
4.3. Device characterization	63
4.4. Current-Voltage characteristics	65
4.5. Energy band diagrams and One-dimensional FET model	67
4.5.1. Energy band diagrams	67
4.5.2. Background donor density	68
4.5.3. One-dimensional FET model for back gate modulation	69
4.6. Ionized mobile charge density	70
4.7. Two donor levels model	71
4.8. Charge transport mechanism	74
4.8.1. Energy band diagram on each junction	74
4.8.2. Channel Resistance vs. Schottky Barrier Resistance	77
4.8.3. Schottky barrier heights on each junction	79
4.8.3.1. Method 1 (Thermionic emission model)	79
4.8.3.2. Method 2 (Thermionic field emission model)	81

4.8.3.3. Thermionic emission model versus thermionic field emission model	83
4.9. Effect of changing ground contact location	83
4.10. Summary	84
5. Optical Characteristics of Molybdenum Disulfide-Graphene Heterojunction Device	85
5.1. Introduction	85
5.2. Device and fabrication	86
5.3. Optics setup	88
5.4. Measurement Results	90
5.4.1. Current-voltage measurement	90
5.4.2. Spatial resolution photoresponse measurement	91
5.4.3. Bias dependent photoresponse measurement	93
5.5. Analysis and discussion	94
5.5.1. Generated voltages by the PTE effect	94
5.5.2. Photocurrent gain by PTE effect	97
5.6. Summary	99
6. Summary	100
Bibliography	102

LIST OF FIGURES

1.1. Crystal structures of graphene and MoS ₂	4
1.2. Electronic band structures of graphene and MoS ₂	4
1.3. Ambipolar characteristics of graphene	6
1.4. Absorption spectra of graphene and MoS ₂	7
1.5. Epitaxial graphene growth on the Si face	9
1.6. RF performance of graphene devices based on CVD graphene and epitaxial graphene	10
1.7. Comparison of transmittance and sheet resistance of various transparent electrodes	11
2.1. Optical microscope view of exfoliated MoS ₂ flakes on target substrates	15
2.2. Optical microscope view of a transferred graphene grown on a Sapphire wafer to a SiO ₂ /Si wafer	17
2.3. Wet etching transfer process	19
2.4. Image of a Raman spectroscopy for identifying materials, in the Cornell Center for Materials Research (CCMR)	20
2.5. Raman spectrum of a transferred graphene grown on Cu to SiO ₂ /Si wafer	21
2.6. Raman spectrum of a MoS ₂ flake exfoliated from a natural chunk of bulk material	22
2.7. Image of an atomic force microscope (AFM) for measuring thickness and surface topography of materials, in the Cornell NanoScale Science & Technology Facility (CNF)	23
2.8. AFM images and profiles of exfoliated MoS ₂ flakes	25
2.9. AFM images with and without a tip artifact on the same sample	27
2.10. TEM images of a monolayer graphene	29
2.11. Images of TEM grids	30
2.12. Raman spectra of several exfoliated MoS ₂ flakes	32
2.13. Plot of peak distance of two MoS ₂ Raman peaks, E _{2g} ¹ and A _{1g} versus number of MoS ₂ layers	33
2.14. AFM measurement results of another set of MoS ₂ flakes	34
2.15. Plot of the change of the silicon Raman peak intensity ratio versus number of MoS ₂ layers	35
3.1. Image of one of the mask designs for 2D device fabrications	41
3.2. Comparison of the two photolithography processes for metal deposition	43
3.3. Raman spectra of graphene after SiO ₂ deposition using PVD methods ..	46
3.4. Schematic cross section of the fabricated 2D transistor	49
3.5. Optical microscope image of a fabricated top-gated graphene transistor	52

3.6.	Current-voltage curves of a top-gated graphene transistor with Al_2O_3	53
3.7.	Current-voltage curves of a top-gated graphene transistor with HfO_2	54
3.8.	Optical microscope image of a fabricated back-gated MoS_2 transistor	56
3.9.	Current-voltage curves of a back-gated MoS_2 transistor on SiO_2	57
4.1.	Device structure of a MoS_2 -graphene heterojunction device	61
4.2.	Heterojunction device fabrication process steps	62
4.3.	Raman and AFM characterization results	64
4.4.	Current-voltage curves ($I_{\text{DS}}-V_{\text{DS}}$ and $I_{\text{DS}}-V_{\text{GS}}$) of a back-gated heterojunction device with 80 nm thick MoS_2 on 100 nm thick SiO_2 at room temperature	66
4.5.	Energy band diagrams with different back gate bias conditions	67
4.6.	Transfer characteristic curves ($I_{\text{DS}}-V_{\text{GS}}$) in semi-logarithmic scale of a 8 nm thickness of MoS_2 -graphene hetero-junction devices on 50 nm thickness of high-k dielectric Al_2O_3 deposited at $V_{\text{DS}} = 2 \text{ V}$	69
4.7.	One-dimensional FET model to describe the change of channel depth by a back gate bias with a V_{DS} applied	70
4.8.	Two donor levels from temperature dependent measurement	71
4.9.	Graph of electron concentration (n) and hole concentration (p) versus Fermi energy relative to Dirac energy	73
4.10.	Energy band diagram model at the graphene- MoS_2 interface	74
4.11.	Energy band diagrams with different drain bias conditions	75
4.12.	Log-Log scale plots of $I_{\text{DS}}-V_{\text{DS}}$ in reverse bias conditions (at $V_{\text{GS}} = 0 \text{ V}$) with graphene or MoS_2 grounded	76
4.13.	Plot for total resistance vs. V_{DS} at a fixed $V_{\text{GS}} = 0 \text{ V}$ with different temperatures (120K-400K with 40K step)	78
4.14.	The Arrhenius plots for the barrier height extractions using thermionic emission model (Method 1) at $V_{\text{DS}} = -0.1 \text{ V}$	80
4.15.	The Arrhenius plots for the barrier height extractions using thermionic field emission model (Method 2) at $V_{\text{DS}} = -0.1 \text{ V}$	82
5.1.	Device structure and characterization results of a graphene- MoS_2 heterojunction device	87
5.2.	Optics setup for photoresponse measurements	89
5.3.	Current-Voltage curves ($I_{\text{DS}}-V_{\text{DS}}$) of the back gated heterojunction device at room temperature	90
5.4.	Photoresponse maps on the heterojunction area with the raster laser scan (800 nm wavelength at 0.43 mW) with different biases applied	92
5.5.	V_{DS} dependent photoresponse curves with a stationary laser illumination on each junction at $V_{\text{GS}} = 0 \text{ V}$	93
5.6.	Photothermal voltages generated at each junction by the photothermal electric (PTE) effect	96

LIST OF TABLES

2.1. Characterization results of each MoS ₂ flakes from AFM and Raman spectroscopy	36
2.2. Calculations of MoS ₂ absorption coefficient for each flake	37
3.1. List of CNF tools used for the device fabrication	50
4.1. Estimated total ionized mobile carrier density for different temperatures	71
4.2. The calculated ionized mobile carrier density from each donor level using Fermi-Dirac (F-D) statistics for different temperatures	72

CHAPTER 1

INTRODUCTION

1.1 Motivation

As Moore's law approaches the physical limitations of silicon based devices, many efforts such as FinFET and Fully Depleted Silicon-on-Insulator (FDSOI) devices have been introduced to keep improving their performances. In addition, other endeavors have been exploring devices using new materials. One of the promising candidates for the new materials is graphene.

Graphene is a one-atom-thick layer of carbon atoms with a honeycomb crystal lattice structure. In 1946, a band theory of graphite by Wallace [1] suggested that electrical conductivity within the plane might be 100 times greater than that across planes. In 2004, the prediction was proved by Novoselov and Geim from the Manchester group with a simple method of isolating graphene from graphite [2]. In 2010, they received the Nobel Prize in physics for their work on graphene. The method of isolating a two-dimensional (2D) layered material from a three-dimensional (3D) bulk material, the "Scotch tape method," opens other 2D layered materials research, e.g., transition metal dichalcogenides (TMDC) like molybdenum disulfide (MoS_2). Along with the individual 2D material researches, heterostructures in combination with different 2D materials have recently emerged and been investigated, showing other intriguing properties for electronic applications, such as a field-effect tunneling transistor that shows an ON/OFF ratio of over 10^6 at room temperature [3].

Because research on the heterostructures using TMDC materials and graphene is a very new area, the physics behind these devices has not yet been fully understood. Therefore, in-depth understanding of properties of the 2D heterostructures is crucial for driving actual applications. In this thesis, two major themes are studied regarding the 2D heterostructures: specifically, (1) Electrical properties and (2) Optical properties of graphene-MoS₂ heterojunction devices.

1.2 Organization of the Thesis

This thesis is organized as follows. To get an idea of what the 2D materials are, chapter 1 provides introductory background into graphene and MoS₂. Once the 2D materials are ready for performing research, the first step is to transfer them onto a target substrate and to understand the quality of the materials. Therefore, chapter 2 provides the 2D materials transfer and characterization methods and their results. Extraction of MoS₂ absorption coefficient is also described. Then the next step is to fabricate devices with the 2D materials. Chapter 3 outlines device fabrication processes for the 2D materials with two examples; graphene transistors and MoS₂ transistors. Knowing how to fabricate the 2D devices, graphene-MoS₂ heterojunction devices are fabricated. Chapter 4 investigates electrical properties of the graphene-MoS₂ heterojunction devices using a temperature-dependent electrical characterization method. Chapter 5 studies optical properties of the graphene-MoS₂ heterojunction devices by measuring photoresponses using a scanning photocurrent microscopy. Chapter 6 offers a summary of the thesis.

1.3 Two-Dimensional Materials: Graphene and MoS₂

1.3.1 Material properties

To perform research on the graphene-MoS₂ heterostructure, it is necessary to understand the properties of graphene and MoS₂. In this section, some of their important electrical and optical properties are reviewed.

1.3.1.1 Structure and Bandgap

The crystal structures of graphene and MoS₂ are shown in Figure 1.1. They both have hexagonal honeycomb lattice structures. Graphene is formed by an atomic layer of carbon atoms and MoS₂ is formed by two different atoms, molybdenum (Mo) and sulfur (S), where Mo atoms are sandwiched between S atoms. Each graphene layer and MoS₂ layer stacks to form graphite and bulk MoS₂, respectively, bound by van der Waals forces. The thickness of graphene is about 0.34 nm [4] and the interlayer spacing for MoS₂ is about 0.65 nm [5].

Electronics band structures of graphene and MoS₂ are illustrated in Figure 1.2. Graphene has a linear energy dispersion relation near the Dirac point where the conduction and valance bands meet, i.e., graphene has a zero gap [6]. The energy band structures of MoS₂ also show interesting results. Monolayer MoS₂ has a bandgap of 1.9 eV (direct), while bulk MoS₂ has a bandgap of 1.2–1.3 eV (indirect) [7-9]. The direct gap of monolayer MoS₂ opens up possible optical applications, e.g., light emitting diodes, due to strong interaction with light [10, 11].

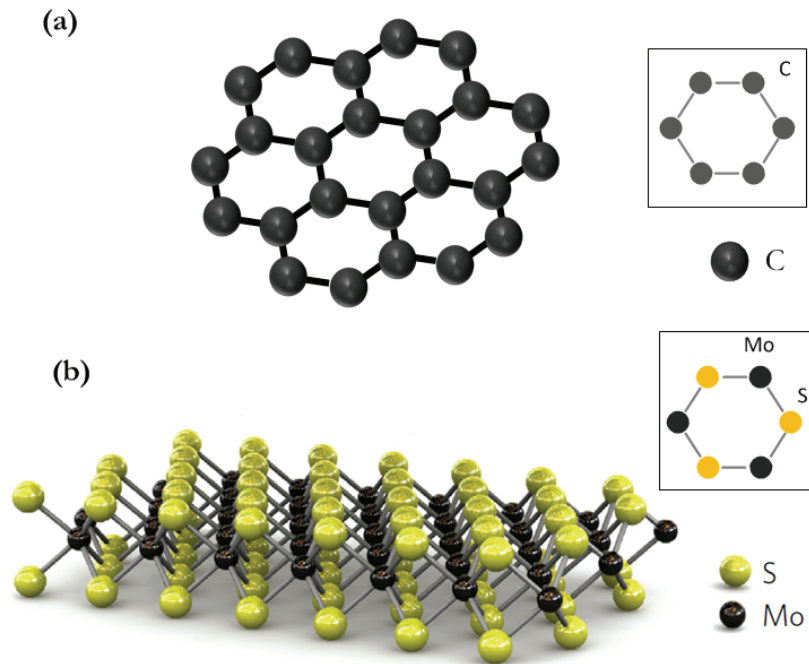


Figure 1.1: Crystal structures of graphene and MoS₂. (a) Atomic structure of graphene. Inset shows the hexagonal lattice of graphene. (b) Atomic structure of MoS₂. Inset shows the hexagonal lattice of MoS₂. Adapted from [5].

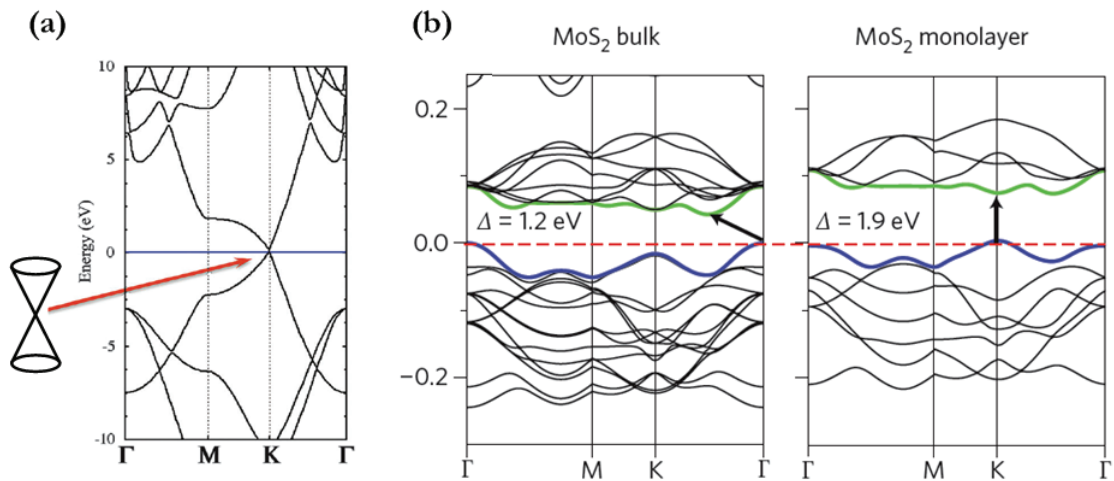


Figure 1.2: Electronic band structures of graphene and MoS₂. (a) Graphene band structure with a Dirac cone shown on the left. Graphene has a linear dispersion near the Dirac cone and has a zero gap. Adapted from [12]. (b) MoS₂ band structure for bulk and monolayer, respectively. Bulk MoS₂ has a bandgap of 1.2–1.3 eV and monolayer MoS₂ has a bandgap of 1.9 eV. Adapted from [7].

1.3.1.2 Electrical properties

Graphene is known to have an ultrahigh mobility that exceeds 200,000 cm^2/Vs in suspended graphene [4]. Carrier mobilities of $\sim 60,000 \text{ cm}^2/\text{Vs}$ [13] and $\sim 40,000 \text{ cm}^2/\text{Vs}$ [14] are reported in the literature for graphene on boron nitride (hBN) and graphene on SiO_2 , respectively. The mobility degradation of graphene from the suspended graphene to graphene on a substrate is mostly attributed to scattering by charged impurities and by surface phonons at the substrate [14]. Graphene exhibits ambipolar transport behavior as shown in Figure 1.3 [15]. For intrinsic graphene, the Fermi level is located at the Dirac point, where the graphene resistance reaches a maximum. The Fermi level of graphene is shifted by a gate bias, resulting in the graphene resistance change. In a positive gate bias, the Fermi level is shifted up from the Dirac point, i.e., electrostatically doped with electrons. On the other hand, in a negative bias, the Fermi level is shifted down from the Dirac point, i.e., electrostatically doped with holes.

MoS_2 mobilities are reported to be 0.1-10 cm^2/Vs for a monolayer MoS_2 on SiO_2 substrate and $\sim 200 \text{ cm}^2/\text{Vs}$ for a monolayer MoS_2 on hafnium oxide (HfO_2) substrate [5]. The improvement in mobility by changing the substrate from SiO_2 to HfO_2 is possibly due to suppression of Coulomb scattering by the high-k dielectric [16]. While a graphene device cannot be turned off due to the zero bandgap, a MoS_2 transistor shows an extremely high current ON/OFF ratio that exceeds 10^8 [5].

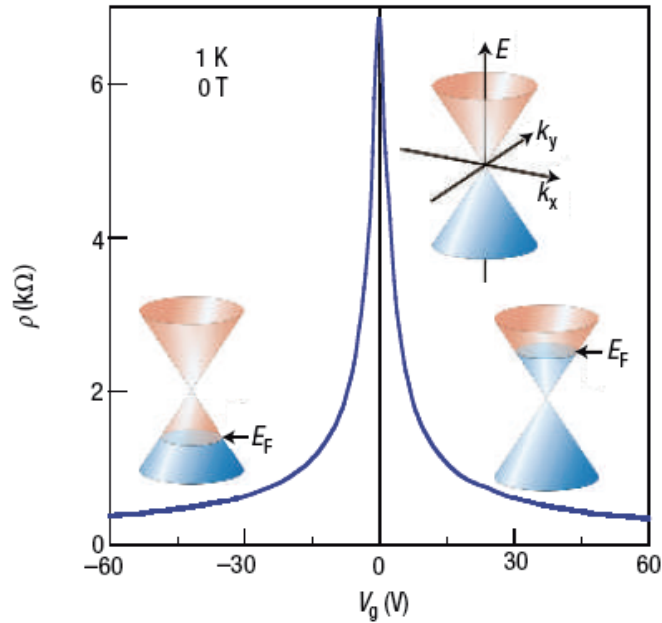


Figure 1.3: Ambipolar characteristics of graphene. A gate bias controls the Fermi level of graphene to reduce the graphene resistance. Adapted from [15].

1.3.1.3 Optical properties

Figure 1.4 shows the absorption spectra of graphene and MoS₂. Graphene has an absorption of 2.3% per layer and the absorption spectrum is flat from 300 to 2,500 nm, which is a consequence of the unique electronic band structure of graphene [17, 18]. Unlike the graphene case, MoS₂ has limited absorption spectra due to its bandgap. The absorption drops when the photon energy is less than the bandgap of about 1.8 eV and 1.3 eV for thin layer and thick layer MoS₂, respectively, as shown in the figure.

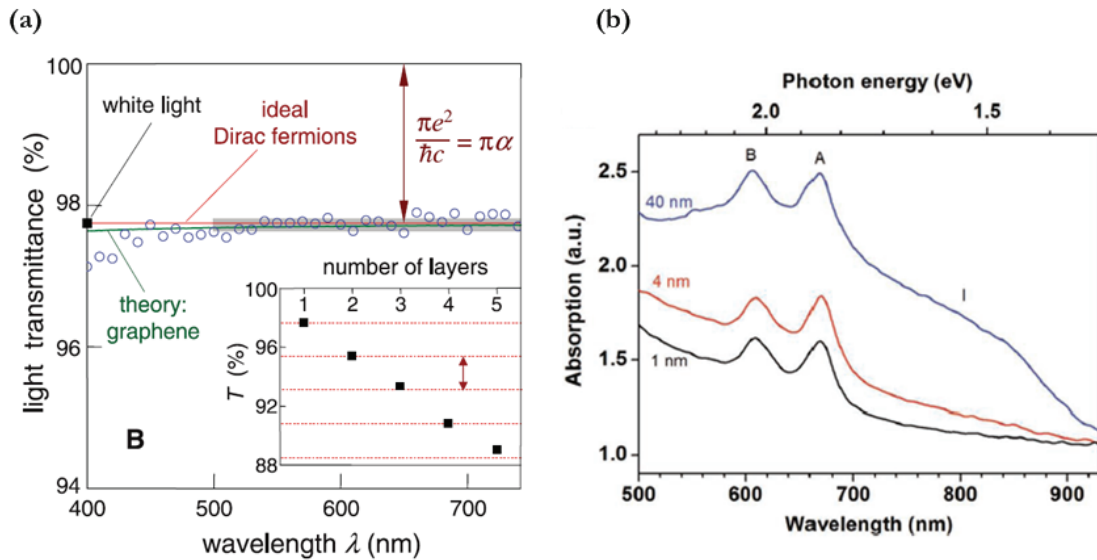


Figure 1.4: Absorption spectra of graphene and MoS₂. (a) Transmittance spectrum of single layer graphene. Inset shows the spectrum as a function of the graphene number of layer. Adapted from [17]. (b) Absorption spectra of MoS₂ with three different thicknesses. Adapted from [19].

1.3.2 Production methods of graphene and MoS₂

How are the 2D materials produced? To answer the question, three common production methods—exfoliation, chemical vapor deposition, and epitaxial growth—are discussed in this section.

1.3.2.1 Exfoliation method

This method involves a mechanical cleavage technique using Scotch tape introduced by the Manchester group [2]. Atomically thin 2D materials are obtained by repeatedly peeling off the 3D materials, i.e., graphite and natural chunk of crystal MoS₂. This method gives single crystal high quality monolayer flakes for fundamental research purposes. However, a disadvantage of the exfoliation method

is low yield, and it is impractical for large scale applications.

1.3.2.2 Chemical vapor deposition method

Large area graphene has been grown on various metal substrates, such as copper [20, 21] and nickel [22] foils, using the chemical vapor deposition (CVD) method. CVD graphene on copper is processed under the deposition temperature of 1000 °C in a low pressure (0.5 Torr) of methane (CH₄) and hydrogen (H₂) gas mixture [20]. Different process conditions like temperatures of 800–950 °C and atmospheric pressures for CVD graphene on copper have been attempted and reported as well [23]. A higher process temperature and a lower pressure tend to produce a larger coverage of monolayer graphene on copper. Since graphene grown on a metal foil requires a graphene transfer process on an insulating substrate, direct graphene growths on insulating substrates, such as sapphire and SiO₂, have been also studied [24-26].

Several growth methods of MoS₂ on SiO₂ using different precursors have been reported. Some common precursors used for the MoS₂ growths are ammonium thiomolybdate solution ((NH₄)₂MoS₄) [27], pre-deposited molybdenum (Mo) metal [28], and molybdenum trioxide (MoO₃) powder [29-31]. Large area 2D materials are easily produced by the CVD method; however, the quality of the materials is not yet comparable to the exfoliated materials.

1.3.2.3 Epitaxial growth method

This is another approach for a large area graphene production on SiC substrate. High temperature (1300–1600 °C) annealing causes sublimation of the silicon atoms and

leaves the carbon atoms behind. The carbon atoms are self-assembled into graphene. SiC has two faces; SiC(0001) surface (or the Si face) and SiC(000 $\bar{1}$) surface (or the C face). It is observed that the Si face provides a layer-by-layer graphene growth, while the C face more resembles a three dimensional type of growth. This is because the sublimation of the silicon atoms happens much faster for the C face than for the Si face. Thicker graphene films are formed on the C face than on the Si face under the same growth condition [32, 33]. As a result, the epitaxial graphene growth is preferred on the Si face.

For the graphene grown on the Si face, an interface layer exists between graphene and the SiC. This interface layer is known by several names: $6\sqrt{3}\times 6\sqrt{3}R30^\circ$ reconstructed layer, zero-layer, or buffer layer. Figure 1.5 shows the buffer layer located in between graphene and the SiC.

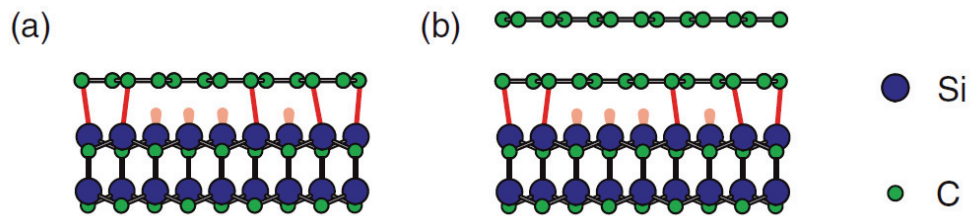


Figure 1.5: Epitaxial graphene growth on the Si face. A buffer layer is presented between graphene and the SiC. Adapted from [34]. (a) The buffer layer is covalent bonded to the Si atoms. (b) Epitaxial graphene is grown on the buffer layer for the Si face.

The covalent bonds between the buffer layer and the Si atoms can be removed by hydrogen intercalation [34]. After the buffer layer is decoupled from the SiC substrate by the hydrogen intercalation process, it becomes another layer of graphene.

1.3.3 Applications of graphene and MoS₂

Although the zero gap of graphene and the low mobility of MoS₂ are the major drawbacks of each material for taking over current silicon-based electronics in industry, there are possible applications that take unique advantages of the 2D materials. This section briefly discusses potential applications of the 2D materials.

1.3.3.1. Graphene applications

One of the potential applications of graphene is radio frequency (RF) applications using the graphene's ultrahigh carrier mobility and the ambipolar transport properties. Sample RF circuit components, e.g., frequency mixer, frequency multiplier, and frequency modulator, have been demonstrated [35-38].

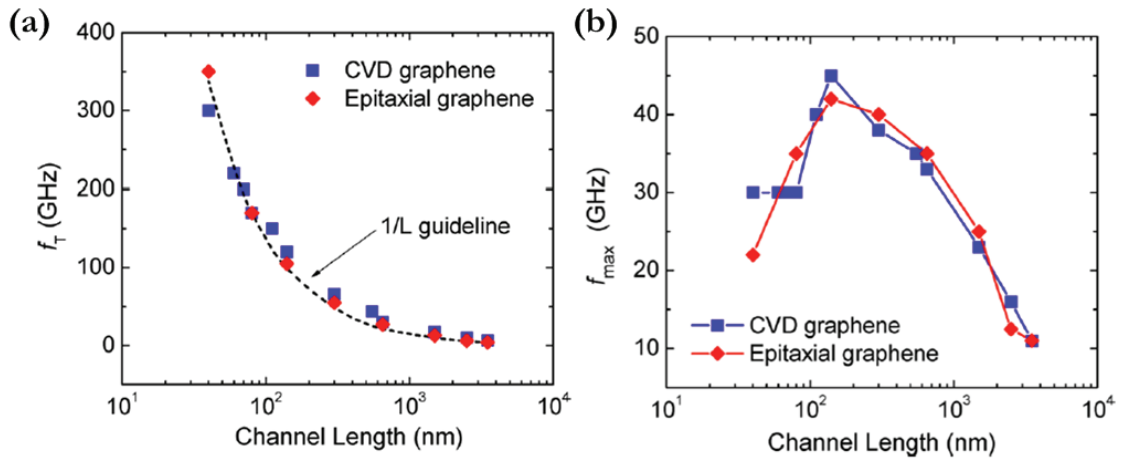


Figure 1.6: RF performance of graphene devices based on CVD graphene and epitaxial graphene. Adapted from [39]. (a) Cutoff frequency as a function of device channel length. f_T of over 300 GHz are demonstrated for both CVD graphene and epitaxial graphene. (b) Maximum oscillation frequency as a function of device channel length. f_{max} of over 40 GHz are demonstrated for both CVD graphene and epitaxial graphene.

A cutoff frequency (f_T) exceeding 300 GHz and a maximum oscillation frequency (f_{max}) exceeding 40 GHz for RF devices based on CVD graphene and epitaxial graphene have been reported (Figure 1.6) [39-41].

Another potential application of graphene is transparent flexible electrodes for various applications like touch panels and neuroimaging [42-45]. Two important requirements for a transparent electrode are high optical transmittance and low sheet resistance. Figure 1.7 shows comparison graphs of different types of transparent electrodes [46]. Graphene electrodes have higher transmittance over a broad spectral range compared to other electrodes, such as indium tin oxide (ITO). Also, the sheet resistances of graphene electrodes are comparable to ITO although the graphene electrode thicknesses are much thinner than any other electrodes. Therefore, high transparency, low reflectance, and high carrier mobility make graphene a promising transparent electrode.

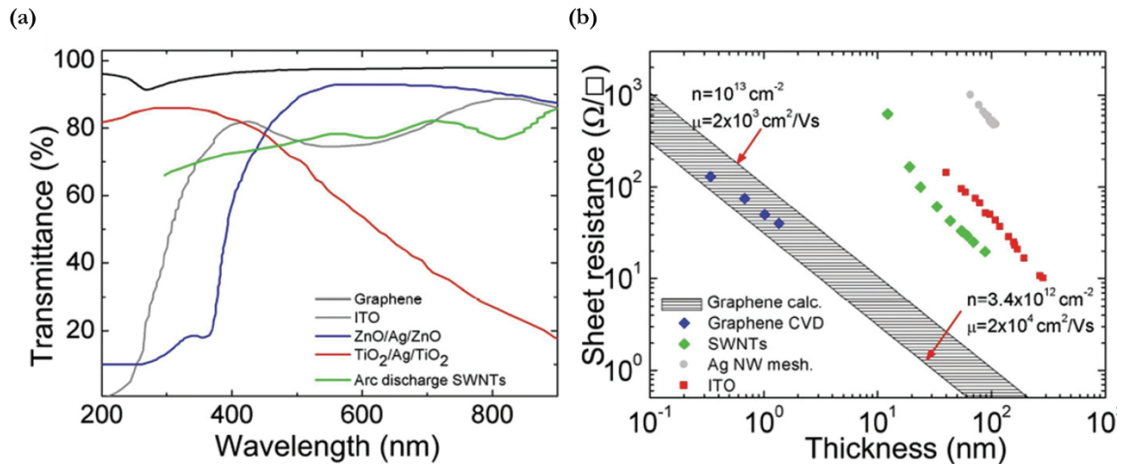


Figure 1.7: Comparison of transmittance and sheet resistance of various transparent electrodes. Adapted from [46]. (a) Transmittance versus wavelength graph. Graphene shows the highest transmittance over a broad spectral range. (b) Sheet resistance versus thickness graph. Graphene sheet resistances are comparable to the sheet resistances of the other electrodes, while the graphene electrode thickness is the thinnest among them.

1.3.3.2. MoS₂ applications

Since MoS₂ has a bandgap and a high current ON/OFF ratio, it has a potential to substitute for conventional silicon based electronics while sharing many advantages of graphene like transparency and flexibility [47]. Several electronic circuits, e.g., logic inverter, NAND gate, NOR gate, SRAM cell, and ring oscillator, have been demonstrated [48-51]. The direct bandgap of MoS₂ also opens many possible optoelectronic applications. Some examples of the optical devices, e.g., solar cells, light emitting diodes, photodetectors, have been demonstrated [10, 11, 52-55].

1.4 Summary

So far, a brief introduction on the 2D materials (graphene and MoS₂) and their potential applications has been discussed. The first part of the chapter introduced the electrical properties of graphene and MoS₂ followed by the optical properties of the materials. Graphene has an ultrahigh mobility, while it has a zero gap. On the other hand, MoS₂ has a bandgap and its device shows a very high current ON/OFF ratio. However, the mobility of MoS₂ is much lower than the mobility of graphene. The second part of the chapter summarized three common methods of producing the 2D materials: mechanical exfoliation, chemical vapor deposition (CVD), and epitaxial methods. The last part of the chapter discussed some potential applications of graphene and MoS₂. The potential applications using graphene include RF circuits and transparent flexible conductive electrode. The potential applications using MoS₂ include electronic circuits and optoelectronic devices.

CHAPTER 2

TWO-DIMENSIONAL MATERIALS TRANSFER, CHARACTERIZATION, AND MOLYBDENUM DISULFIDE ABSORPTION COEFFICIENT

2.1 Introduction

In year 2004, graphene was successfully isolated from graphite by Geim's group in Manchester [2] by an exfoliation method using Scotch tape. Since then researchers have been working on growing graphene directly on many different substrates such as Cu foil [20, 56-58] for a large area graphene. Research on MoS₂ devices was also started with the exfoliation method [5]. Since then, researches on large area MoS₂ growth have become popular for practical fabrication of devices for real world applications [59]. To perform research on physical and chemical properties of 2D materials, it is essential to properly transfer the materials to a target substrate like a SiO₂/Si wafer unless they are directly grown on an insulator [25]. In addition to the transfer process, characterization processes are required to confirm the existence and the quality of the transferred materials on the target substrate. With the results obtained from the characterization processes, MoS₂ absorption coefficient is extracted.

This chapter begins with a brief discussion of three popular transfer methods and their results. Two-dimensional materials characterization methods are discussed next. Finally, an extraction of molybdenum disulfide (MoS₂) absorption coefficient based on the characterization results is presented.

2.2 Transfer methods of 2D materials

Three popular transfer methods are discussed in the following. The first is an exfoliation method using Scotch tape; the second method is a thermal release tape method; and the last one is a wet etching method.

2.2.1 Exfoliation method

An exfoliation method, which is also known as the Scotch tape method, uses a piece of normal Scotch tape to obtain an atomically thin material by peeling off from a bulk material. The process for the exfoliation is as follows:

1. Prepare a piece of Scotch tape and bulk graphite or a natural chunk of MoS₂.
2. Attach the tape onto the bulk and gently press it with a smooth surface like an ending portion of a diamond scribe handle.
3. Slowly peel the tape off from the bulk from one edge of the tape to the other.
4. Attach the peeled off tape to a target substrate.
5. Gently press it as described in step 2.
6. Slowly peel the tape off from the substrate.
7. Verify the thicknesses of flakes using characterization tools like Atomic Force Microscope (AFM), Raman Spectroscopy, and an optical microscope. This verification process will be discussed later in more detail.

The size of the obtained material flake generally varies from 10 μm^2 to 10000 μm^2 . The thickness of the flakes also has a large variation, from monolayer to several hundred layers. Experimentally, a smaller size flake has a thinner thickness. Figure

2.1 shows some optical images of the MoS₂ transfer results using the exfoliation method.

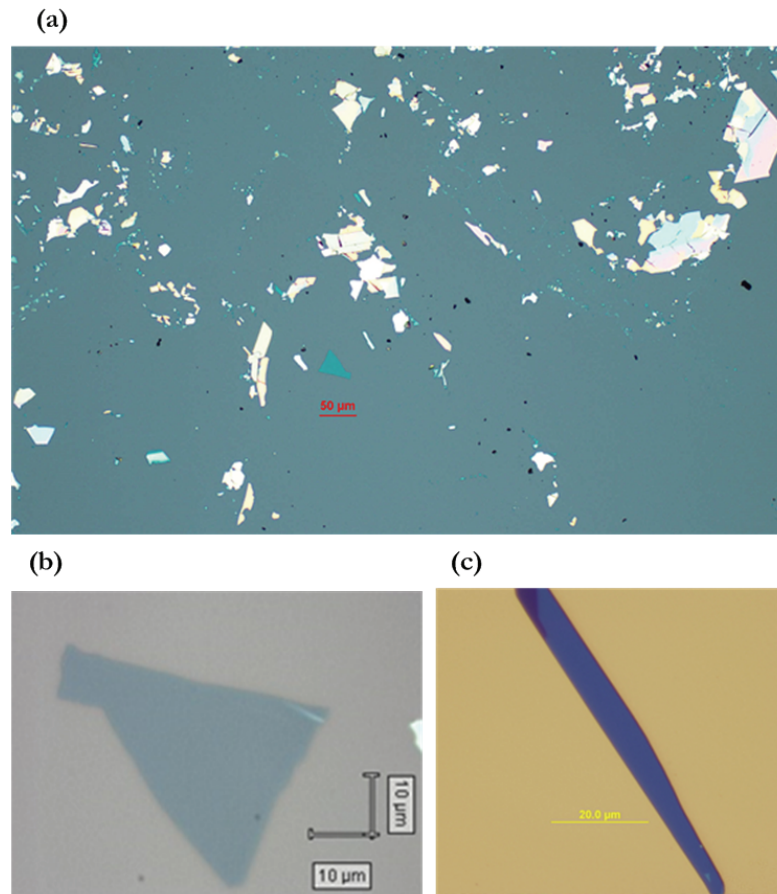


Figure 2.1: Optical microscope view of exfoliated MoS₂ flakes on target substrates. (a) A large area view of a surface after exfoliation. (b,c) Magnified view of exfoliated MoS₂ flakes.

2.2.2 Thermal release tape method

This method uses a special tape that loses its adhesion when it is heated. Unlike the Scotch tape method used for transferring flakes from a bulk material, this method is used for a large area transfer from a grown material, e.g., graphene grown on a Cu foil

or graphene grown on a sapphire wafer. The processing steps for the thermal release tape method are as follows:

1. Prepare a piece of thermal release tape and graphene grown on a substrate.
2. Deposit a gold layer on the graphene with an ebeam evaporator (100 nm).
3. Gently press the tape onto the Au/graphene stack for 1 minute.
4. Slowly peel the tape off from the substrate surface.
5. Gently press the peeled off tape to a target substrate.
6. Place it on a hot plate that is set to temperature 180°C for more than 1 minute.
7. Once the tape loses its adhesion to the Au/graphene, remove the tape from the target substrate.
8. Remove the Au with a gold etchant.
9. Clean the surface with DI water.
10. Verify the material with an Atomic Force Microscope (AFM), a Raman Spectroscopy, and an optical microscope.

This method provides a high quality large area of graphene coverage; however, often the transferred graphene is not continuous. Two common reasons why it is not easy to obtain a continuous graphene film are: 1) an uneven force made over the tape surface when pressing on the Au/graphene stack; and/or 2) some non-uniform stress distributions occurring on the Au/graphene stack due to a small bending of the tape when peeling it off from the surface. Figure 2.2 shows an optical image of the graphene transfer results using the thermal release tape method.

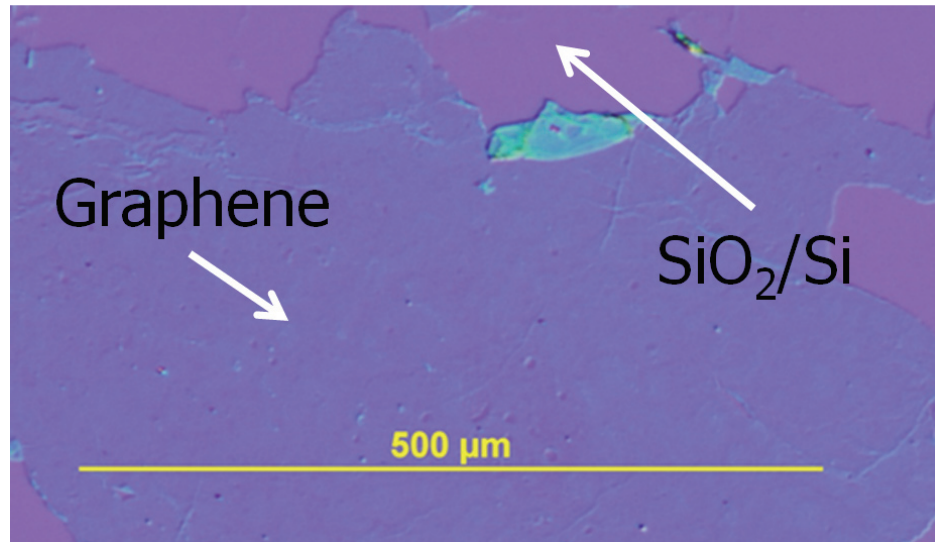


Figure 2.2: Optical microscope view of a transferred graphene grown on a Sapphire wafer to a SiO₂/Si wafer.

2.2.3 Wet etching method

To date, the most popular graphene for research is a CVD grown graphene on a copper foil because it is an easy and cheap way to obtain a large area monolayer graphene. In consequence, the wet etching method has become the most popular method for transferring a large area graphene or other 2D materials grown on a metal foil. It provides a continuous large area graphene on any types of target substrates. On the other hand, if the transfer process is not carefully performed, it sometimes brings up an issue regarding contamination of the 2D material because a polymer (polymethyl methacrylate, PMMA) and a couple of chemical acids are involved during the process. The process for the wet etching method is as follows:

1. Spin a thin layer of PMMA onto the graphene on Cu. (Spin it with 2500 rpm for 45 seconds).

2. Place it on a hot plate at 170°C for 2 minutes for curing the PMMA.
3. Remove the graphene from the opposite side of the copper foil if necessary using oxygen plasma etching.
4. Etch the copper by floating the foil on a Cu etchant (HCl/FeCl₃). Although the foil is fully etched within 1 hour, more than 2 hours are desired to make sure to etch the copper completely.
5. Scoop the PMMA/graphene stack with a temporary substrate and transfer it to DI water. Float it for at least 4 hours per DI water rinse.
6. Transfer the stack to a couple of successive DI water rinses to thoroughly remove the Cu etchant residue.
7. Scoop the PMMA/graphene stack to a target substrate.
8. Dry it in air for 1 day.
9. Remove the PMMA by immersing the stack in acetone for 2 hours.
10. Clean the surface with DI water.
11. Verify the material with an Atomic Force Microscope (AFM), a Raman Spectroscopy, and an optical microscope.

Figure 2.3 illustrates the change of the layer stacks during the wet etching transfer process.

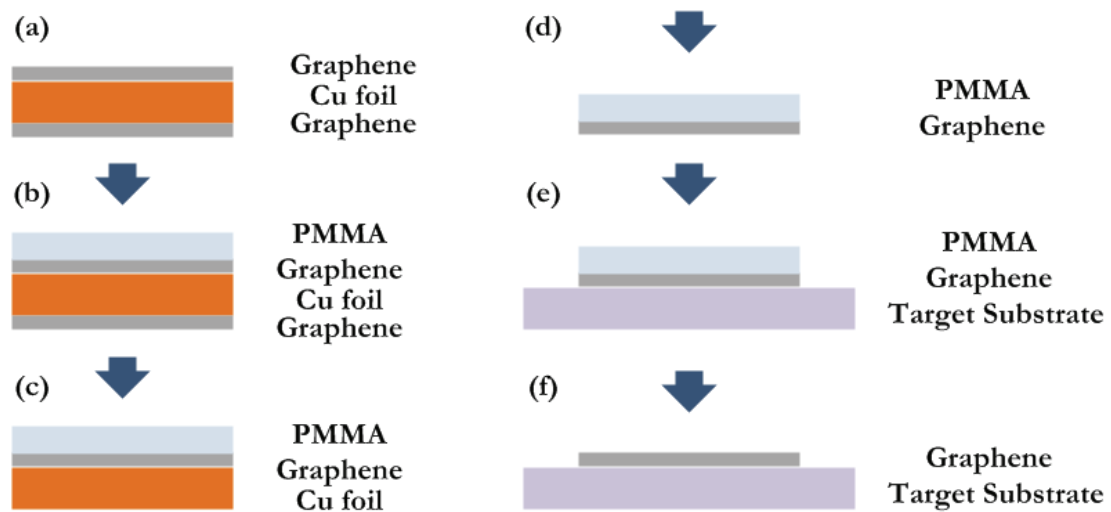


Figure 2.3: Wet etching transfer process. (a) Graphene grown on Cu. Graphene is grown on both side of copper. (b) Spin PMMA on graphene. (c) Graphene on the other side is etched by oxygen plasma etching. (d) Copper foil is etched by Cu etchant and transferred onto DI water. (e) PMMA/graphene stack is transferred onto a target substrate. (f) Remove PMMA using acetone.

2.3 Characterization tools

Two popular characterization tools are discussed first in this section: 1) Raman spectroscopy; and 2) atomic force microscopy (AFM). Another powerful characterization tool, transmission electron microscopy (TEM), will then be discussed briefly.

2.3.1 Raman spectroscopy

2.3.1.1 Introduction

Raman spectroscopy is used for identification of materials using the Raman scattering effect. Figure 2.4 shows an image of a Raman spectroscope.

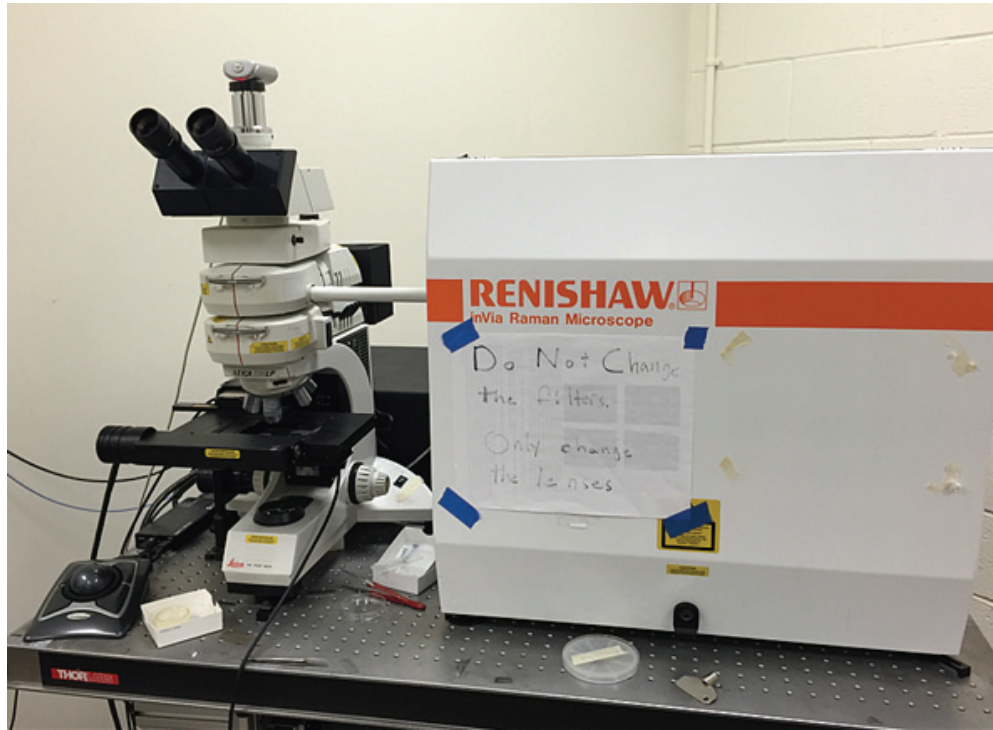


Figure 2.4: Image of a Raman spectroscope for identifying materials, in the Cornell Center for Materials Research (CCMR).

There are two types of scattering events: one is Rayleigh scattering, and the other is Raman scattering. In Rayleigh scattering photons are scattered from phonons elastically, meaning the frequency of the emitted photon remains the same as the frequency of the incident photon. On the other hand, in Raman scattering photons are scattered from phonons inelastically either by losing energy or gaining energy [60]. The energy transfer between the laser photons and the phonons changes the photons' energy state, i.e., their frequency changes. This change is called a Raman shift and it contains the information about the material. For a high efficiency 2D material Raman measurement, a laser with a wavelength of 488 nm is used with the testing material prepared on a 285 nm thickness of SiO_2/Si wafer.

2.3.1.2 Raman peaks of a transferred graphene grown on Cu to a silicon wafer

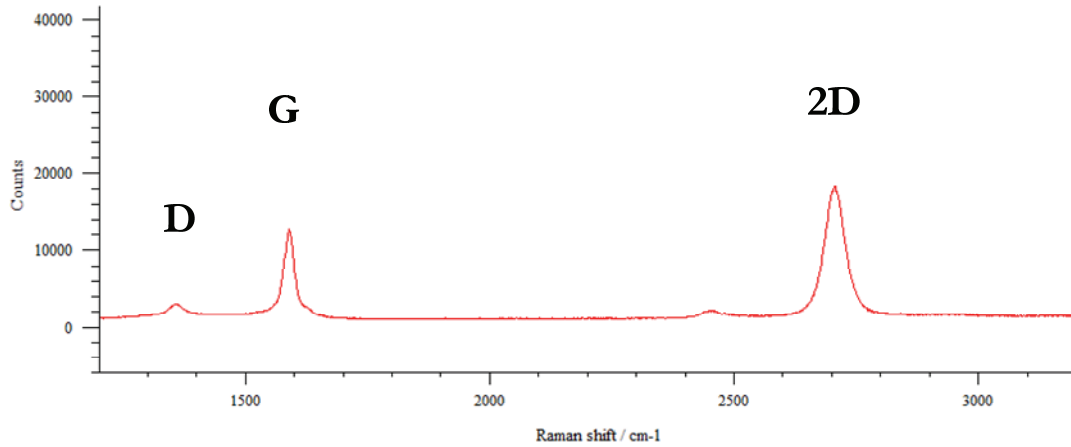


Figure 2.5: Raman spectrum of a transferred graphene grown on Cu to SiO₂/Si wafer. The D peak (1350 cm⁻¹) is activated by defects. As a result, a pristine graphene with no defects only has a G peak (1580 cm⁻¹) and a 2D peak (2700 cm⁻¹).

A Raman spectrum of graphene transferred from Cu to SiO₂/Si wafer is shown in Figure 2.5. There are three distinct Raman peaks in graphene [60]. The first peak is the D peak located at 1350 cm⁻¹ due to the breathing modes of six carbon atom rings. The D peak is also called the disorder induced D-band because it requires a defect for its activation [61]. As a result, the D peak gets smaller as less defects are present in a graphene. The second peak is the G peak located at 1580 cm⁻¹ that corresponds to an in-plane optical phonon mode. The last peak is the 2D peak located at 2700 cm⁻¹, which is the D peak overtone. Unlike the D peak, the 2D peak does not require defects for its activation and hence always appears in a graphene Raman spectrum. In general, a large single grain pristine graphene without any existing defect only has two Raman peaks, a G peak and a 2D peak, in a Raman shift.

2.3.1.3 Raman peaks of an exfoliated MoS₂ flake

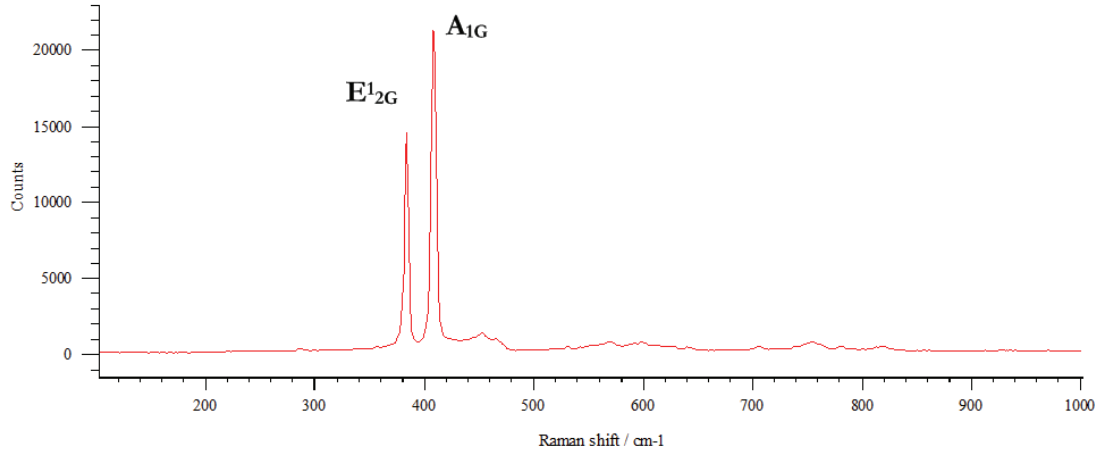


Figure 2.6: Raman spectrum of a MoS₂ flake exfoliated from a natural chunk of bulk material. The E¹_{2G} (382 cm⁻¹) peak is due to in-plane scattering mode and the A_{1G} peak (405 cm⁻¹) is due to out-of-plane scattering mode.

A Raman spectrum of an exfoliated MoS₂ from a natural chunk of bulk material is shown in Figure 2.6. There are two distinct Raman peaks in MoS₂ [62, 63]. The first peak is an E¹_{2G} peak located at around 382 cm⁻¹. The E¹_{2G} peak is due to an in-plane inelastic phonon scattering event. The second peak is an A_{1G} peak located at around 405 cm⁻¹. The A_{1G} peak is due to an out-of-plane inelastic phonon scattering event. The distance between the E¹_{2G} peak and the A_{1G} peak is one of the indicators for determining the MoS₂ thickness. As the thickness increases, the distance between the peaks becomes wider and is saturated at certain thickness. More details of this will be discussed later.

2.3.2 Atomic Force Microscope (AFM)

2.3.2.1 Introduction

An atomic force microscope (AFM) is used to confirm a thickness and a surface topography of materials. It is a type of scanning probe microscope with a very high resolution on the order of sub-nanometers. There are two operation modes available in the current AFM tool shown in Figure 2.7: contact mode and tapping mode.

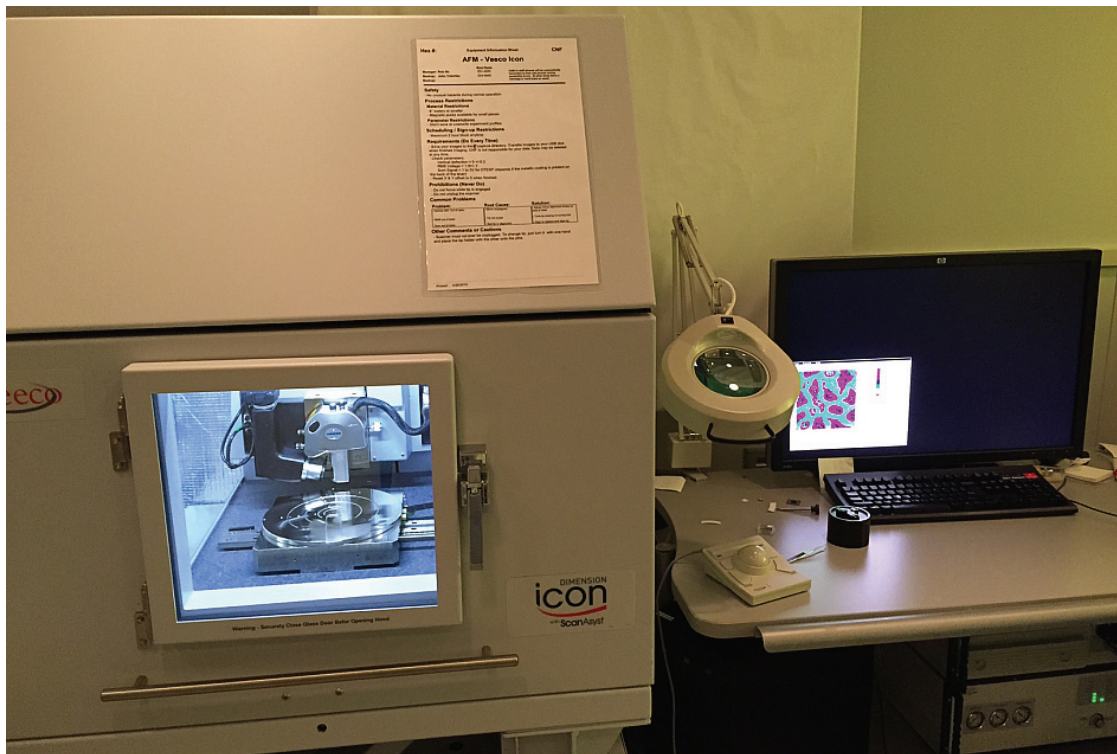


Figure 2.7: Image of an atomic force microscope (AFM) for measuring thickness and surface topography of materials, in the Cornell NanoScale Science & Technology Facility (CNF).

In the contact mode, the sharp AFM cantilever tip is dragged across the surface. A feedback system with a photodiode monitors the beam deflection of the probe tip. A

signal is applied to the scanner to maintain the deflection setpoint. The applied signal is directly proportional to the height of the sample. In the tapping mode, the probe tip scans over the surface at a resonance frequency by contacting the sample surface for a minimal amount of time. Depending on the distance between the probe tip and the sample surface, the amplitude of the tapping motion is changed. A feedback mechanism monitors the changes of the oscillation amplitude and phase, and applies a signal to maintain the amplitude setpoint. The applied signal is directly proportional to the height of the sample. Compared to the contact mode, the intermittent contact reduces damage to the surface in the tapping mode.

2.3.2.2 AFM measurement results on exfoliated MoS₂ flakes

Figure 2.8 shows two AFM measurement results of two different exfoliated thin MoS₂ flakes. The size of the first MoS₂ flake is much bigger than the size of the specified AFM scan window and, therefore, the image only shows a part of the flake. On the other hand, the size of the second MoS₂ flake is smaller than the size of the AFM scan window, and hence, the flake shape can be observed. To measure the thickness of the flake, a height profile is obtained across the flake boundary.

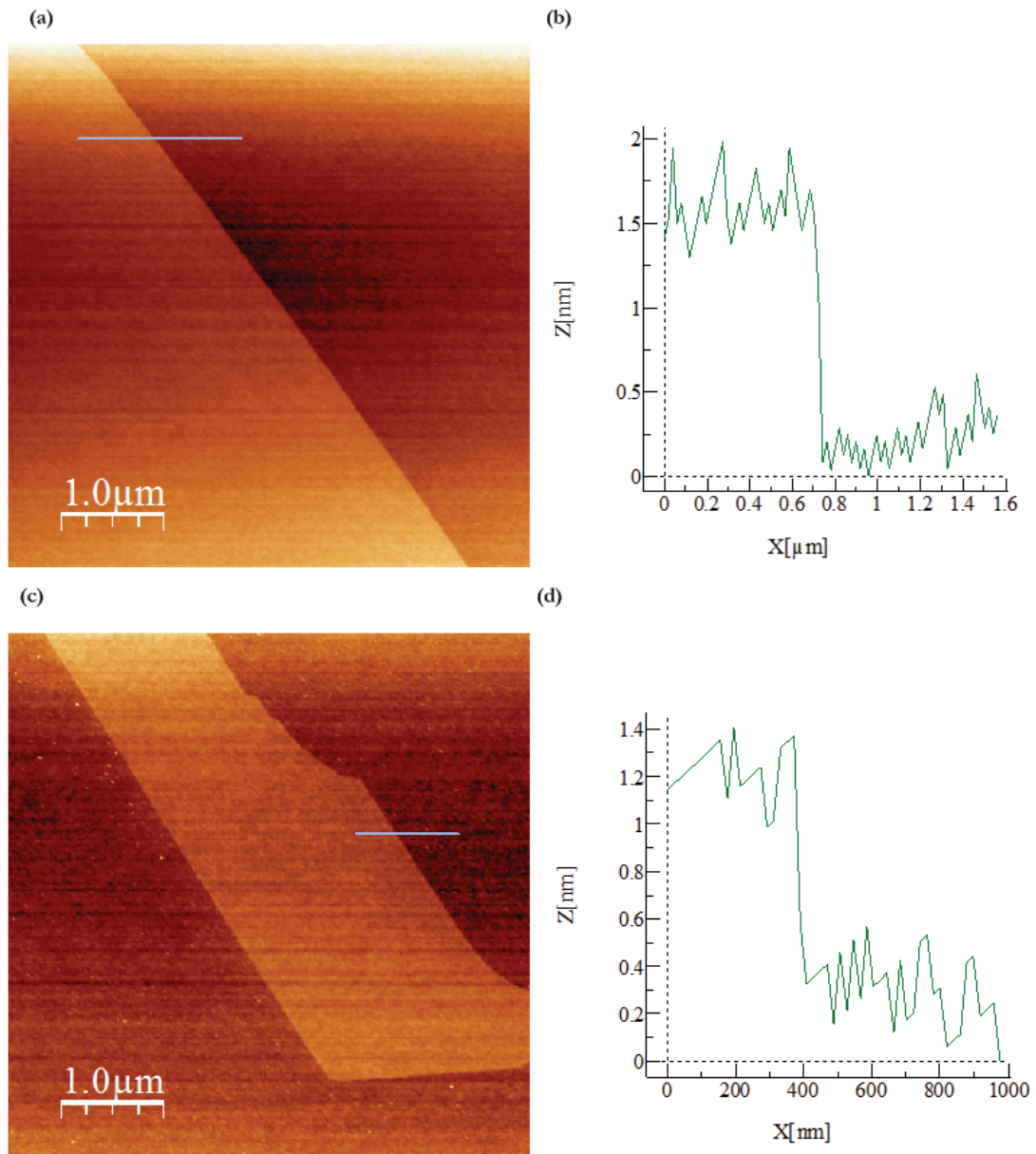


Figure 2.8: AFM images and profiles of exfoliated MoS₂ flakes. (a,b) A bilayer MoS₂ flake (around 1.3 nm thickness) with measured results. (c,d) A monolayer MoS₂ flake (around 0.65 nm thickness) with measured results. The purple bars on the images are the locations where the height profiles are measured.

2.3.2.3 AFM artifacts

Here, one of the most popular artifacts, i.e., a tip artifact, is discussed. It is important to

understand the artifact to correctly analyze the data. Occasionally, AFM image results lead to a false conclusion because of artifacts generated in the images. The sources of artifacts in AFM images include the probe tip, the scanner, vibrations, the feedback system, and the image-processing software [64]. When using an AFM tool at Cornell, in most cases the only thing one needs to worry about is the probe tip. This is because while the other sources like the scanner, vibrations, and the feedback system are not controlled by the user, the user needs to manage the probe tip very carefully. An AFM tip should be much sharper than the sample feature for proper measurements. However, the apex of the AFM tip can be worn out after three to four two-hour-measurements are made. Additionally, a new tip might itself have a defect. Figure 2.9 shows AFM images with and without the tip artifact using the same sample. As one can clearly see, although the measurements are done on the same sample surface, there are lots of triangular shapes in the first image, while there are no triangular shapes observed in the second image. Those triangular shapes are the tip artifacts mainly due to the blunt apex of the tip. When a new sharp tip is used, the actual image is correctly measured as shown in the second image.

In general, many users who have done a large number of AFM measurements are able to determine whether the images obtained contain artifacts or not. If the user has doubts about the tip artifact in the image, three different methods are used to verify it. The first method is to rotate the sample and measure it again to see if the direction of the feature shapes changes or not. The second method is to replace the old AFM tip with a new one and measure the sample again to see if the feature shapes are the same or not. The last method, which is probably the easiest, is to ask

colleagues or the tool staffs who are experts in AFM measurements.

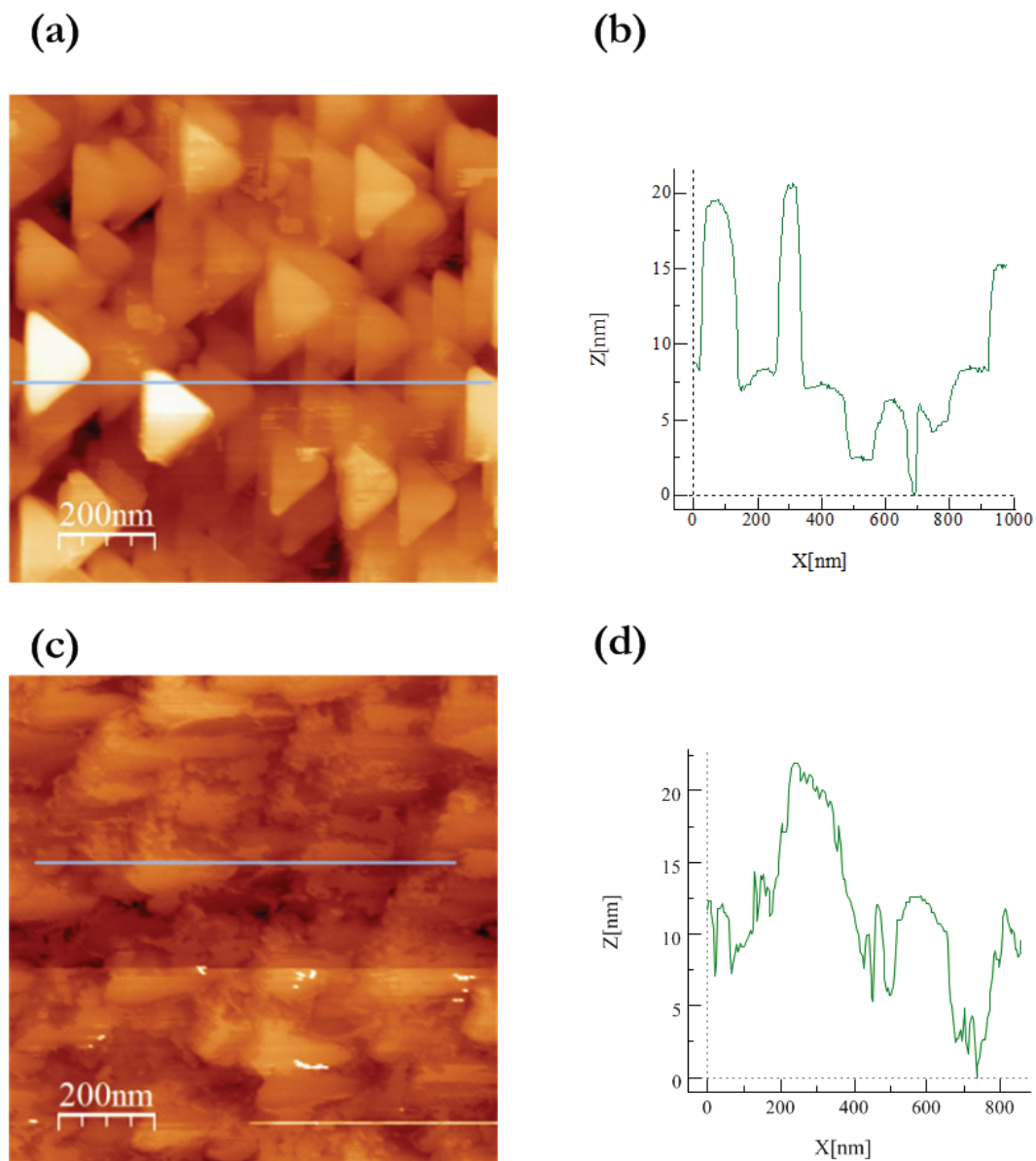


Figure 2.9: AFM images with and without a tip artifact on the same sample. (a,b) Multiple similar sized triangular shapes produced by the tip artifact. (c,d) The actual surface image of the same sample measured in (a) after replacing the old AFM tip with a new tip.

2.3.3 Transmission Electron Microscopy (TEM)

2.3.3.1 Introduction

A transmission electron microscope (TEM) is a very powerful tool for seeing the actual atomic structure of 2D materials [65, 66]. In addition, it enables users to investigate 2D materials in great detail about grain boundaries, defects, and single crystalline area. A TEM hits a sample prepared on a special grid with a beam of electrons. The electrons are then either transmitted through the specimen or scattered (or diffracted) by the specimen. These electrons contribute to various TEM imaging modes. For example, the transmitted (or unscattered) electrons contribute to a bright area of the image and the scattered (or diffracted) electrons contribute to a dark area of the image in a bright field (BF) imaging mode. A dark field (DF) image and an electron diffraction pattern can be obtained using different imaging modes.

2.3.3.2 TEM imaging results on a single layer graphene

Figure 2.10 shows a bright field image of a single layer graphene transferred onto a TEM grid and the electron diffraction pattern of the graphene. The six diffraction spots in the pattern, which are due to the six-fold symmetry of graphene, form a definitive identification of a monolayer graphene [67, 68].

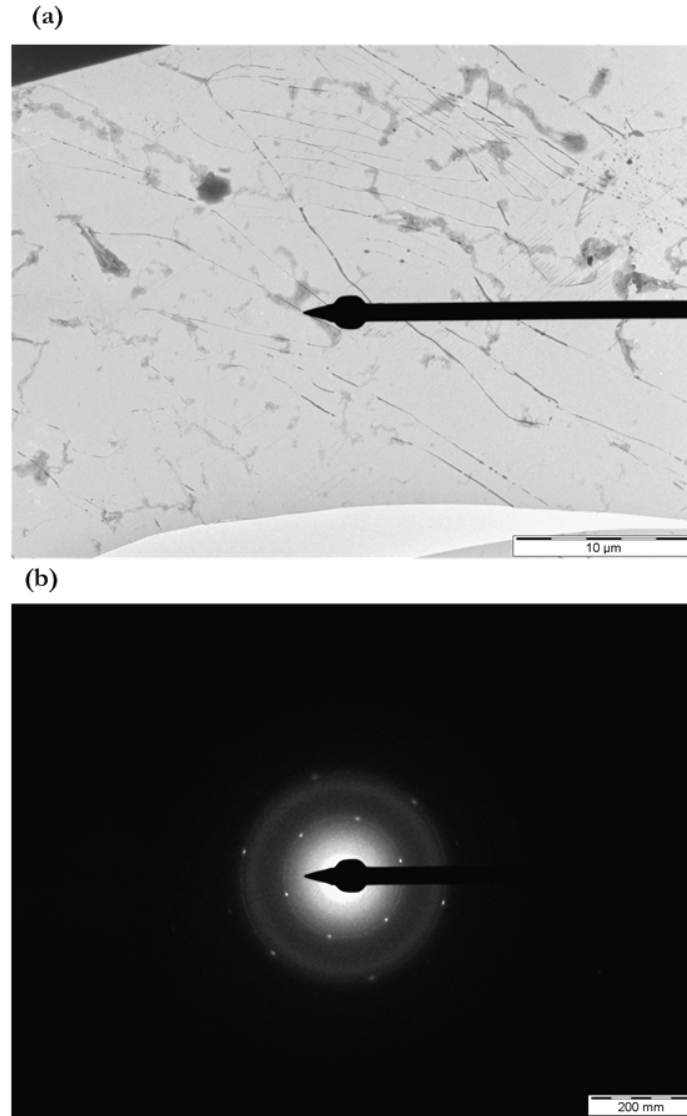


Figure 2.10: TEM images of a monolayer graphene. (a) Bright field image of the graphene transferred on a TEM grid. (b) Electron diffraction pattern of the monolayer graphene, which clearly shows six diffraction spots in the pattern.

2.3.3.3 Graphene sample preparation for TEM

Although TEM is a powerful tool for analyzing 2D materials, there are some issues. One of the issues is a sample preparation for the TEM measurement. The sample preparation procedure for graphene is similar to the wet etching transfer method

described in the previous section except that the target substrate is a TEM grid, which is much harder to transfer graphene onto. A TEM grid is a 3 mm diameter ring (some other shapes are available) and a mesh structure inside the ring as shown in Figure 2.11. An ultrathin supporting film (< 10 nm), e.g., formvar, carbon, or silicon nitride, etc., is needed to hold the graphene.

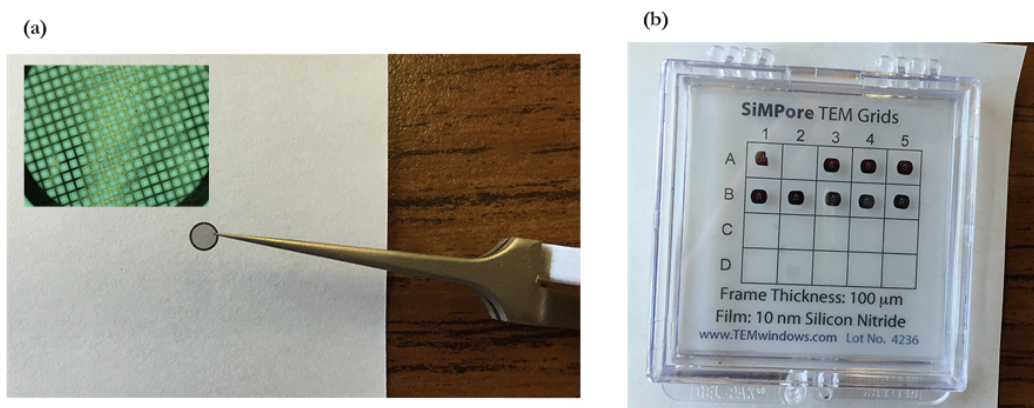


Figure 2.11: Images of TEM grids. (a) Image of a TEM grid with a ring shape. The inset shows a magnified image of the grid with a mesh structure. (b) Picture of other shape of TEM grids.

Since TEM grids are ultrathin and easy to tear apart compared to wafer type substrates, the wet etching transfer process requires a tremendous effort.

2.4 Absorption coefficient of MoS₂

In this section, a MoS₂ absorption coefficient extraction result is discussed. As discussed earlier, AFM measurements provide the actual thickness information for MoS₂ flakes. In addition, Raman spectra of MoS₂ flakes provide the intensity change

information of silicon Raman peaks depending on the different thicknesses of MoS₂ flakes. By the Beer-Lambert law (or light attenuation equation), the absorption coefficient of MoS₂ is estimated with the data obtained from the Raman spectra and the AFM measurements.

2.4.1 Raman spectra of several MoS₂ flakes and their colors

Figure 2.12 shows Raman spectra of several exfoliated MoS₂ flakes on a SiO₂/Si wafer. The first thing to notice in the figure is, the color of the MoS₂ flake depends on its thickness, which is attributed to optical interference and the different reflectivity depending on the flake thicknesses [69-72]. Because the color is distinct by thickness, one can find a thin flake in a much faster way. For instance, if the color is indistinguishable by the naked eye, all the flakes must be measured by AFM to identify a thin flake. This process is very time consuming and expensive. Potentially, it is also possible that the AFM tip could damage the atomic thin flake. On the other hand, if one can just scan over the flakes using an optical microscope and pick a couple of flake candidates by the color differences for AFM measurements, the time for finding a thin flake can be greatly reduced. The color of the flake is generally sensitive to the light source and the substrate. The rule of thumb is, the thinner the flake, the more purple the color when the graphene and MoS₂ are on a 285 nm SiO₂/Si wafer.

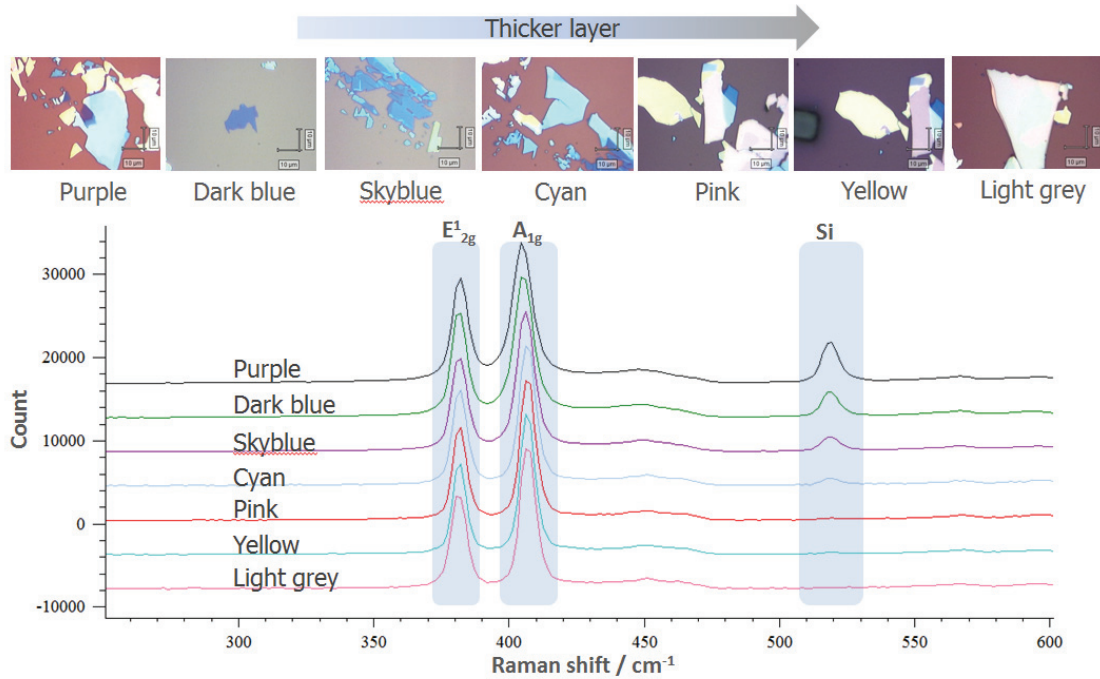


Figure 2.12: Raman spectra of several exfoliated MoS₂ flakes. The thinner the flakes, the more purplish-bluish the flake color. In addition, the intensity of the silicon Raman peak increases as the flake gets thinner.

Another thing to notice from the Raman spectra in the figure is, as the flake gets thinner, the intensity of the silicon Raman peak increases. For a thick MoS₂ flake, the Raman laser interacts (or is scattered) with the flake only; the substrate causes no scattering event. Conversely, if the MoS₂ flake is thin, the Raman laser penetrates the flake and is also scattered by the silicon substrate. The scattering event by the silicon is detected by the Raman system. The intensity changes of silicon peaks in the Raman spectra are important information for determining the MoS₂ absorption coefficient later on.

2.4.2 Distance between the MoS₂ Raman peaks (E_{2g}¹ and A_{1g})

One of the identification methods to determine the thickness of MoS₂ layers is to see the Raman shift in the distance between the two major peaks, E_{2g}¹ and A_{1g}. Figure 2.13 shows a plot of peak distance versus number of layers from another experimental set of MoS₂ flakes.

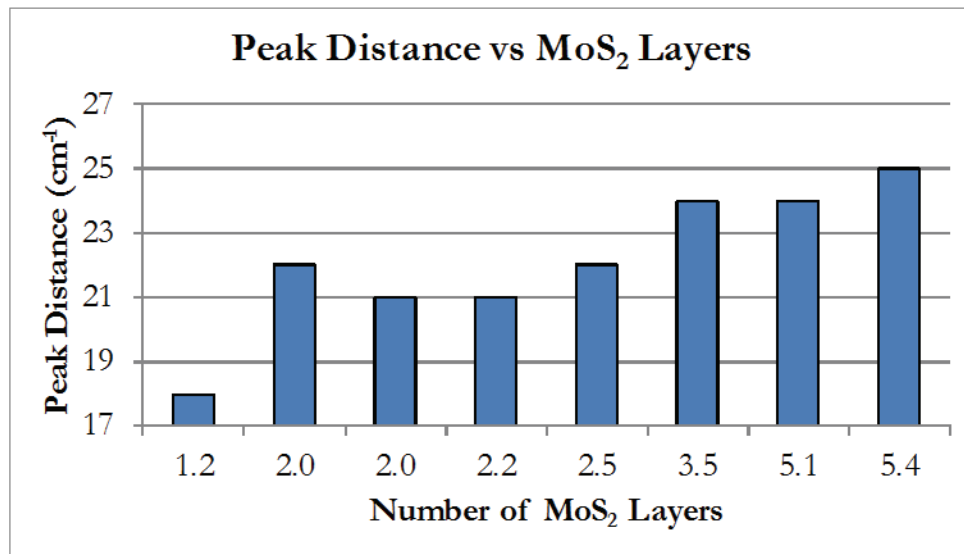


Figure 2.13: Plot of peak distance of two MoS₂ Raman peaks, E_{2g}¹ and A_{1g} versus number of MoS₂ layers. The Raman peak distance increases as the number of layers increase.

The trend shows that as the number of MoS₂ layers increases, the distance between E_{2g}¹ and A_{1g} also increases. Since the peak distance is saturated for thick MoS₂ layers [62], this method is good for identifying thin layers of MoS₂. The reason for the increment of peak distance is that the out-of-plane (A_{1g}) mode is stiffened by interlayer van der Waals interaction with increasing number of layers, which

suppresses atom vibration.

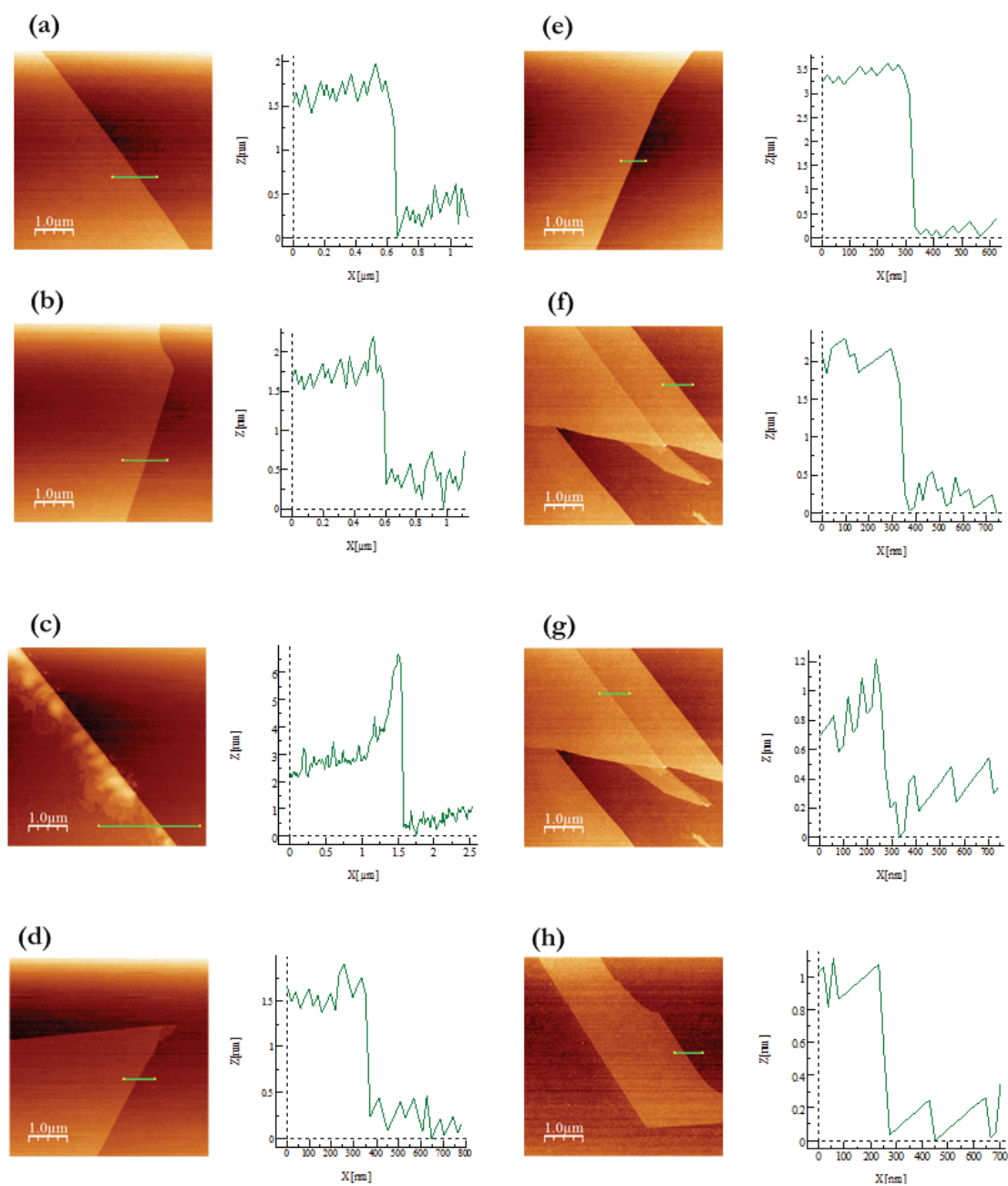


Figure 2.14: AFM measurement results of another set of MoS₂ flakes. (a-h) AFM images are shown on the left and the corresponding height profiles are shown on the right.

The suppression of atom vibration results in a higher spring constant, and thus, it effectively increases the restoring force on the atoms [62, 73]. In consequence, the A_{1g} peak is shifted to a higher frequency, i.e., it gains a higher energy. For thick multilayers of MoS_2 , bulk effects like Coulombic interlayer interactions dominate and the peak distance is saturated [73].

One side note about the plot is that even though the number of MoS_2 layer is determined by AFM measurements, the x-axis thickness numbers are not integers because AFM profiles contain some noisy signals as shown in Figure 2.14. The numbers of MoS_2 layers are calculated based on the thicknesses, which are then divided by the monolayer thickness of MoS_2 or 0.65 nm.

2.4.3 Estimation of MoS_2 absorption coefficient

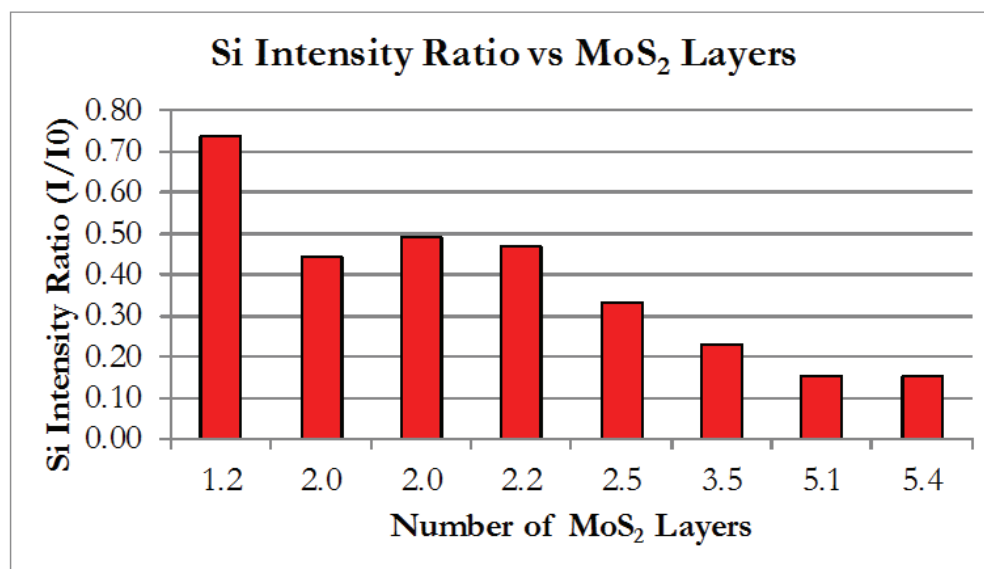


Figure 2.15: Plot of the change of the silicon Raman peak intensity ratio versus number of MoS_2 layers. The trend shows that the thinner MoS_2 , the higher silicon Raman intensity.

Figure 2.15 shows the ratio of an intensity of silicon Raman peak of each characterized MoS₂ flake to the reference silicon Raman peak. As previously mentioned, it shows that as the number of MoS₂ layers decreases the intensity of the silicon Raman peak increases. The MoS₂ absorption coefficient is determined using the following light attenuation equation from Raman measurement [74];

$$I = I_0 e^{-2\alpha t} \rightarrow \alpha = \frac{\ln \frac{I}{I_0}}{-2t}$$

where I is the silicon Raman peak intensity from the flake, I₀ is the reference silicon Raman peak intensity on wafer, t is the thickness of the MoS₂ flake, and α is the MoS₂ absorption coefficient [cm⁻¹]. From the MoS₂ flake thickness data (t) from the AFM measurements and the silicon peak intensity data (I/I₀) from the Raman spectra, the average absorption coefficient of the thin layer MoS₂ flakes is estimated to be 2.8×10⁶ cm⁻¹. This value is somewhat close to a theoretical calculation value, 1.5×10⁶ cm⁻¹ for a monolayer MoS₂ absorption coefficient [75]. In summary, the characterization results from both AFM and Raman measurements of each MoS₂ flake are shown in Table 2.1 and the calculations for the absorption coefficient are shown in Table 2.2.

Table 2.1: Characterization results of each MoS₂ flakes from AFM and Raman spectroscopy.

Sample	Flake thickness (nm)	Flake layer (L)	Raman shift (cm-1)				Intensity	Ratio
			E12g	A1g	Si	Peak distance	Si	I/I0
1 (50x)	1.3	2.0	384	406	520	22	26300	0.44
2 (100x)	1.4	2.2	384	405	520	21	24930	0.47
3 (50x)	3.5	5.4	383	408	520	25	9100	0.15
4 (100x)	1.3	2.0	384	405	520	21	25970	0.49
5 (50x)	3.3	5.1	383	407	520	24	9100	0.15
6 (100x)	1.6	2.5	384	406	520	22	17700	0.33
6_1 (100x)	0.7 + 1.6	3.5	383	407	520	24	12200	0.23
7 (100x)	0.8	1.2	385	403	520	18	39030	0.74
Si (50x)	520	.	59300	.
Si (100x)	520	.	52980	.

Table 2.2: Calculations of MoS₂ absorption coefficient for each flake.

Sample	Calculation			Absorption Coeff
	Ln (I/I ₀)	thickness (cm)	-2*thickness	
1 (50x)	-0.813	1.30E-07	-2.60E-07	3.13E+06
2 (100x)	-0.754	1.40E-07	-2.80E-07	2.69E+06
3 (50x)	-1.874	3.50E-07	-7.00E-07	2.68E+06
4 (100x)	-0.713	1.30E-07	-2.60E-07	2.74E+06
5 (50x)	-1.874	3.30E-07	-6.60E-07	2.84E+06
6 (100x)	-1.096	1.60E-07	-3.20E-07	3.43E+06
6_1 (100x)	-1.468	2.30E-07	-4.60E-07	3.19E+06
7 (100x)	-0.306	8.00E-08	-1.60E-07	1.91E+06
Si (50x)				
Si (100x)				

2.5 Summary

In this chapter, the necessary procedures for sample preparation were introduced and discussed for actual 2D materials device researches. A physical property of MoS₂, for example the absorption coefficient, is calculated by the procedures. The first part of the chapter discussed three popular transfer methods for 2D materials: the exfoliation, thermal release tape, and wet etching methods. For a large area transfer of a 2D material grown on a metal foil, the wet etching method is the one generally used. The second part of the chapter discussed various characterization tools for 2D materials. The two essential tools for 2D characterization, Raman spectroscopy and AFM, were discussed first and then followed by a brief discussion about TEM. The distinct Raman peaks of graphene and MoS₂ as well as the AFM results were discussed. The last part of the chapter discussed the absorption coefficient of MoS₂. That value is estimated to be approximately $2.8 \times 10^6 \text{ cm}^{-1}$, based on the characterization results from the Raman spectra and the AFM measurements for several MoS₂ flakes.

CHAPTER 3

DEVICE FABRICATION USING TWO-DIMENSIONAL MATERIALS

3.1 Introduction

Two-dimensional (2D) materials have many advantages, e.g., graphene's superior mobility, atomically thin flexible layer, and high transparency, for various device applications [76]. Specifically, several of the 2D materials are strong candidates for a breakthrough in the traditional silicon industry to overcome the physical limitations of silicon-based devices as transistor sizes scale down. For instance, when a 2D material is used as a current channel of a transistor, the device structure is similar to a Silicon-on-Insulator (SOI) transistor with a thin body. Since the 2D material forms an ultrathin body of the transistor, the body leakage current of the transistor is greatly reduced. As a result, the transistor with 2D material will have better performance with reduced power consumption.

In this chapter, a device fabrication process using graphene and MoS₂, and the measurement results of the transistors, are discussed. This chapter begins with a top- and back-gated transistor fabrication process, from a mask design step to a finish-up step. An issue about dielectric deposition on the 2D materials is explored. Finally, the results of electrical characterization of the fabricated transistors are discussed.

3.2 Device fabrication process

A brief overview of the fabrication processes for graphene and MoS₂ transistors may be summarized as follows:

1. Sample preparation.
2. Mask design and fabrication.
3. Drain and source metal contacts formation.
4. Transistor channel formation.
5. Global back gate metal contact formation.
6. Gate dielectric deposition.
7. Top gate metal contact formation.
8. Device annealing.

The device fabrication processes are all performed in a cleanroom. Each process step is discussed in more detail in the following sections.

3.2.1 Sample preparation

Two steps are needed in the sample preparation for a transistor fabrication. The first step is a dielectric deposition on a bare silicon wafer unless the dielectric is already on the wafer. Before the dielectric is deposited on a new silicon wafer, the native silicon dioxide (SiO₂) needs to be removed using buffered oxide etch (BOE) or hydrofluoric acid (HF) for an accurate physical property control of the dielectric material deposited. For instance, if a high-k dielectric is deposited with 30 nm thickness on the native SiO₂ oxide (usually 2-3 nm thickness [77]), the thickness error between the actual

deposited thickness and the total thickness can be 10%. In addition, an estimation of the actual dielectric constant is complicated because the native SiO₂ and the high-k dielectric constants are different. In general, wet oxidation furnace processing (at around 1000 °C) is performed for a high quality SiO₂ deposition. For a high-k dielectric deposition like hafnium oxide (HfO₂) and aluminum oxide (Al₂O₃), an atomic layer deposition (ALD) tool is used.

The second step is 2D materials preparation on the substrate. MoS₂ flakes are exfoliated from a natural chunk of MoS₂ crystal onto the substrate prepared in the first step for MoS₂ transistors. Graphene grown on copper foil is transferred onto the substrate by the wet etching transfer method for graphene transistors. In this case, when graphene is directly grown on an insulator like a sapphire wafer, the transfer process is not needed. Once the transfer process is finished, the characterization process is followed to confirm the presence and the quality of the transferred material. More details regarding 2D materials transferring and characterization are discussed in Chapter 2.

3.2.2 Mask design and fabrication

A transistor layout design is performed with a computer aided design (CAD) tool, e.g., L-edit at the Cornell CNF. Figure 3.1 shows a mask design for graphene transistors. The actual area of the mask design is 1 cm by 1 cm. Typically, additional test structures, such as transmission line method (TLM) structure, van der Pauw structure, hall bar, and so on, are contained in a mask design for various experiments, which are not included in this particular mask design.

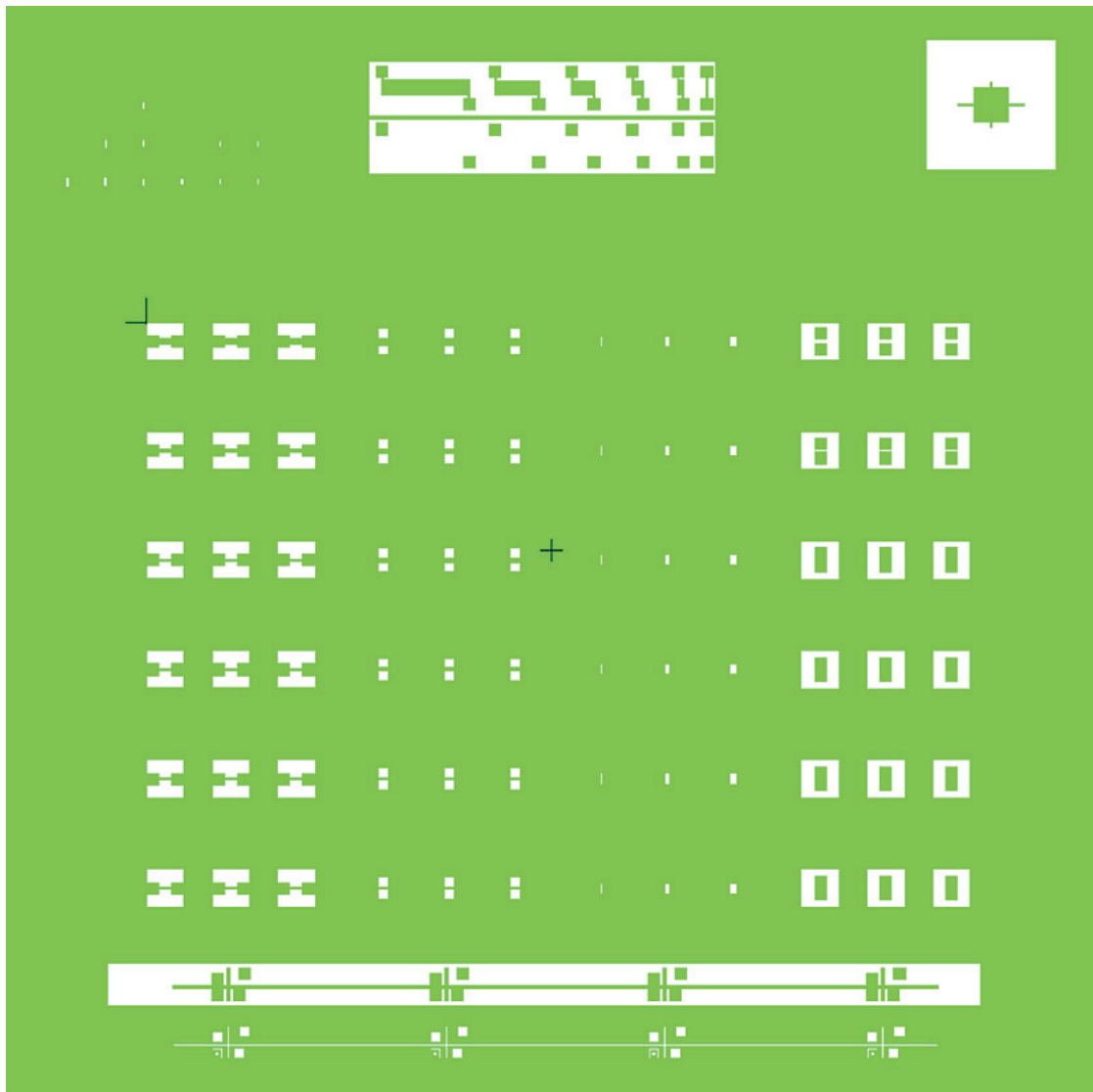


Figure 3.1: Image of one of the mask designs for 2D device fabrications.

Once the mask design is finished and converted into a graphic database system (GDSII) file, a pattern generator tool prints the design on a hard chrome/quartz photomask. The exposed mask then goes through chemical processes like developing, etching, and cleaning.

3.2.3 Drain and source metal contacts formation

Drain and source metal pads are needed for direct wafer probing for electrical characterizations of the devices. The first step is a photolithography process using the mask. For a metal deposition, either of two methods is used. One method is a bilayer lift-off process (using LOR photoresist) and the other method is a standard one layer photoresist process (using SPR220 photoresist) as shown in Figure 3.2. If the feature size is small, the lift-off process is recommended to prevent the metal deposition on the sidewall of the photoresist. The photolithography process for the metal deposition is described in the following:

1. Preparatory steps for the lift-off process:
 - a. Prebake the sample for 1 minute at 180 °C on a hot plate.
 - b. Spin coat LOR 10A photoresist at 3000 rpm for 45 seconds.
 - c. Bake the sample at 180 °C for 5 minutes on the hot plate.
2. Preparatory steps for the standard photolithography process:
 - a. Spin adhesion promoter (P20) at 3000 rpm for 60 seconds.
3. Spin SPR220-3 μ m at 3000 rpm for 60 seconds.
4. Prebake the sample at 115 °C for 90 seconds.
5. Expose the sample with ABM contact aligner for 10 seconds.
6. Post-exposure bake the sample at 115 °C for 1 minute.
7. Develop the sample with 726 MIF developer for 1 minute and rinse with DI water.
8. Check the sample with an optical microscope.

9. Deposit 10 nm of titanium as an adhesion layer, followed by 150 nm of gold using an e-beam evaporator (or a sputter).
10. Immerse the sample into 1165 resist stripper for 10 hours and rinse it with DI water.
11. Check the finished sample with the optical microscope.

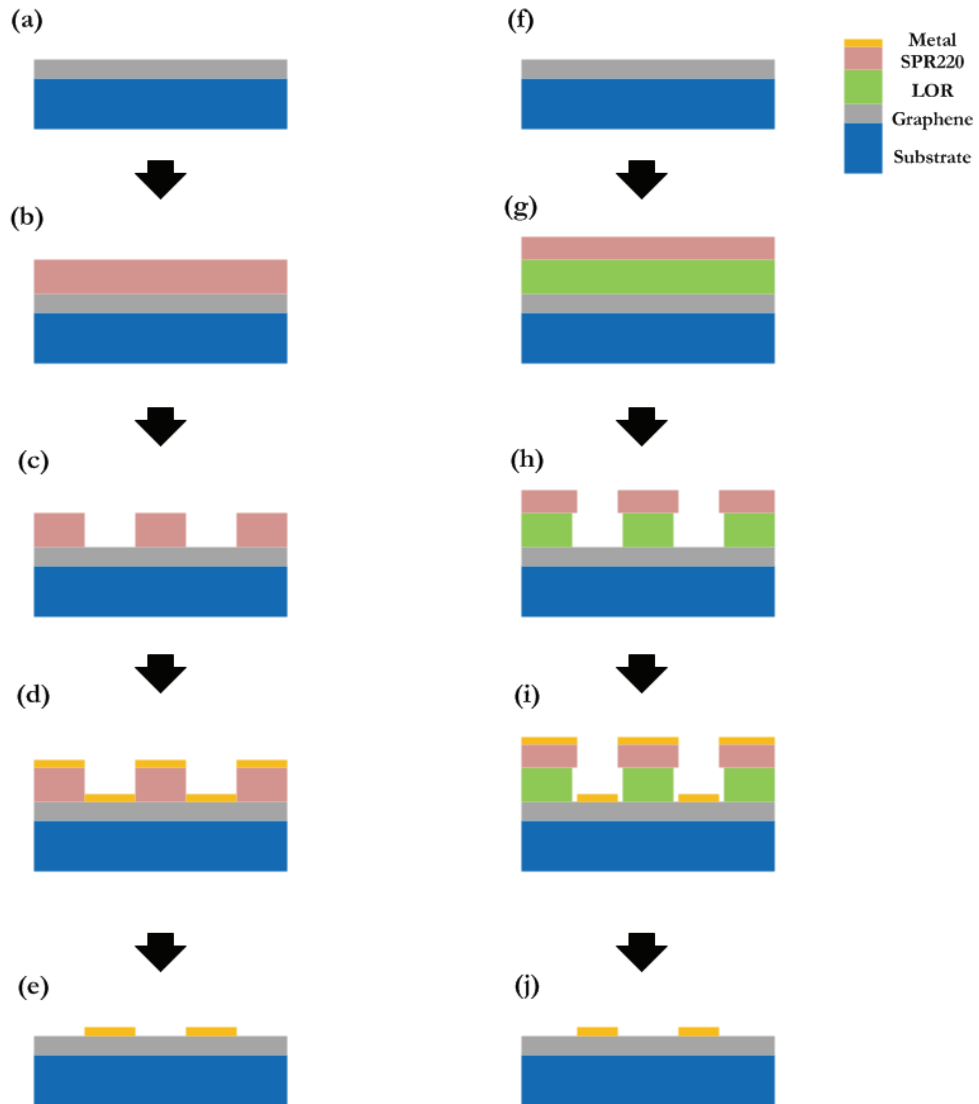


Figure 3.2: Comparison of the two photolithography processes for metal deposition: (a-e) standard one layer photoresist process and (f-j) bilayer lift-off process. (a,e) Graphene on a substrate. (b,g) Photoresist coating. (c,h) Exposure and development. (d,i) Metal deposition. (e,j) Photoresist removal.

After the drain and source metal contacts are formed, a quick current-voltage (IV) measurement is usually performed using a probe station to verify a current flow between the contacts.

3.2.4 Transistor channel formation

The transistor channel for a current flow is formed by a plasma etching process. A graphene channel can be formed by an oxygen plasma etching process. An MoS₂ channel can be formed either by the oxygen plasma for thin flakes or a CF₄ (fluorine) plasma etching process for thick flakes. The first step is the photolithography process with the mask. For the etching process, the standard one layer photoresist process is used. Following the photolithography steps described in the previous section up to step 8, the rest of the etching process is described in the following:

1. Use either an Oxford plasma etching tool or a YES Asher to etch the sample with a proper recipe.
 - a. Oxford 81 recipe: oxygen plasma for less than 10 minutes with O₂ gas flow with 50 sccm.
 - b. YES Asher recipe: O₂ gas flow with 100 sccm, 1000 watts, for 180 seconds at 150 °C.
 - c. Oxford 81 standard CF₄ etching recipe for 30 seconds.
2. Immerse the sample into acetone/IPA for the photoresist strip for 10 hours and rinse it with DI water.
3. Check the finished sample with the optical microscope.

After the etching process is performed, a quick Raman measurement is needed to check whether the graphene channel is intact or not since the graphene is not easily detectable by the optical microscope.

3.2.5 Global back gate metal contact formation

This step is needed when the backside of the SiO₂/Si wafer is not polished, i.e., SiO₂ is present. In this case, CHF₃/CF₄/Ar plasma etching (Oxford tool) is performed for 5 minutes and 30 seconds to etch 280 nm thickness of SiO₂ on the backside. The etching time setting depends on the thickness of the SiO₂. Although highly doped silicon itself is a good global back gate pad, a metal deposition using the e-beam evaporator or the sputter is suggested. To deposit the metal on the backside of the wafer, the front side of the wafer first needs to be coated with a photoresist to protect the surface from possible contamination, followed by the metal deposition.

3.2.6 Gate dielectric deposition

A gate dielectric is an important component to make a three terminal transistor. For a silicon-based transistor, the gate dielectric deposition is not a problem. However, the dielectric deposition on a 2D layered material like graphene and MoS₂ is quite challenging due to the pristine surface having no dangling bonds [78-80]. Therefore, it is worth mentioning some challenges for the dielectric deposition methods in this section.

3.2.6.1 Challenges for top gate dielectric deposition

There are several methods for depositing the gate dielectrics. The first is a physical vapor deposition (PVD) dielectric deposition method such as pulsed laser deposition (PLD), radio frequency (RF) sputter, or e-beam evaporator. The PVD methods can introduce some defects on the graphene lattice, which greatly degrade the mobility of the device. Figure 3.3 shows the introduction of a D peak in Raman spectra of graphene after SiO₂ deposition by PVD methods [81].

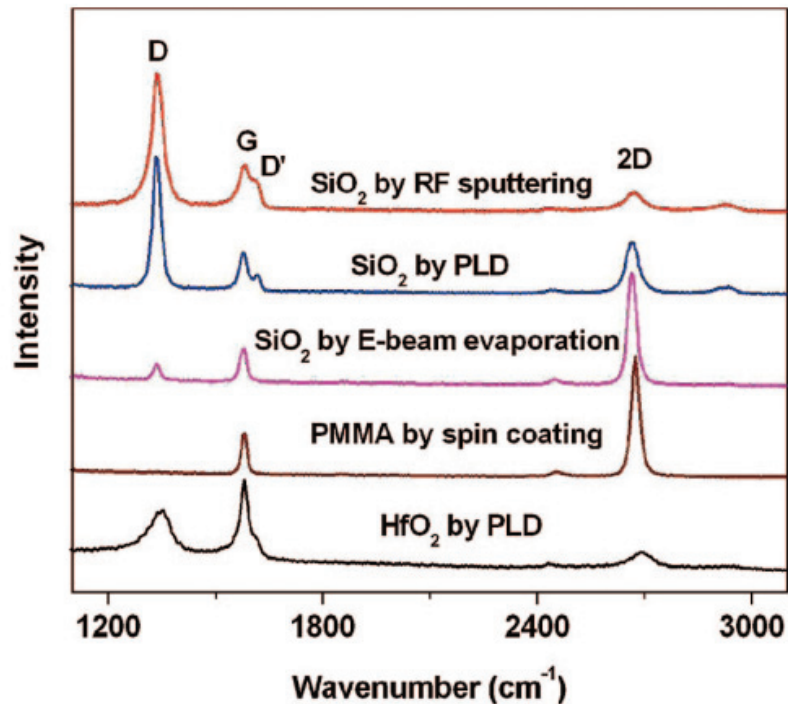


Figure 3.3: Raman spectra of graphene after SiO₂ deposition using PVD methods. The increasing D peak in the Raman spectra means defects are introduced on the graphene. Adapted from [81].

Second is the atomic layer deposition (ALD) dielectric deposition method. In fact,

ALD is the most popular tool to deposit high-k dielectrics for a silicon based device. The method requires chemical functional groups on the surface that react with the ALD precursor molecules [82]. The ALD method includes either H₂O for a thermal ALD process or O₂ for a plasma ALD process. Due to the hydrophobic nature of graphene, the thermal ALD process is not a good way to deposit the dielectric [83]. The other option, the plasma ALD process, is not suitable either because O₂ etches (or damages) the graphene. As a result, to enable the reaction with the ALD precursors, the graphene needs intentional nucleation sites by surface functionalization [83, 84] or nucleation layers by depositing a thin aluminum layer to form aluminum oxide in air [85]. The ALD method using functionalization still introduces undesired impurities by breaking the chemical bonds of graphene, which degrades the mobility of the device [86]. Other methods have been introduced. One promising method uses other 2D dielectric materials such as hexagonal boron nitride (hBN) for transfer of the CVD grown hBN on graphene or direct growth of the hBN on top of graphene [87-89].

3.2.6.2 High-k dielectric deposition

To deposit a top gate high-k dielectric, the ALD method with a formation of nucleation layers is used. Specifically, 1-2 nm thickness of e-beam evaporated SiO₂ is deposited on the graphene surface as seed layers, i.e., rough nucleation layers on the graphene, prior to the ALD high-k dielectric deposition. The first step is the photolithography process with the mask as usual. For the dielectric deposition process, the standard one layer photoresist process is used by following the photolithography steps described in the previous section up to step 8. The rest of the

high-k dielectric process is described in the following:

1. 1-2 nm thickness of SiO₂ is deposited by the e-beam evaporator.
2. 30 nm thickness of high-k dielectric, either Al₂O₃ or HfO₂, is deposited by the thermal ALD process.
 - a. Oxygen plasma cleaning of the chamber without the sample present.
 - b. Seasoning the chamber for the target high-k process for 20 cycles of the precursor pulse at 200 °C without the sample.
 - c. Put the sample in the chamber.
 - d. Oxford ALD FlexAL recipe for the thermal Al₂O₃ deposition: 220 cycles of the precursor pulse-and-purge at 200 °C.
 - e. Oxford ALD FlexAL recipe for the thermal HfO₂ deposition: 250 cycles of the precursor pulse-and-purge at 200 °C.
3. Immerse the sample into acetone/IPA for the photoresist strip for 10 hours and rinse it with DI water.
4. Check the finished sample with the optical microscope and/or the AFM if needed.

3.2.7 Top gate metal contact formation

A top gate metal deposition process is the same as the drain and source metal contacts deposition process with the photolithography steps as described in the section for the drain and source metal contacts formation.

3.2.8 Device annealing

The final step of the 2D transistor fabrication process is a device annealing process that removes the photoresist residue. For the device annealing process, the carbon nanotube/graphene furnace in CNF is used. The sample is annealed with a gas mixture of Ar/H₂ 10% (i.e., 1000sccm/100sccm) at atmospheric pressure (atm) for 2 hours at 200 °C or 300 °C. Figure 3.4 shows a schematic cross section of the fabricated graphene and MoS₂ transistors.

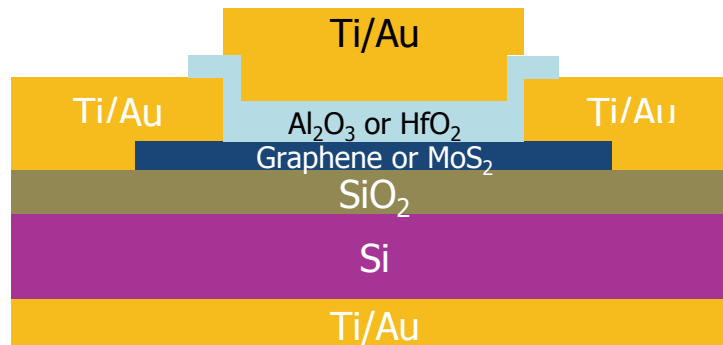


Figure 3.4: Schematic cross section of the fabricated 2D transistor.

3.2.9 List of CNF tools used for the device fabrication

Table 3.1 shows the list of the device fabrication process tools used in the Cornell CNF clean room. A full list of CNF tools can be found in the following link:

<http://www.cnf.cornell.edu/>.

Table 3.1: List of CNF tools used for the device fabrication.

Process Category	Tool name	Description
PHOTOLITHOGRAPHY	ABM Contact Aligner	Flexible 200mm Mask Aligner with DUV light source
	Autostep i-line Stepper	GCA Autostep 200 DSW i-line Wafer Stepper
	Heidelberg Mask Writer DWL2000	DWL2000 Laser Pattern Generator and Direct Writer
	GCA PG 3600 Pattern Generator	Mask pattern generator
FURNACE PROCESSING	Wet/Dry Oxide - B2	MRL Industries Furnace for oxidation of silicon substrates
	Carbon Nanotube/Graphene Furnace	First Nano Carbon Nanotube and Graphene Furnace
COMPUTING	L-Edit CAD Software	L-Edit Layout Editor software by Tanner EDA
ELECTRICAL TESTING	IV Probe Station	I-V Measurement Systems
METROLOGY	FilMetrics Film Measurement Systems	F40 / F50-EXR Optical Measurement Systems for transparent thin film measurement
	P10 Profilometer	Equipment for measuring surface topology in the micron or finer scales.
	Woollam Spectroscopic Ellipsometer	Variable Angle Ellipsometer for full optical characterization of thin films
SEMS / MICROSCOPES	AFM - Veeco Icon	Veeco Icon Atomic Force Microscope for high resolution profilometry
	Nikon Eclipse L200N	Microscopes for inspection of devices
	Olympus Confocal Microscope	Olympus BX60/U-CFU Real Time Confocal Microscope
	Zeiss Ultra SEM	Ultra High Resolution Field Emission SEM
ETCHING	Branson Resist Strip	Oxygen plasma barrel asher for Photoresist/organic removal
	Glen 1000 Resist Strip	Oxygen Plasma tool for removal of organics
	Hamatech Hot Piranha	Automatic Wafer Processor for SC-1 & Piranha cleans
	Oxford 81 Etcher	Oxford PlasmaLab 80+ RIE System for fluorine based etching of oxide, nitride, & silicon
	PT720-740 Etcher	PlasmaTherm720/740 Chlorine-based RIE system for Silicon & Aluminum etching
	YES Asher	YES CV200RFS Oxygen Plasma Asher
	YES Asher	YES CV200RFS Oxygen Plasma Asher
THIN FILM DEPOSITION	AJA Sputter Deposition	Load-lock single wafer, AJA sputter tool for deposition of thin metallic and dielectric films
	CVC Sputter Deposition	Magnetron Sputter system for depositing thin metal & dielectric films
	GSI PECVD	GSI Plasma Enhanced Chemical Vapor Deposition System
	Oxford ALD FlexAL	Atomic Layer Deposition
	SC4500 Odd-Hour Evaporator	CVC SC4500 Combination Thermal/ E-gun Evaporation System for deposition of thin films
	SC4500 Even-Hour Evaporator	CVC SC4500 E-gun Evaporation System for deposition of thin films
PACKAGING & MISC PROCESSING	Dicing Saw - KS 7100	K&S 7100 Dicing Saw
	RTA - AG610	Rapid Thermal Anneal - AG Associates Model 610
	Westbond 7400A Ultrasonic Wire Bonder	Wire bonder

3.3 Two-dimensional material based transistors

In this section, the results of current-voltage measurement of the fabricated graphene transistors and MoS₂ transistors are presented and discussed.

3.3.1 Graphene transistor

To measure electrical characteristics of top-gated graphene transistors, first two sets of graphene transistors are fabricated. The first set uses a CVD grown graphene on a sapphire wafer with the as-received sample Hall mobility less than 200 cm²/Vs. The top gate dielectric is deposited with the ALD processed Al₂O₃ high-k material (relative permittivity: 9.3). The second set uses another CVD grown graphene on a sapphire wafer with the as-received sample Hall mobility around 1000 cm²/Vs. The top gate dielectric is deposited with the ALD processed HfO₂ high-k material (relative permittivity: 25). The method described in the high-k dielectric deposition section is performed. In brief, a very thin e-beam evaporated SiO₂ seed layer is deposited first to create nucleation sites followed by the actual ALD deposition. Since both graphene samples are directly grown on the insulator, no transfer processes are needed. The channel lengths of the devices can be any of 5, 10, 15, 20, 30, or 50 μm, and the channel widths can be any of 25, 50, or 75 μm; each channel can be of a different width and length combination. Figure 3.5 shows an optical microscope image of one of the fabricated top-gated graphene transistors.

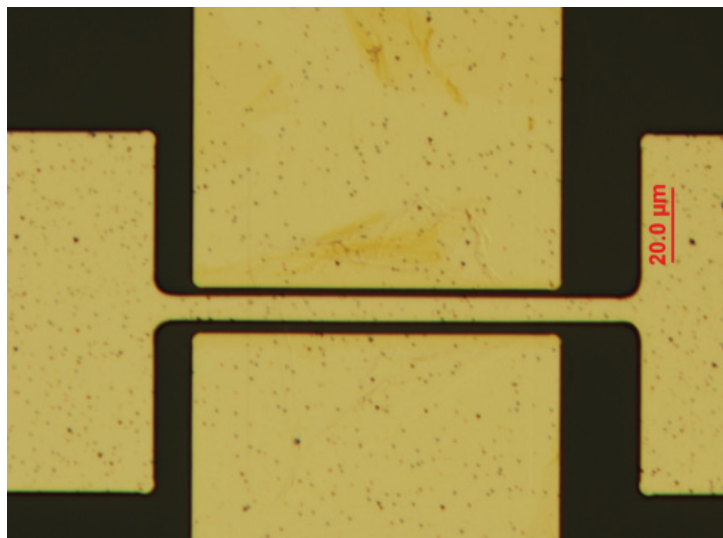


Figure 3.5: Optical microscope image of a fabricated top-gated graphene transistor. The transparent graphene channel formed between the top and bottom contacts is hardly detectable from the image.

Figures 3.6 and 3.7 show the current-voltage measurement results of one of the graphene transistors with Al_2O_3 and one of the graphene transistors with HfO_2 , respectively. The measurements are done with three terminals: a variable drain bias (V_D), a variable top gate bias (V_G), and a grounded source (V_S). Each figure contains three graphs: transfer characteristic curves ($I_{DS}-V_{GS}$) with large V_{DS} biases, transfer characteristic curves ($I_{DS}-V_{GS}$) with small V_{DS} biases, and output characteristic curves ($I_{DS}-V_{DS}$) in a small bias region. The transfer characteristic curves show the ambipolar transport characteristics of graphene FETs. The field effect mobility values of $25.7 \text{ cm}^2/\text{Vs}$ and $13.4 \text{ cm}^2/\text{Vs}$ are calculated for the transistors shown on Figures 3.6 and 3.7, one with Al_2O_3 and the other with HfO_2 , respectively. Those low mobility values are possibly attributed to the charged impurity scattering with the rough SiO_2 seed layer and defects and contaminations from the fabrication process.

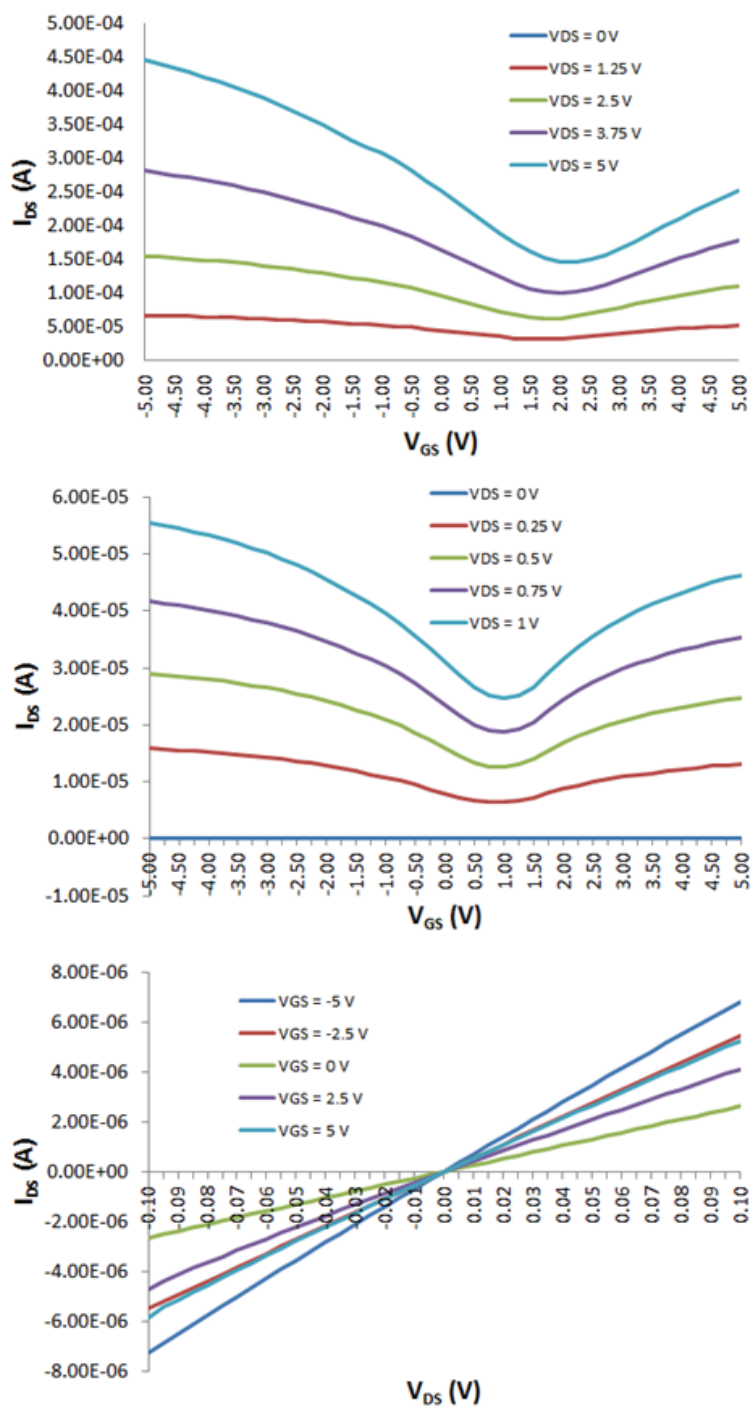


Figure 3.6: Current-voltage curves of a top-gated graphene transistor with Al_2O_3 . From top to bottom: transfer characteristic curves (I_{DS} - V_{GS}) with large V_{DS} biases, transfer characteristic curves (I_{DS} - V_{GS}) with small V_{DS} biases, and output characteristic curves (I_{DS} - V_{DS}) in a small bias region.

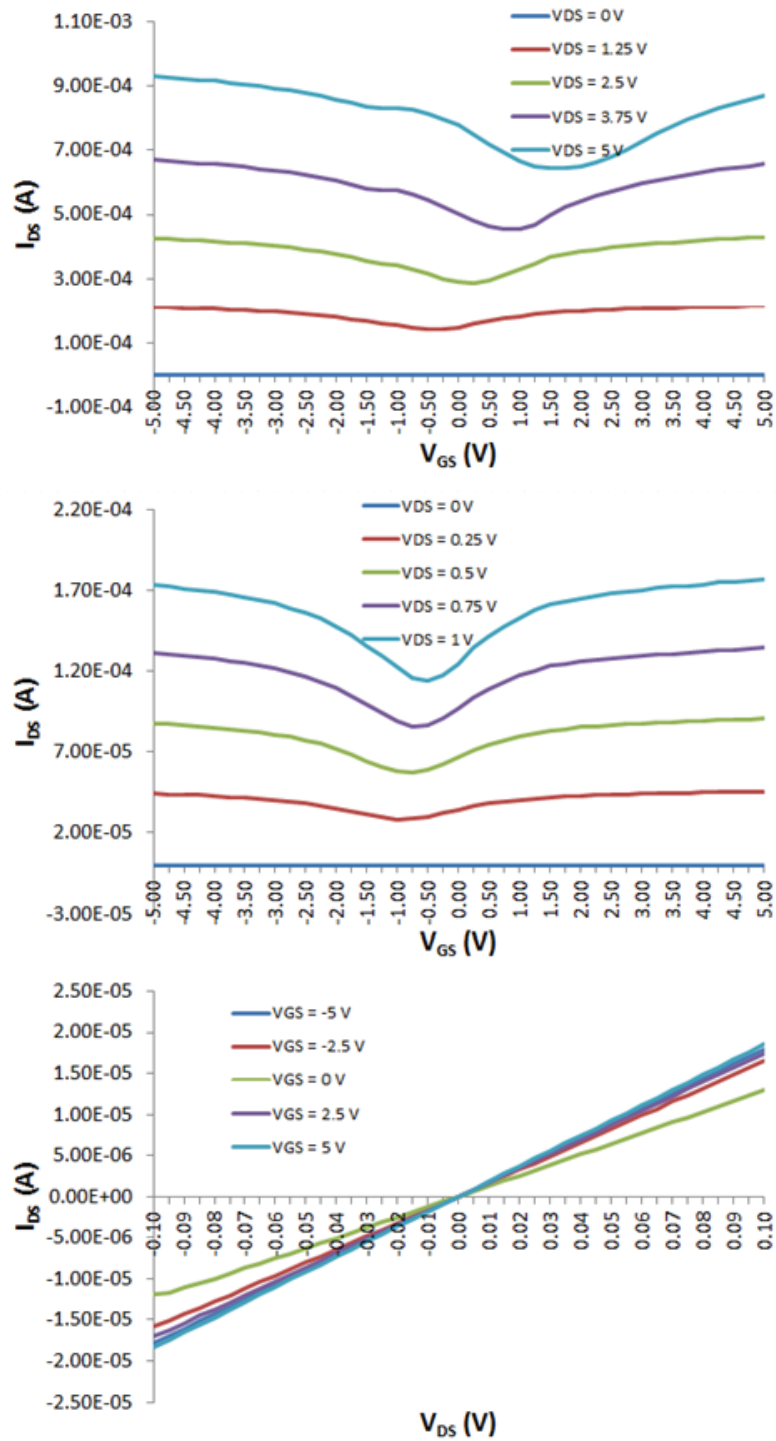


Figure 3.7: Current-voltage curves of a top-gated graphene transistor with HfO₂. From top to bottom: transfer characteristic curves (I_{DS} - V_{GS}) with large V_{DS} biases, transfer characteristic curves (I_{DS} - V_{GS}) with small V_{DS} biases, and output characteristic curves (I_{DS} - V_{DS}) in a small bias region.

The I_{DS} - V_{GS} curves with large V_{DS} biases show the Dirac point shifts with different V_{DS} values. As the drain voltage increases, the Dirac point shifts to the right. The minimum current flows at the Dirac point when the carrier injection from the drain is equal to the opposite carrier injection from the source in an ambipolar device [90, 91]. Since the higher drain voltage injects more holes in the channel (i.e., collects more electrons in the drain terminal), the higher gate voltage, which induces more electrons in the channel, is needed to make the channel charge neutral. By the linear energy dispersion relationship of graphene, the charge carrier density at the Dirac point is supposed to be zero, i.e., no current at the point. However, there is a minimum conductivity at the Dirac point in the I_{DS} - V_{GS} curves of graphene as shown in the figures. The presence of disorders, e.g., defects in graphene and charged impurities in the substrate, induces a spatially inhomogeneous potential distribution that creates local potential fluctuation. This effect is significant near the Dirac point because the screening of the local potential fluctuation is weak due to the low carrier density. As a result, the local potential fluctuation leads to electron-rich and hole-rich puddles in graphene and a current flow by the induced carrier density [6, 92-95].

3.3.2 MoS₂ transistor

In this section, the result of an electrical characteristic measurement of one of the fabricated back-gated MoS₂ transistors is presented. The MoS₂ transistor is fabricated from an exfoliated flake on a thickness of 285 nm SiO₂/Si substrate. The

AFM measurement shows the flake thickness is 4 nm. Figure 3.8 shows an optical microscope image of the fabricated back-gated MoS₂ transistor.

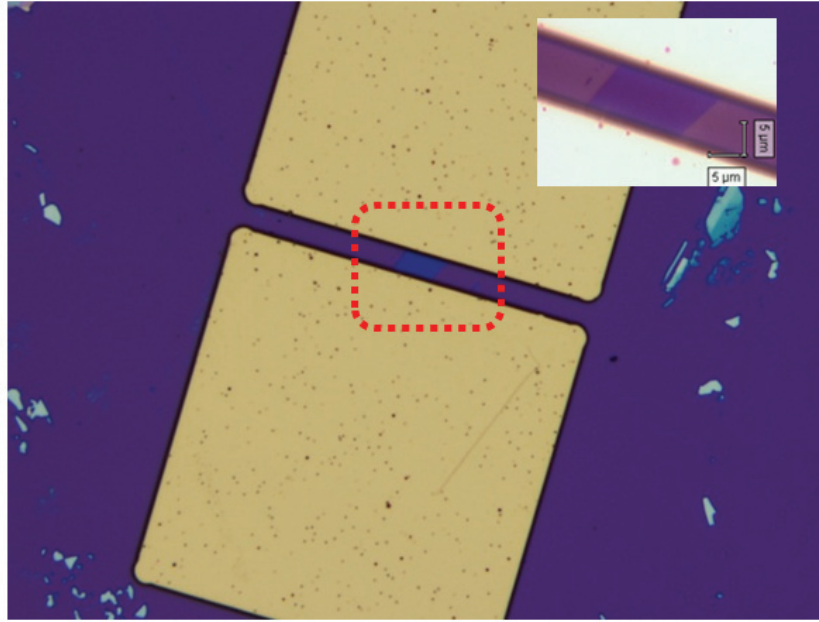


Figure 3.8: Optical microscope image of a fabricated back-gated MoS₂ transistor.

Figure 3.9 shows the results of the current-voltage measurement of the MoS₂ transistor. Unlike a top-gated device, the gate bias is applied through a global back gate. The figure contains two graphs: output characteristic curves ($I_{DS}-V_{DS}$) and transfer characteristic curves ($I_{DS}-V_{GS}$). The transfer characteristic curves show the threshold voltage is far below -10 V, which means the device exhibits n-type behavior. The field effect mobility was calculated as 4 cm²/Vs. The mobility is compatible with previously reported values for back-gated MoS₂ devices on SiO₂ [5, 96].

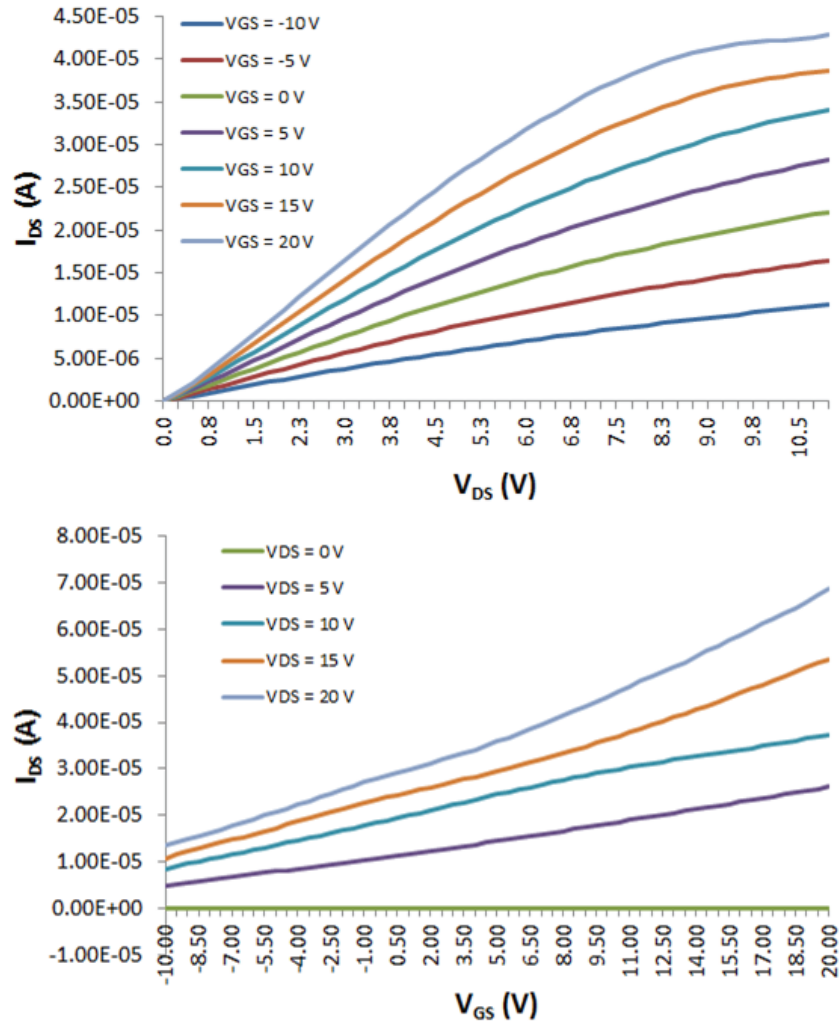


Figure 3.9: Current-voltage curves of a back-gated MoS₂ transistor on SiO₂. Top: output characteristic curves (I_{DS} - V_{DS}). Bottom: transfer characteristic curves (I_{DS} - V_{GS}).

3.4 Summary

In this chapter, the 2D material device fabrication process and the results of the fabricated transistors were discussed. The first part of the chapter discussed the device fabrication process with the 2D materials from the mask design step to the final annealing step. An issue on a dielectric disposition on the 2D material was discussed

as well. The second part of the chapter was about electrical characterization of the fabricated transistors. The output curves of graphene and MoS₂ transistors were analyzed and discussed. Graphene transistors were shown to have ambipolar transport properties and the exfoliated MoS₂ transistors were shown to have all n-type characteristics.

CHAPTER 4

ELECTRICAL CHARACTERISTICS OF MULTILAYER MOLYBDENUM DISULFIDE-GRAPHENE HETEROJUNCTION DEVICE

4.1 Introduction

Because of the unique electrical, mechanical and optical properties of graphene, interest has grown exponentially since the material was successfully exfoliated onto SiO₂ in 2004 [2, 4, 18, 97-99]. Other two-dimensional (2D) crystal materials like molybdenum disulfide (MoS₂) and hexagonal boron nitride (hBN) singularly or in combination with graphene also have intriguing properties. For example, it has been reported that when graphene is transferred onto hBN (a 2D insulating material) mobility is improved to 200 000 cm²/Vs due to the atomic flatness, low interface charge density, and small lattice mismatch (with graphene) [13]. Single-layer and multilayer MoS₂ transistors show high current ON/OFF ratios of 1×10^8 and ultralow standby power dissipation [5]. The 2D heterojunction structures of graphene in combination with other 2D materials are driving new types of applications. Initial studies are reported on vertical heterojunctions of hBN-graphene [100-102], transition metal dichalcogenides (TMDC)-graphene [103, 104], TMDC-TMDC [105], and graphene-silicon [106-108]. Applications of 2D heterostructures for memory (using MoS₂-graphene junctions [109-111]) and as photodetectors (utilizing MoS₂-graphene [112, 113] or graphene-silicon [114]) have been proposed.

In this chapter, a study of the electrical characteristics of multilayer MoS₂

field-effect transistors (FETs) with MoS₂-graphene heterojunction contacts is discussed. By studying multilayer material it is possible to determine the electrical properties, the role of contacts, and background doping of the material without additional complications due to backside dielectric junction. The principal results of this study are (1) The I-V characteristics of multilayer MoS₂-graphene heterojunction FETs can be modeled with a one-dimensional FET model similar to [115], (2) due to charge transfer from MoS₂, graphene makes a low barrier height contact to MoS₂, and (3) the electrostatics of the transistor can be self-consistently explained by two background donor levels present in the exfoliated MoS₂ where the total donor concentration is found to be $\sim 3.57 \times 10^{11} \text{ cm}^{-2}$. A free electron concentration of $\sim 3.61 \times 10^{10} \text{ cm}^{-2}$ in the material is due to partial ionization of these donors. It is believed that the donors in MoS₂ transfer charge to the graphene in agreement with [116]. Parts of this chapter have been adapted from a paper published in Nano Letters [117].

4.2 Device structure and fabrication

Heterojunction devices are fabricated on insulator/p+-Si substrate; back gate biases are applied to Si as shown in Figure 4.1. Drain and source biases are applied to the device through two contacts; either the graphene or Ti/Au, which serve as either drain or source depending on bias conditions. A graphene FET is formed between contacts #1 and #2, and a MoS₂ FET is formed between contacts #3 and #4 for additional characterization. Channel lengths of the devices are 10–20 μm implying that the

FETs are operating in the long channel regime.

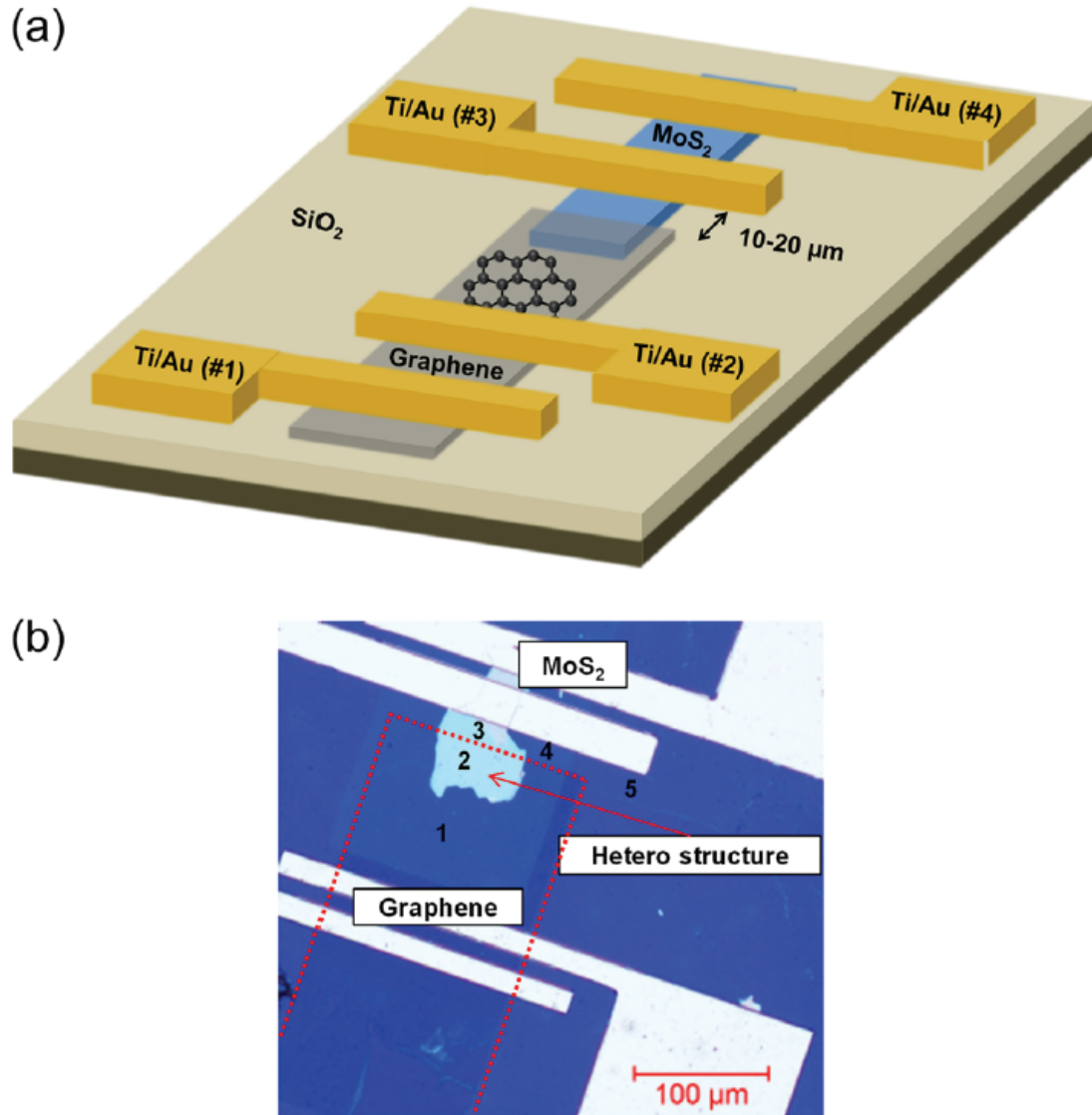


Figure 4.1: Device structure of a MoS₂-graphene heterojunction device. (a) Schematic illustration of a MoS₂-graphene heterojunction device. (b) Optical image of a graphene-MoS₂ heterojunction device. The labeled numbers indicate the following: (1) graphene with the red dotted line, (2) heterojunction, (3) MoS₂, (4) SiO₂ and (5) SiO₂ with CF₄ plasma etched. A slight color difference between (4) and (5) is due to a slight different thickness of SiO₂, which was etched by CF₄ plasma.

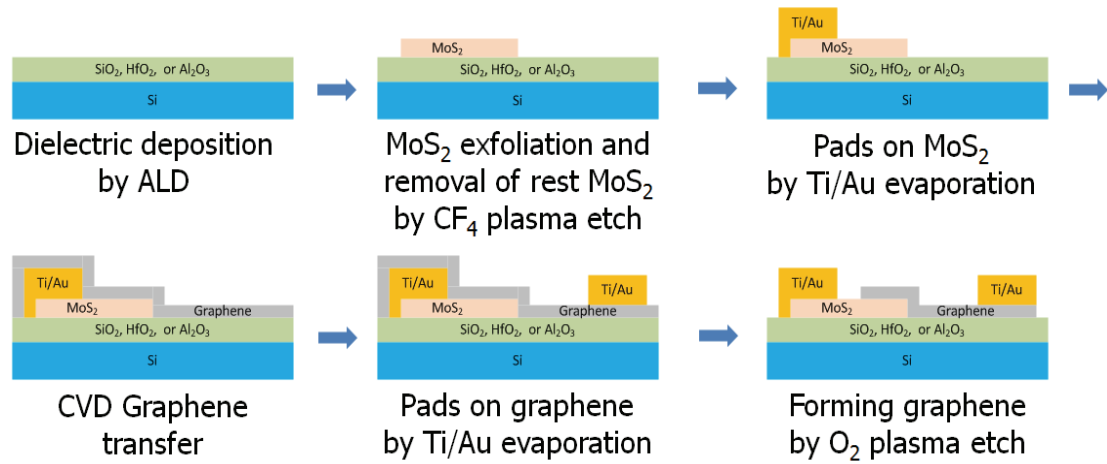


Figure 4.2: Heterojunction device fabrication process steps.

The MoS₂-graphene heterojunction devices are fabricated with exfoliated MoS₂ and transferred graphene. Figure 4.2 shows the graphene-MoS₂ heterojunction fabrication process. The fabrication starts either with 100 nm thermally grown SiO₂ or deposition of 50 nm thickness of Al₂O₃ using plasma atomic layer deposition (ALD) at 200 °C. Using the “scotch-tape” technique, MoS₂ flakes are exfoliated onto the insulator/p+-Si substrates producing an active channel. The extraneous MoS₂ flakes are removed by CF₄ plasma. Metal contact pads consisting of Ti/Au (15 nm/150 nm) are deposited on the MoS₂ flakes using e-beam evaporation. Titanium is used as an adhesion layer for gold contact metal on the flakes. Atomic force microscope measurements (AFM) are made to determine the thickness of the MoS₂ flakes. After MoS₂ characterization, CVD grown graphene on copper foil is transferred onto the surface using a wet transfer method [20, 118]. Metal contact pads of Ti/Au (15 nm/150 nm) are fabricated on the transferred graphene side by evaporation. To form

a heterojunction channel graphene is patterned with oxygen plasma etching at 150 °C, while the MoS₂ flake is not etched at this condition. Finally, the device is annealed at 300 °C in 10% forming gas of Ar/H₂ for 2 h to remove photoresist residue on the surface.

4.3 Device characterization

To confirm the presence of graphene and MoS₂, Raman spectra measurements are performed on the heterojunction using a confocal Raman microscope. The Raman signature of MoS₂ (E_{2g}¹ peak at 383 cm⁻¹ and A_{1g} peak at 408 cm⁻¹) [62, 73] and graphene (D peak at 1351 cm⁻¹, G peak at 1580 cm⁻¹, and 2D peak at 2700 cm⁻¹) [61, 119, 120] are clearly present in Figure 4.3. All the Raman spectra indicate that the MoS₂ peaks are stronger than graphene peaks and high-resolution scans were done to confirm the presence of graphene. In addition, AFM measurements are done on the MoS₂ flakes. The thickness of the MoS₂ flake measured by AFM is 80 nm for one of the heterojunction transistor. Direct wafer probing was used for electrical characterizations of the devices.

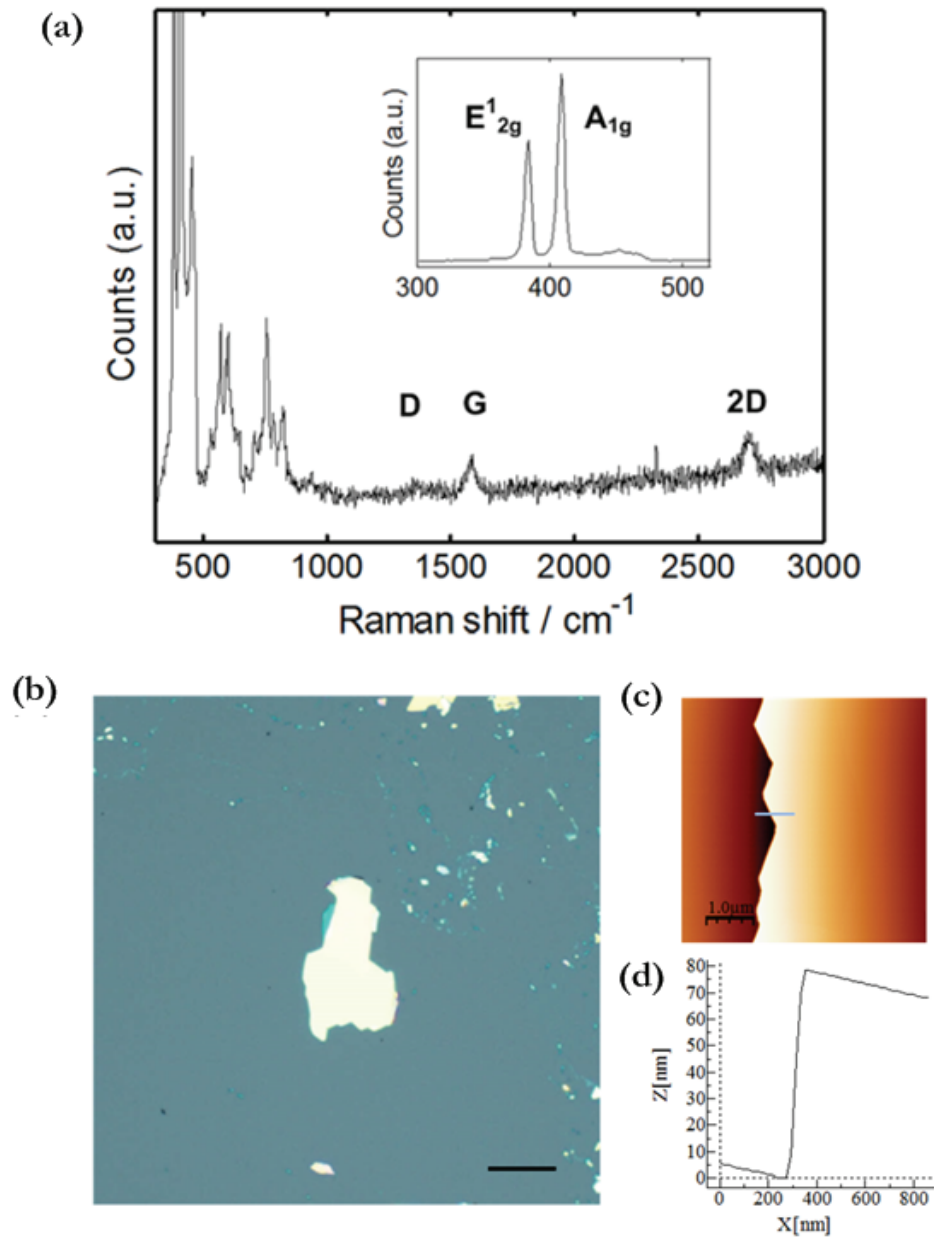


Figure 4.3: Raman and AFM characterization results. (a) Raman spectrum of the heterojunction area. Both graphene and MoS₂ Raman signatures are observed. Because the graphene Raman peaks are much weaker than MoS₂ Raman peaks, it is magnified in y-axis. The inset Raman spectrum shows the original magnitude of MoS₂ Raman peaks at less than 500 cm⁻¹. (b) Optical microscope image of the exfoliated MoS₂ flake. Scale bar, 50 μm. (c) AFM image of an edge of the MoS₂ flake. (d) The edge height profile of the flake that shows 80 nm thick MoS₂.

4.4 Current-Voltage characteristics

Measured electrical properties are shown in Figure 4.4. Room temperature current-voltage curves are measured on 80 nm thick MoS₂ transferred to 100 nm thick SiO₂ on p+-Si. The transferred graphene is monolayer thick as verified by Raman spectroscopy. The fabricated device has a MoS₂ channel length of 20 μm and the channel width of 50 μm. The I_{DS}-V_{DS} curves show different electrical behavior depending on which contact (graphene or Ti/Au) is grounded (Figure 4.4a and b). Mobility of MoS₂ determined using the following Equation 4.1 is found to be 11 cm²/Vs.

$$\mu_{FE} = \frac{g_m L}{W C_{ox} V_{DS}} \dots (4.1)$$

where $g_m = dI_{DS}/dV_{GS}$ is the transconductance, L and W are the channel length and the channel width, respectively, C_{ox} is the capacitance of the gate dielectric, and V_{DS} is the drain to source bias voltage.

The I_{DS}-V_{DS} curves (Figure 4.4a) show FET like behavior with gate bias dependency. For small drain bias (inset of Figure 4.4a), the curves look diode-like. When the MoS₂ side is grounded (Figure 4.4b) the I_{DS}-V_{DS} curves show FET like behavior but the contacts are clearly affecting the curves (inset of Figure 4.4b). The magnitude of the drain current is reduced and there is a “knee” in the curve. The I_{DS}-V_{GS} curves with graphene source contact and MoS₂ source contact are shown in Figure 4.4 Panels c and d, respectively. At lower gate biases, the curves show a quadratic dependence, while at higher gate biases (greater than V_{GS} = 1 V) the current increment slows down. The more details about the I_{DS}-V_{DS} curves are discussed in a

later section.

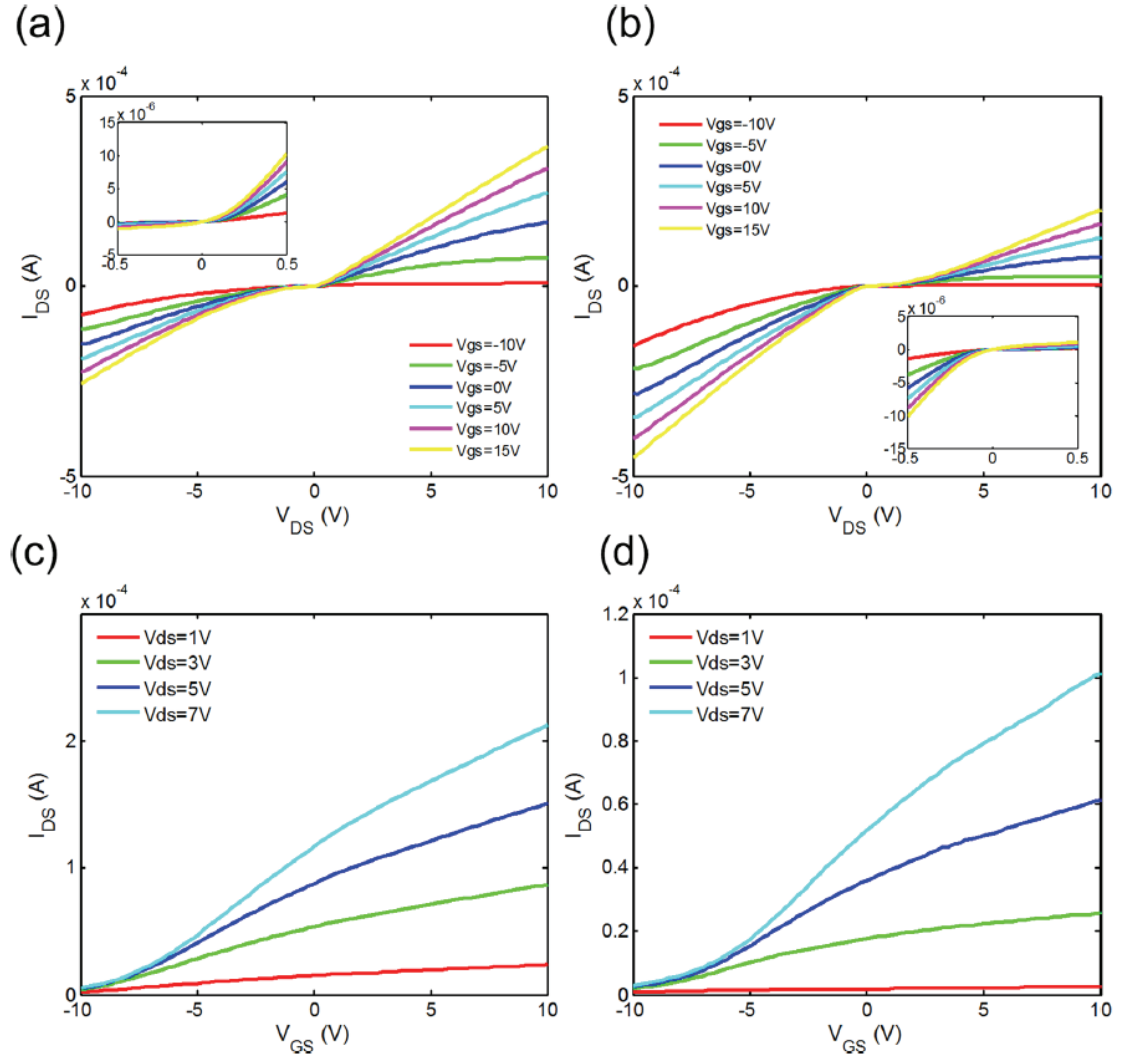


Figure 4.4: Current-voltage curves (I_{DS} - V_{DS} and I_{DS} - V_{GS}) of a back-gated heterojunction device with 80 nm thick MoS₂ on 100 nm thick SiO₂ at room temperature. (a) I_{DS} - V_{DS} of the device when graphene side is grounded, that is, source on graphene side. The inset shows the current-voltage curves in a small bias region. (b) I_{DS} - V_{DS} of the device when MoS₂ side is grounded, that is, source on MoS₂ side. The inset shows the current-voltage curves in a small bias region. (c) I_{DS} - V_{GS} of the device when graphene side is grounded. (d) I_{DS} - V_{GS} of the device when MoS₂ side is grounded.

4.5 Energy band diagrams and One-dimensional FET model

4.5.1 Energy band diagrams

Band diagrams of the MoS₂/dielectric interface are shown in Figure 4.5. The electron affinity and the energy bandgap of multilayer MoS₂ are 4.1 and 1.3 eV, respectively [121]. The work function of monolayer graphene at the Dirac point is 4.5 eV [122-124] and dielectrics, silicon dioxide (SiO₂) and aluminum oxide (Al₂O₃), have bandgaps of 8.5 and 8.8 eV with electron affinities of 0.95 and 1.25 eV, respectively [125]. The electron affinity and the bandgap of silicon are 4.05 and 1.12 eV, respectively [126].

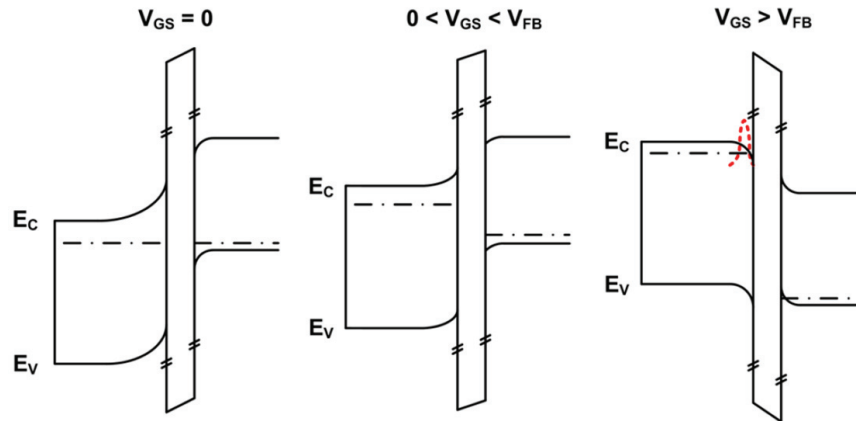


Figure 4.5: Energy band diagrams with different back gate bias conditions. Energy band diagrams of the MoS₂ channel region not covered by graphene (from left to right: MoS₂-dielectric-Si) under various back gate voltages are shown. A back gate bias (V_{GS}) changes the size of the flat region in MoS₂ (i.e., the conducting channel depth). The red dotted curve near the interface of the MoS₂/dielectric describes the accumulations of carriers.

Measured devices are normally ON and can be biased into accumulation or depletion, indicating the presence of background charge, which prevents unintentional carrier

depletion of unbiased devices.

4.5.2 Background donor density

The total donor density present in MoS₂ is calculated with the MoS₂ device with cutoff shown in Figure 4.6 using the depletion width expansion from a flat band condition to a cutoff using the following equations,

$$X_{D_MoS2} = \sqrt{\frac{2\varepsilon V_{MoS2}}{qN_D}}$$

$$N_D = \frac{2\varepsilon V_{MoS2}}{qX_{D_MoS2}^2} \dots (4.2)$$

where X_{D_MoS2} is the depletion width of MoS₂, ε is the permittivity of MoS₂, and V_{MoS2} is the effective voltage drop in MoS₂. X_{D_MoS2} in the cutoff condition is the same as the measured MoS₂ thickness because the MoS₂ is fully depleted. When the device is in cutoff, the device can be modeled as two capacitors in series, C_{MoS2} and C_{Al2O3} with $\varepsilon_{r_MoS2} = 4$, $\varepsilon_{r_Al2O3} = 9.3$, MoS₂ thickness of 8 nm, and Al₂O₃ thickness of 50 nm. The total voltage at cutoff applied across the two capacitors is the sum of the flat band voltage and the cutoff voltage. The MoS₂ depletion consists of two portions: 1) the depletion due to flat band voltage and 2) the depletion due to the cutoff voltage. The flat band voltage is calculated as 0.93 V using $V_{FB} = \chi_{Si} + E_{gSi} - \chi_{MoS2} - (E_C - E_F)_{MoS2}$ given the energy gap of Si (E_{gSi}) of 1.12 eV, the electron affinity of Si (χ_{Si}) and MoS₂ (χ_{MoS2}) of 4.05 eV and 4.1 eV, respectively, and the Fermi level of 0.14 eV below conduction band for the device. The Fermi level was calculated using $E_C - E_F = kT$

$\times \log (N_C/n)$ where N_C is the MoS₂ effective density of states [127] of $1.2 \times 10^{13} \text{ cm}^{-2}$ and n is the mobile charge density of the device at $V_{DS} = 2 \text{ V}$ and $V_{GS} = 1 \text{ V}$.

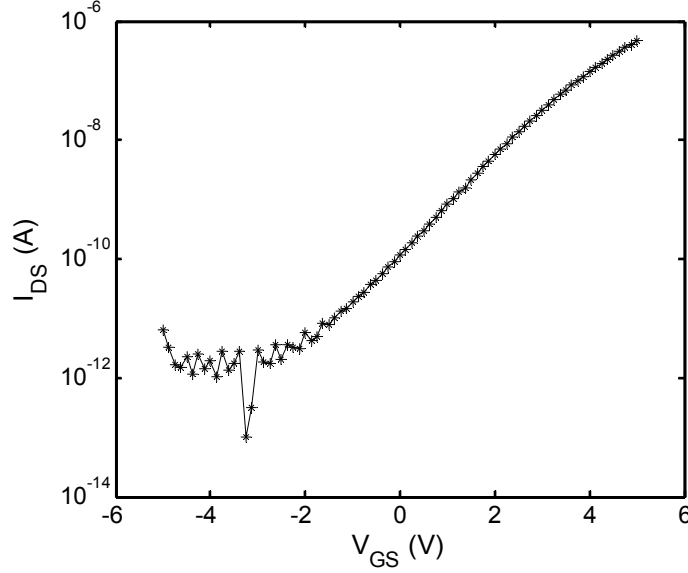


Figure 4.6: Transfer characteristic curves (I_{DS} - V_{GS}) in semi-logarithmic scale of a 8 nm thickness of MoS₂-graphene hetero-junction devices on 50 nm thickness of high-k dielectric Al₂O₃ deposited at $V_{DS} = 2 \text{ V}$.

The cutoff voltage is -2 V from Figure 4.6. V_{MoS_2} is calculated as 0.79 V using

$$V_{MoS_2} = (V_{FB} - V_{Cutoff}) \times \frac{C_{Al_2O_3}}{C_{MoS_2} + C_{Al_2O_3}}$$

and therefore, the total donor density is calculated to be $N_D \sim 3.57 \times 10^{11} \text{ cm}^{-2}$.

4.5.3 One-dimensional FET model for back gate modulation

The energy band diagram models in Figure 4.5 and a simplified one dimensional FET model with Schottky contacts in Figure 4.7 are used to explain the back gate modulation of a heterojunction device. Changing the back gate voltage modulates the thickness of the conducting layers. As the back gate voltage further increases,

electrons are accumulated near the MoS₂/dielectric interface, which will screen the back gate electric field ($V_{GS} > V_{FB}$ case in Figure 4.5).

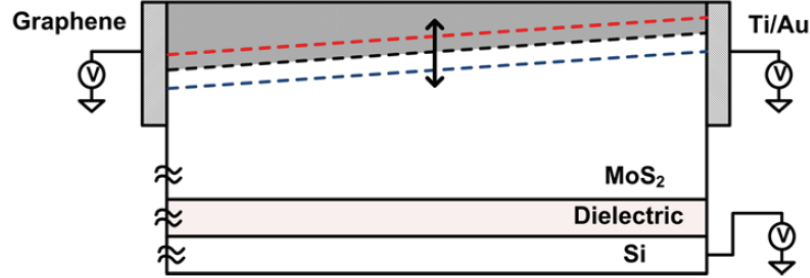


Figure 4.7: One-dimensional FET model to describe the change of channel depth by a back gate bias with a V_{DS} applied. The arrow indicates the movement of channel depth by the applied back gate bias. The length change of the flat region in MoS₂ in the energy band diagram of Figure 4.5 corresponds to the depth change of the channel.

4.6 Ionized mobile charge density

The total ionized mobile charge density at $V_{DS} = 3$ V and $V_{GS} = 0$ V is calculated for the device of Figure 4.4 using the following Equation 4.3,

$$I_D = V_{DS}(q\mu n)(t_{MoS_2} - X_D) \left(\frac{W}{L}\right) \dots (4.3)$$

where I_D is the drain current, μ is the mobility, t_{MoS_2} (80 nm) is the thickness of the MoS₂ (i.e., maximum channel depth), X_D is the depleted channel depth at a gate bias of zero volt and W/L (2.5) is the width-to-length ratio of the device. The calculated ionized mobile charge density, n , is $\sim 3.61 \times 10^{10} \text{ cm}^{-2}$ at room temperature, which means that about 10% of the total donor density, $N_D \sim 3.57 \times 10^{11} \text{ cm}^{-2}$, is ionized and contributes to the current. Table 4.1 shows the variation in ionized charge as a function of temperature.

Table 4.1: Estimated total ionized mobile carrier density for different temperatures.

Ionized mobile carrier density								
Temperature	120K	160K	200K	240K	280K	320K	360K	400K
Mobility (cm^2/Vs)	11.99	11.61	11.55	11.80	11.99	11.46	10.53	8.93
n ($\times 10^{10}$) cm^{-2}	2.28	2.74	3.07	3.22	3.45	3.78	4.76	6.10
Ionization (%)	6.39	7.70	8.63	9.05	9.67	10.62	13.37	17.16

4.7 Two donor levels model

Figure 4.8 shows a plot of $\log [I_{DS}]$ versus $1/kT$ of the device.

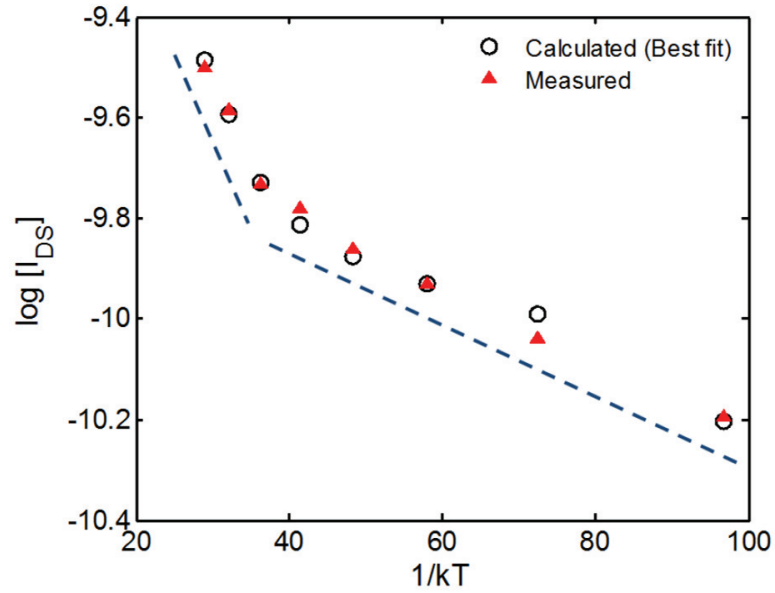


Figure 4.8: Two donor levels from temperature dependent measurement. The $\log[I_{DS}]$ versus $1/kT$ plot of the measured current and the best fit calculated current with different temperatures (120–400 K) at a bias condition, $V_{DS} = 3$ V and $V_{GS} = 0$ V. The blue dotted guide lines indicate two different slopes (i.e., two different donor levels) are present; one is a deep donor level and the other is a shallow donor level. The calculated data show the best fit to the measured data. The optimum values of the deep donor density (N_{D1}) and the shallow donor density (N_{D2}) are 3.2×10^{11} and $3.3 \times 10^{10} \text{ cm}^{-2}$, respectively, and the deep donor level and the shallow donor level from the conduction band are 0.27 and 0.05 eV, respectively.

Two different slopes can be fitted implying that two donor levels are present. Previous studies in the literature have discussed the nature of impurities in MoS₂ where a possible role of rhenium impurities and sulfur vacancies has been investigated [116, 128]. The measured donor levels are possibly from one or two (intrinsic or extrinsic) donor sources. The two different donor levels and concentrations are calculated from Fermi-Dirac (F-D) statistics using the following equations,

$$n = (1 - f(E_1, E_F))N_{D1} + (1 - f(E_2, E_F))N_{D2} \dots (4.4)$$

$$N_{D1} + N_{D2} = N_D \dots (4.5)$$

where $f(E_n, E_F)$ is the F-D function for a donor level of energy E_n , n is the total ionized mobile charge density from Table 4.1, N_{D1} and N_{D2} are donor concentrations for the two donor levels and N_D is the total donor density. The Fermi level is determined from the measured values of n using an effective density of states for MoS₂ of $1.2 \times 10^{13} \text{ cm}^{-2}$ [127]. Table 4.2 shows the calculated parameters.

Table 4.2: The calculated ionized mobile carrier density from each donor level using Fermi-Dirac (F-D) statistics for different temperatures

Calculated ionized mobile charge density from F-D statistics								
Temperature	120K	160K	200K	240K	280K	320K	360K	400K
$E_C - E_F$ (eV)	0.055	0.075	0.096	0.118	0.140	0.161	0.177	0.192
$1-f(E_1)$	8.84E-10	6.83E-07	3.89E-05	0.001	0.004	0.018	0.047	0.092
$1-f(E_2)$	0.692	0.885	0.945	0.969	0.979	0.984	0.985	0.985
$(1-f(E_1))N_{D1} (\times 10^{10}) \text{ cm}^{-2}$	2.86E-08	2.21E-05	0.001	0.020	0.140	0.584	1.508	2.979
$(1-f(E_2))N_{D2} (\times 10^{10}) \text{ cm}^{-2}$	2.250	2.880	3.072	3.150	3.184	3.201	3.204	3.205

Using an iterative process, optimum values of N_{D1} , N_{D2} , E_1 , and E_2 are found that fit the data. The optimum values of deep donor density (N_{D1}) and shallow donor density (N_{D2}) are found to be 3.2×10^{11} and $3.3 \times 10^{10} \text{ cm}^{-2}$, respectively, and the deep donor level and the shallow donor level are found to be 0.27 and 0.05 eV measured from the conduction band edge.

The high donor concentrations in MoS₂ can explain the doping of graphene by MoS₂ [116]. The graphene Fermi level shift from the Dirac point is determined to be 0.17 eV in thermal equilibrium, and this value is obtained from the graphene- MoS₂ junction barrier height (discussed below) and the bulk Fermi level location in MoS₂. The Fermi level shift in graphene is due to charge transfer from MoS₂. The graphene doping concentration of $2 \times 10^{12} \text{ cm}^{-2}$ based on the graphene Fermi level position is estimated using Figure 4.9 [129]. The high concentration of deep donors effectively pins the interface Fermi level. Figure 4.10 summarizes the findings.

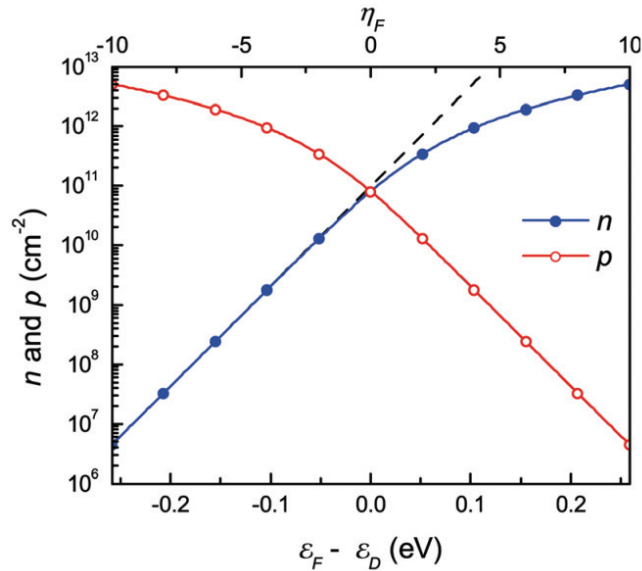


Figure 4.9: Graph of electron concentration (n) and hole concentration (p) versus Fermi energy relative to Dirac energy ($\epsilon_F - \epsilon_D$). Adapted from [129].

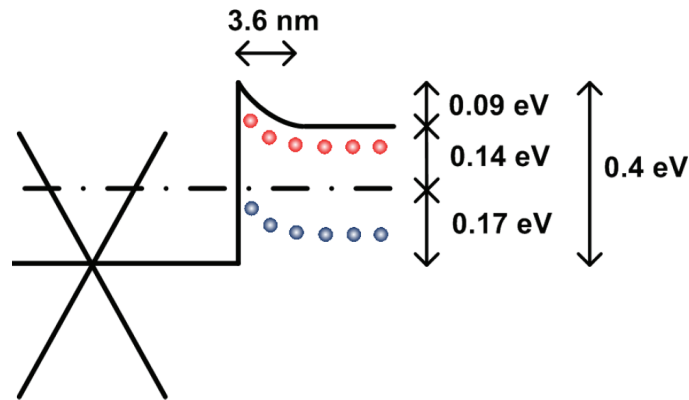


Figure 4.10: Energy band diagram model at the graphene-MoS₂ interface. Energy band diagram of the MoS₂ covered by graphene (from left to right: graphene-MoS₂) is shown. The small circles in MoS₂ indicate two dominant donor levels in MoS₂. The deep donor level (blue circle) is located at 0.27 eV from the conduction band and the shallow donor level (red circle) is located at 0.05 eV from the conduction band.

4.8 Charge transport mechanism

4.8.1 Energy band diagram on each junction

Figure 4.4a mentioned in the earlier section shows the output characteristics obtained when the graphene terminal is grounded. For positive V_{DS} , the electrons see the graphene-MoS₂ interface as the barrier to injection at the source region but no barrier to collection at the drain region. On the other hand, for negative V_{DS} , the electrons see the Ti-MoS₂ interface as the barrier to injection at the drain region, but no barrier to collection at the source region as shown in Figure 4.11.

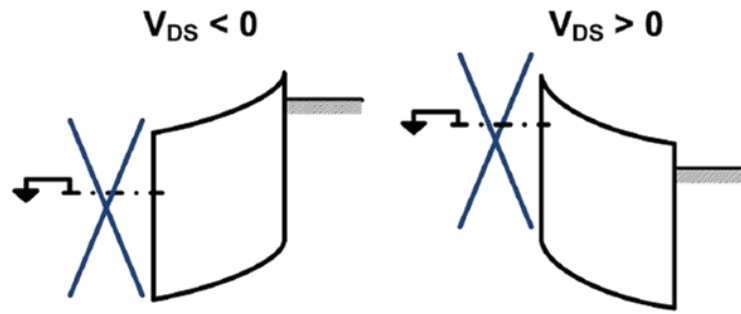


Figure 4.11: Energy band diagrams with different drain bias conditions. Energy band diagrams (from left to right: graphene-MoS₂-Ti/Au) in a reverse drain bias and in a forward drain bias condition, respectively, when the graphene side is grounded are shown.

The asymmetry of the current behavior in low bias region is due to the barrier height difference between the graphene-MoS₂ heterojunction and the Ti-MoS₂ junction. In order to extract the Schottky barrier heights, temperature dependent I_{DS} - V_{DS} ($V_{GS} = 0$ V) measurements were made as shown in Figure 4.12. At low drain bias voltages the current is strongly temperature dependent, while at high voltages I_{DS} is temperature independent. Therefore, at low V_{DS} the resistance of the device is dominated by thermionic or thermionic-field emission of the interface barrier (strongly temperature dependent), while at high V_{DS} the barrier transport is by field emission (temperature independent). In the field emission region, the series resistance of the channel dominates.

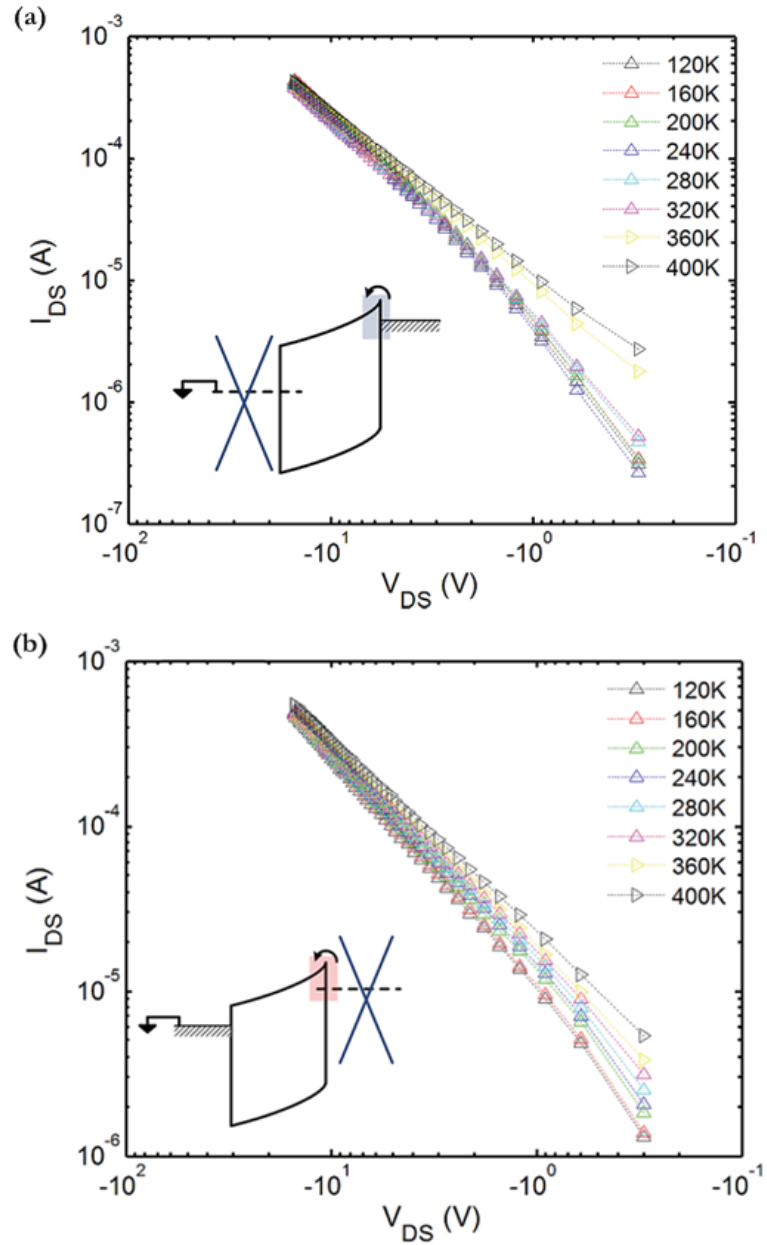


Figure 4.12: Log-Log scale plots of I_{DS} - V_{DS} in reverse bias conditions (at $V_{GS} = 0$ V) with graphene or MoS₂ grounded. (a) I_{DS} - V_{DS} curves with temperature-dependent measurement when graphene is grounded. The energy band diagram (inset) shows the Ti-MoS₂ Schottky barrier in a reverse bias region. (b) I_{DS} - V_{DS} curves with temperature dependent measurement when MoS₂ is grounded. The energy band diagram (inset) shows the graphene-MoS₂ Schottky barrier in a reverse bias region.

4.8.2 Channel Resistance vs. Schottky Barrier Resistance

Figure 4.13 shows the total resistance versus V_{DS} of the device with dominating resistance regions labeled. The total resistance consists of the Schottky barrier resistance, the MoS₂ channel resistance and graphene contact resistance. Prior measurements of the graphene resistance utilizing the graphene transistor fabricated on the same substrate (Figure 4.1a contacts #1 and #2) determined that the resistance is less than 6% of the total resistance. If the channel resistance is greater than the Schottky barrier resistance, the temperature dependence of the current is attributed to the MoS₂ channel resistance (flat regions of Figure 4.13) [115]. The total resistance is much higher in a lower V_{DS} than the relatively flat region of the total resistance in a higher V_{DS} . That is, at low V_{DS} the Schottky barrier dominates the total resistance. Note the difference in the temperature dependence in the respective regions; large temperature dependence in the barrier dominated region and small dependence in the channel dominated region. In the barrier dominated region, the carrier transport mechanism becomes thermionic or thermionic-field emission and the Schottky barrier height can be extracted at low V_{DS} . As a result, $V_{DS} = 3$ V is used for donor level extraction in the previous discussion on donor levels, and $V_{DS} = -0.1$ V is used for the Schottky barrier height extraction in the next section.

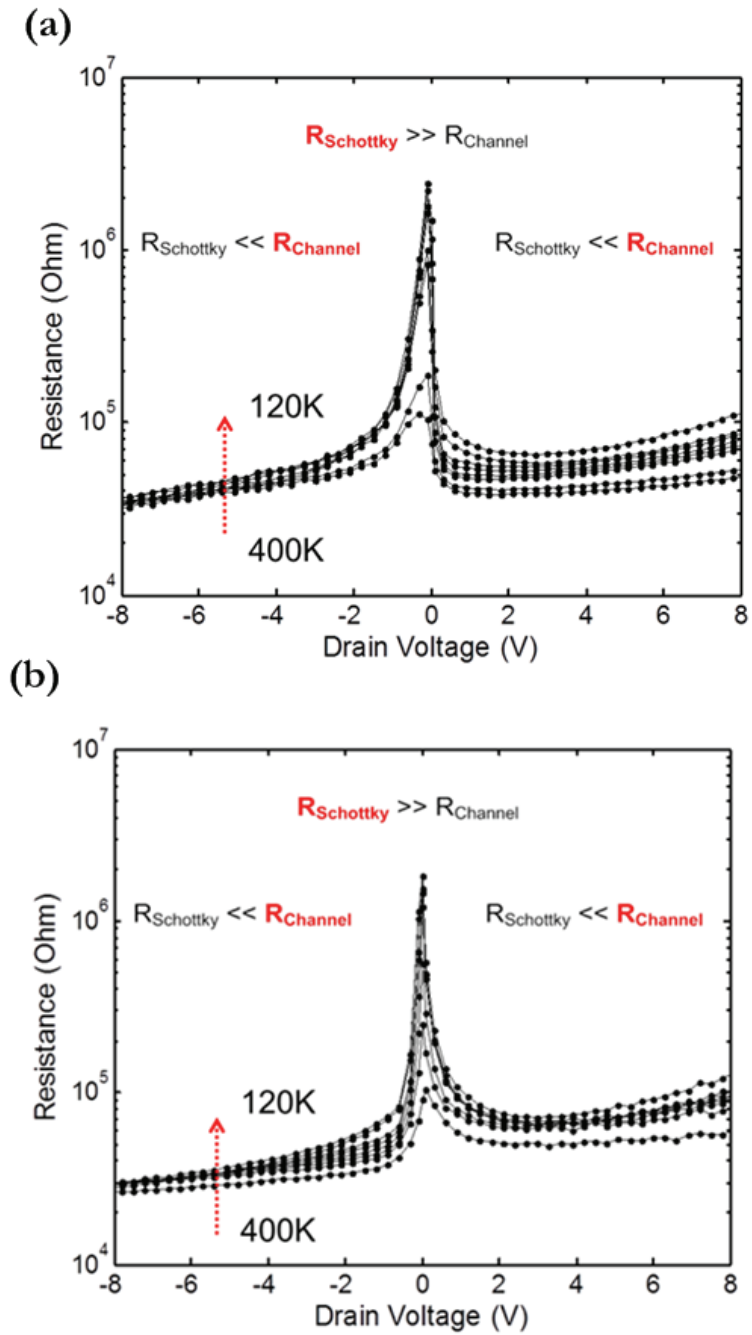


Figure 4.13: Plot for total resistance vs. V_{DS} at a fixed $V_{GS} = 0$ V with different temperatures (120K-400K with 40K step). (a) Resistance changes of the device when graphene side is grounded. (b) Resistance changes of the device when MoS₂ side is grounded.

4.8.3 Schottky barrier heights on each junction

Two methods are used for Schottky barrier height extraction. Method 1 is based on a thermionic emission model and Method 2 is based on the thermionic field emission model [130].

4.8.3.1 Method 1 (Thermionic emission model)

Barrier height extraction method uses the Schottky diode equation for a thermionic emission [131],

$$I_D = \left[AA^* T^2 \exp\left(\frac{-q\phi_B}{kT}\right) \right] \left[\exp\left(\frac{qV_{DS}}{kT}\right) - 1 \right] \dots (4.6)$$

where ϕ_B is the junction barrier height, A is the junction area, A^* is the effective Richardson constant, k is the Boltzmann constant, T is the temperature and V_{DS} is the applied bias. Figure 4.14 shows the Arrhenius plot ($\log [I_S/T^2]$ vs. $1/kT$) for the barrier height estimate. A small reverse bias ($V_{DS} = -0.1$ V) is applied to minimize the image force barrier lowering effect as well as the channel resistance effect as described in the Channel Resistance vs. Schottky Barrier Resistance section above. The barrier heights ϕ_B (the slopes of the plot) are extracted for each junction; 136 meV for the Ti-MoS₂ junction and 78.3 meV for the graphene-MoS₂ junction, respectively. The plot deviates from the linear fit line and becomes weakly temperature dependent at around 240K and below. In the low temperature regime, temperature independent field emission dominates.

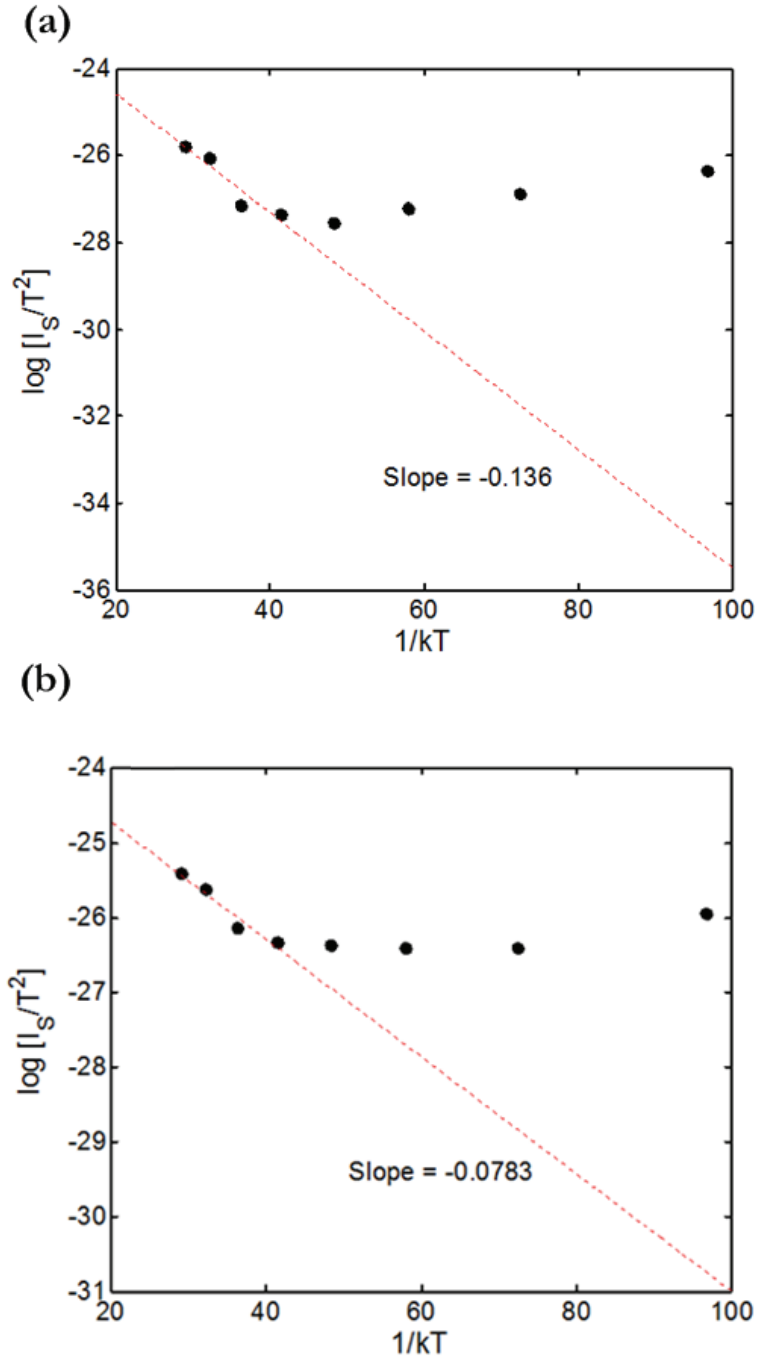


Figure 4.14: The Arrhenius plots for the barrier height extractions using thermionic emission model (Method 1) at $V_{DS} = -0.1$ V. (a) The barrier height of Ti-MoS₂ junction is 136 meV. (b) The barrier height of graphene-MoS₂ junction is 78.3 meV.

4.8.3.2 Method 2 (Thermionic field emission model)

The reverse saturation current equation is expressed as follows [130],

$$I_S = \frac{AA^*(\pi E_{00})^{1/2}}{kT} \left[-E + \frac{E_B}{\cosh^2\left(\frac{E_{00}}{kT}\right)} \right]^{1/2} \times \exp\left(-\frac{E_B}{E_0}\right) \dots (4.7)$$

where $E_{00} = \frac{qh}{4\pi} \left[\frac{N_D}{m^* \epsilon} \right]^{1/2}$ and $E_0 = E_{00} \coth\left(\frac{E_{00}}{kT}\right)$. A^* is the effective Richardson constant, A is the area of the junction, k is the Boltzmann constant, T is the temperature, h is the Planck constant, m^* is the effective mass of MoS₂, ϵ is the permittivity of MoS₂, E is the potential energy associated with an applied bias between the junction, E_B is the barrier height, and N_D is the impurity concentration. By constructing the Arrhenius plot ($\log [|I_S| \cosh(E_{00}/kT)/T]$ vs. $1/E_0$) as described in the reference [130], the barrier height for each junction is shown in Figure 4.15. From this method, the barrier heights (the slopes of the plot) are extracted; 398 meV for the Ti-MoS₂ junction and 232 meV for the graphene-MoS₂ junction, respectively.

The barrier heights, 136 meV for Ti-MoS₂ junction and 78.3 meV for graphene-MoS₂ junction, extracted using Method 1 are about one-third of the barrier heights, 398 meV and 232 meV, for the corresponding junctions using Method 2 for this device. The results from both the methods show that the barrier height of a graphene-MoS₂ junction is around 60% lower than the barrier height of a Ti-MoS₂ junction.

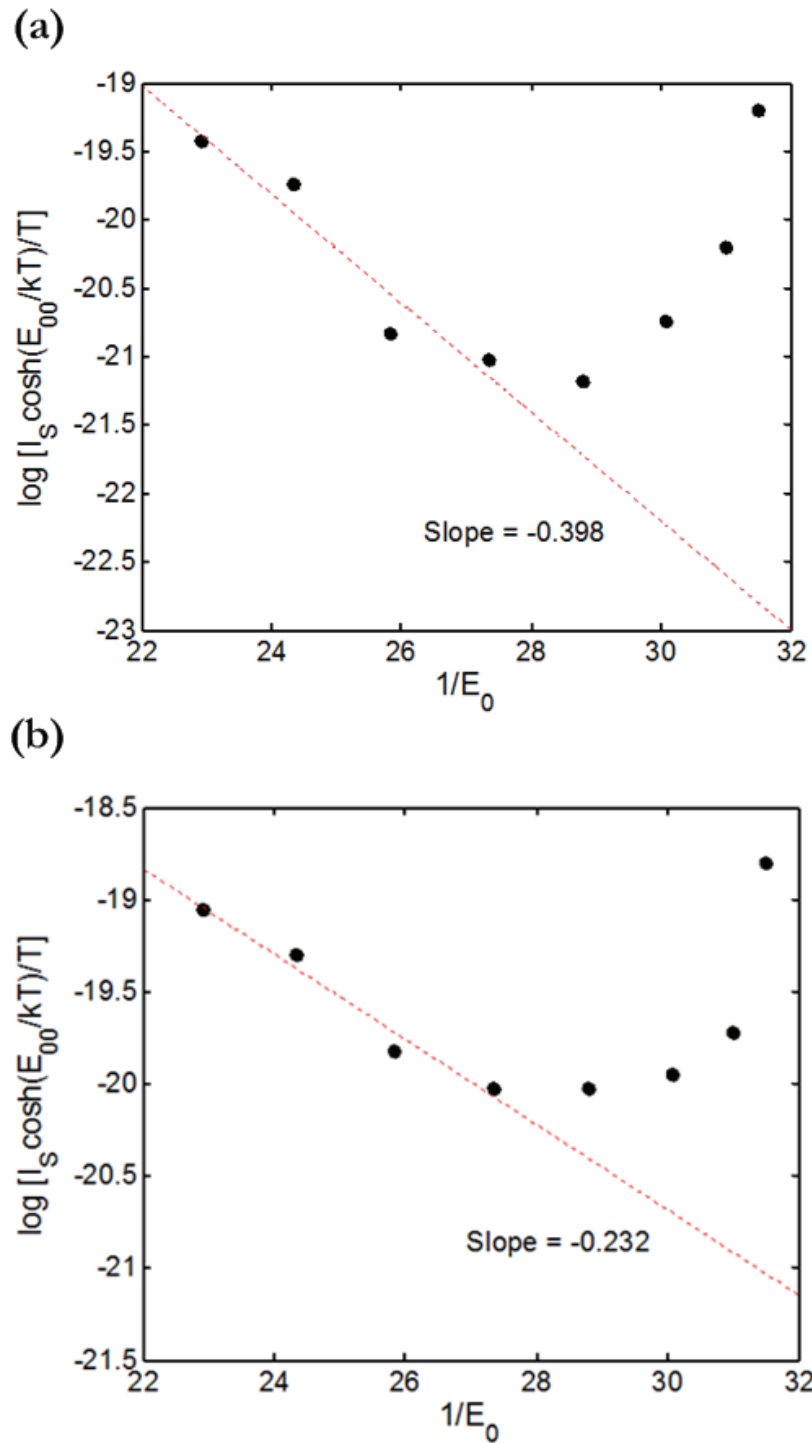


Figure 4.15: The Arrhenius plots for the barrier height extractions using thermionic field emission model (Method 2) at $V_{DS} = -0.1$ V. (a) The barrier height of Ti-MoS₂ junction is 398 meV. (b) The barrier height of graphene-MoS₂ junction is 232 meV.

4.8.3.3 Thermionic emission model versus thermionic field emission model

In summary, the thermionic emission model [131] yields a value of 0.08 eV for the graphene-MoS₂ interface and 0.14 eV for the Ti-MoS₂ barrier, and the thermionic field emission model [130] yields a barrier height of 0.23 eV for the graphene-MoS₂ interface and 0.40 eV for the Ti-MoS₂ interface. Because of the large concentration of deep donors and the resulting high electric field at the interface, the thermionic field emission model represents the Schottky barrier heights more accurately. As a result, the 0.40 eV barrier height predicted for the Ti-MoS₂ interface is higher than that predicted in [132].

4.9 Effect of changing ground contact location

When the ground contacts are switched, the current characteristics of the device are dramatically changed. For positive V_{DS} the electrons will now see the Ti-MoS₂ Schottky barrier to injection at the source region but no barrier to collection at the drain region. On the other hand, for negative V_{DS} the electrons will see the graphene-MoS₂ Schottky barrier to injection at the drain region but no barrier to collection at the source region. As in the case of the grounded graphene contact above, the asymmetry of the current behavior is due to the barrier height difference between the graphene-MoS₂ heterojunction and the Ti-MoS₂ junction.

4.10 Summary

In this chapter, heterojunction transistors with multilayer MoS₂-graphene were designed and fabricated to study the behavior of electrical transport properties and the operation mechanism of thick heterojunction devices. Firstly, the current-voltage measurement results were discussed. Secondly, the energy band models were used to explain the back gate modulation. Thirdly, a two donor-levels model was proposed and discussed. Lastly, the charge transport mechanisms on each junction—graphene-MoS₂ heterojunction and Ti-MoS₂ junction—were discussed. The concentration of unintentional donors in exfoliated MoS₂ was determined to be $\sim 3.57 \times 10^{11} \text{ cm}^{-2}$ with two dominant donor levels, one at 0.27 eV and the other at 0.05 eV below the conduction band. The high concentration of deep donors effectively pins the interface Fermi level in thermal equilibrium. The results of current-voltage measurements show that the electronic behavior of the device is strongly influenced by the contacts. The charge transport mechanism in both junctions was determined to be either thermionic field emission or field emission depending on bias voltage and temperature in a low bias regime. On the basis of a thermionic field emission model, the barrier height at the graphene-MoS₂ interface was determined to be 0.23 eV, while the barrier height at the Ti-MoS₂ interface was 0.40 eV. The value of the Ti-MoS₂ barrier reported here is higher than previously reported values [132], which did not include the effects of thermionic field emission.

CHAPTER 5

OPTICAL CHARACTERISTICS OF MOLYBDENUM DISULFIDE- GRAPHENE HETEROJUNCTION DEVICE

5.1 Introduction

In the past decade, graphene-based devices have been of great interest due to superior mobility ($> 200,000 \text{ cm}^2/\text{Vs}$ at room temperature), broad spectral absorption (2.3% per layer), and flexibility [2, 4, 17, 78, 133, 134]. Other two-dimensional (2D) crystal materials such as molybdenum disulfide (MoS_2) and hexagonal boron nitride (hBN), individually or in combination with graphene, are inspiring new types of applications in flexible electronics, tunneling devices, and optoelectronics [51, 135-139]. For example, a MoS_2 transistor made from a single layer flake shows an ultralow standby current and a current on-off ratio of 1×10^8 [5]. Hexagonal boron nitride (hBN), due to the small lattice mismatch with graphene and atomically thin flat surface, could be a good dielectric for realizing high-speed graphene electronics [13]. Two-dimensional heterojunction structures of transition metal dichalcogenides have intriguing properties. Applications of 2D heterojunction structures on MoS_2 -silicon [114, 140], MoS_2 -graphene [141, 142], MoS_2 - WS_2 [143], and WSe_2 - MoS_2 [144, 145] as photodetectors have been proposed.

The mechanism of photocurrent generation in three-dimensional heterojunction structures is most often the photovoltaic effect (PV). However, due to the ultrafast carrier relaxation time of graphene ($< 10\text{--}150 \text{ fs}$) after photo excitement [146, 147],

carrier transport between graphene and MoS₂ is unlikely to happen before energy relaxation of the electron-hole pairs. In studies of metal graphene photodetectors, the dominate mechanism of current collection was found to be photovoltaic at low carrier density but thermoelectric effects and bolometric effects at high carrier density [148]. In studies of MoS₂ field effect transistors, a large photothermal voltage (generated by the photothermal electric (PTE) effect) was found at the metal MoS₂ junction [149]. The induced potential is due to a large mismatch between the Seebeck coefficients of the metal and MoS₂. Prior work on photoresponse of MoS₂-graphene junctions has focused on absorption in the MoS₂ layer with subsequent transfer of electrons and holes to adjacent graphene regions [112, 141, 150]. This work focuses on absorption in the graphene layer of the heterojunction structure. The major result of this work is finding and characterizing the role of the PTE effect in photocurrent generation in graphene-MoS₂ heterojunction FETs.

As a result of this study, the PTE effect determines the response of the graphene-MoS₂ junction for light below the bandgap of MoS₂ and enhances the graphene-MoS₂ response for light above the bandgap of MoS₂. Because the PTE can modulate the junction voltage, the photocurrent depends exponentially on the product of the Seebeck coefficient difference and the light induced temperature gradient.

5.2 Device and fabrication

An optical microscope image and a schematic view of the graphene-MoS₂ heterojunction device are shown in Figures 5.1a and b.

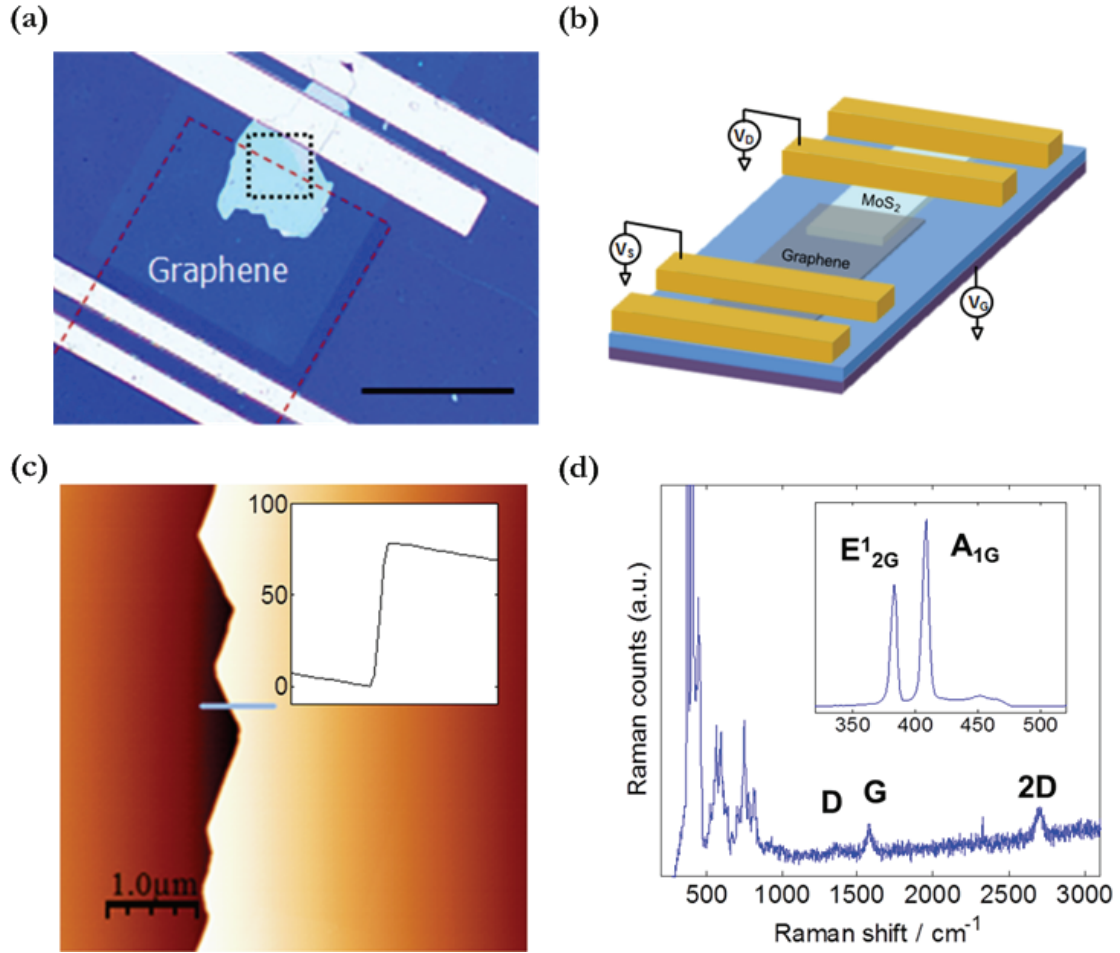


Figure 5.1: Device structure and characterization results of a graphene-MoS₂ heterojunction device. (a) Optical image of the device. The black dotted box is the raster laser scanned area. The red dotted area indicates graphene area. Scale bar, 100 μm . (b) Schematic of the graphene-MoS₂ heterojunction device. (c) AFM image of an edge of the MoS₂ flake. The edge height profile of the flake shows 80 nm thick MoS₂. (d) Raman spectrum of the heterojunction area. Both graphene and MoS₂ Raman signatures are observed. Because the graphene Raman peaks are much weaker than MoS₂ Raman peaks, it is magnified in y-axis. The inset Raman spectrum shows the original magnitude of MoS₂ Raman peaks at less than 500 cm^{-1} .

The heterojunction device is fabricated using an exfoliated MoS₂ flake from a geological crystalline MoS₂ chunk and transferred graphene from CVD-grown graphene on a Cu foil. Thermal SiO₂ is deposited on a highly doped p-Si wafer with

a thickness of 100 nm. MoS₂ flakes are exfoliated onto the substrate using the Scotch tape method followed by CF₄ plasma etching to remove extraneous MoS₂ flakes. MoS₂ flake thickness of 80 nm is measured with an atomic force microscope (AFM) shown in Figure 5.1c. Metal contacts are deposited on the MoS₂ flakes using e-beam evaporation of Ti/Au (15 nm/150 nm). Thin titanium is used as an adhesion layer for the gold deposition. Graphene on the Cu foil is then transferred onto the surface using a wet transfer method followed by Ti/Au (15 nm/150 nm) e-beam evaporation on the transferred graphene surface. The heterojunction channel is patterned by oxygen plasma etching at 150 °C. The exfoliated MoS₂ flake is not attacked during channel etching. The devices are annealed at 300 °C in 10% forming gas of Ar/H₂ for 2 hours to remove photoresist residues and other contaminants on the surface. Raman characterizations are performed, confirming that both MoS₂ and graphene are present on the heterojunction area. The Raman peaks of both MoS₂ and graphene are clearly shown in Figure 5.1d. In all Raman spectra, MoS₂ Raman peaks are stronger than graphene Raman peaks.

5.3 Optics setup

The photoresponse of the heterojunction device is performed by a raster laser scan over the device surface with direct probing on drain and source terminals, where the drain is on the Ti-MoS₂ contact side and the source is on the graphene-MoS₂ contact side, at room temperature. Figure 5.2 shows the optics setup for the measurements.

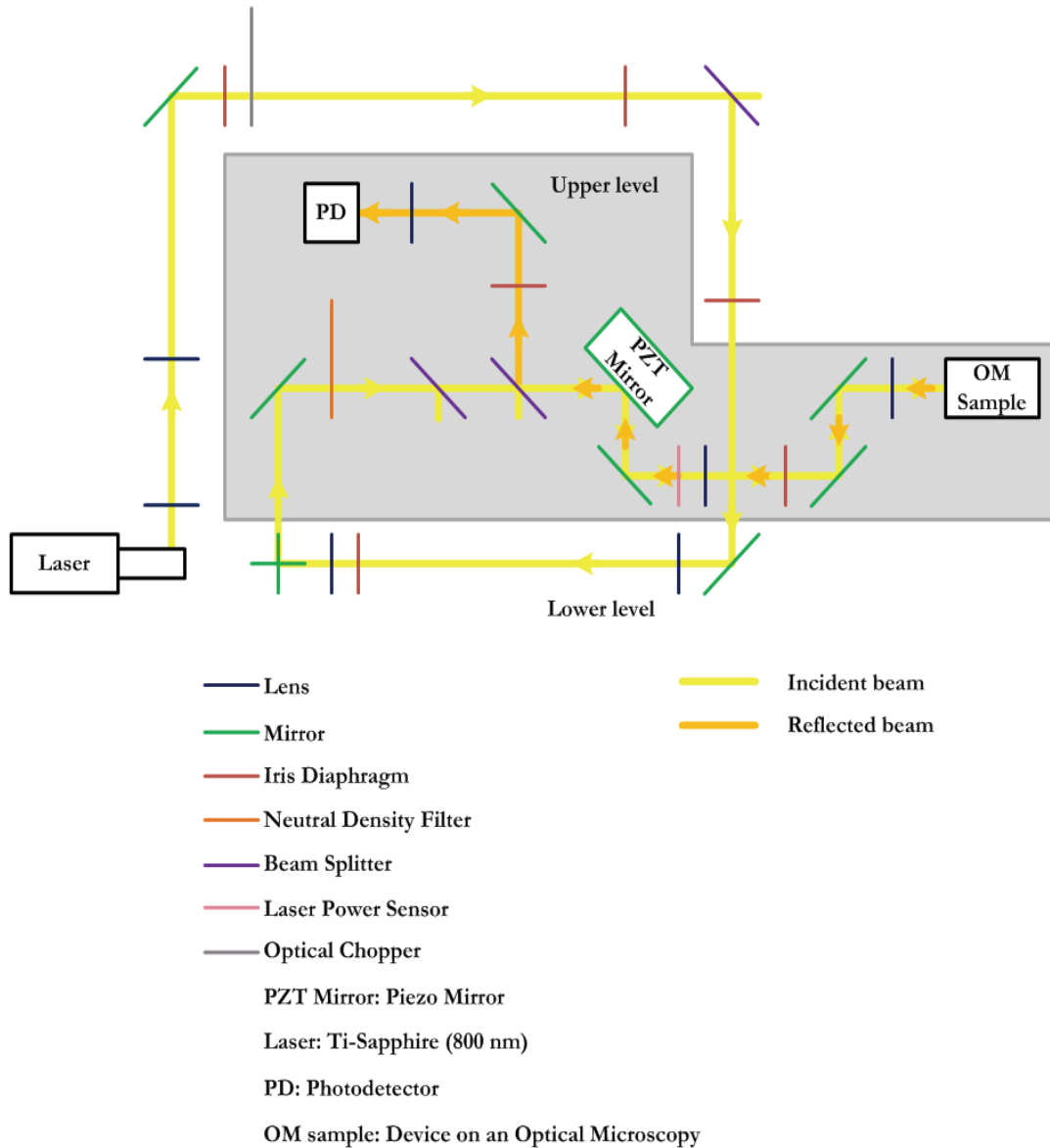


Figure 5.2: Optics setup for photoresponse measurements. The setup offers spatial resolution photoresponse measurements. The laser uses Ti-Sapphire laser fixed at 800 nm wavelength. The PZT mirror enables raster laser scanning on the sample. The photodetector detects reflected beam that gives an image of the sample. An objective lens of the optical microscope (OM) focuses the laser beam on a desired spot of the sample surface.

In this experiment, an 800 nm wavelength of Ti-Sapphire laser is used with a power of 0.43 mW. The laser beam is focused on the device surface with an objective lens

(Olympus LCPlan N 50x), which provides a beam diameter of approximately 1.5 μm . An optical chopper is placed on the beam path to block and pass the laser beam at a frequency of 332 Hz. The photoresponse is measured with a lock-in amplifier (Stanford Research Systems SR830) at this frequency.

5.4 Measurement Results

5.4.1 Current-voltage measurement

The heterojunction device output characteristic ($I_{\text{DS}}-V_{\text{DS}}$) is shown in Figure 5.3. The FET device exhibits n-type behavior, which is typically observed in devices fabricated with exfoliated MoS_2 [121, 151].

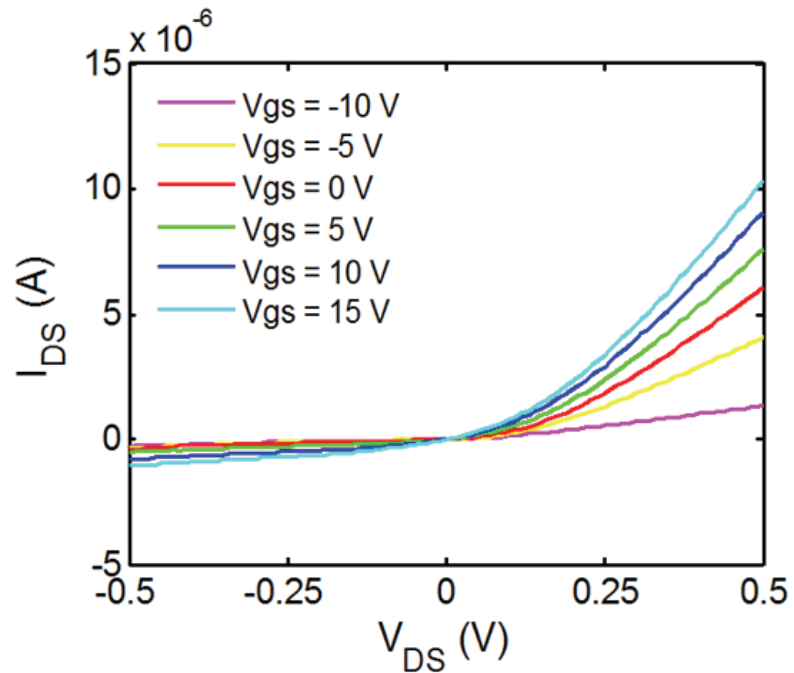


Figure 5.3: Current-Voltage curves ($I_{\text{DS}}-V_{\text{DS}}$) of the back gated heterojunction device at room temperature. The device is measured with the source grounded on graphene side.

The I-V curve can be modeled as a FET channel with Schottky barrier contacts, and the asymmetry of the output curve is attributed to the barrier height difference between the Ti-MoS₂ and graphene-MoS₂ contacts [103, 117]. The current-voltage measurement is done with the graphene side grounded. For a positive V_{DS}, the graphene-MoS₂ junction limits current flow in the positive bias. On the other hand, for a negative V_{DS}, the Ti-MoS₂ junction limits the current flow in the negative bias. The current in the positive V_{DS} is much larger than the current in the negative V_{DS}, indicating the graphene-MoS₂ junction Schottky barrier is lower than the Ti-MoS₂ junction Schottky barrier.

5.4.2 Spatial resolution photoresponse measurement

Spatial resolution photoresponse maps of the heterojunction device with different V_{DS} are shown in Figure 5.4. Region I is the graphene-MoS₂ heterojunction area; Region II is the MoS₂ channel area; and Region III is the Ti-MoS₂ junction area. In the thermal equilibrium condition where V_{DS} = 0 V and V_{GS} = 0 V, the maximum photoresponses of 0.019 mA/W and 0.032 mA/W from the photoresponse map are observed on the graphene-MoS₂ heterojunction and the Ti-MoS₂ junction, respectively. The magnitude of the photoresponses depends on the applied drain-source bias conditions. When V_{DS} = 0.3 V is applied, the maximum photoresponse of 0.139 mA/W from the photoresponse map is observed on the graphene-MoS₂ heterojunction area. On the other hand, when V_{DS} = -0.3 V is applied, the maximum photoresponse of 0.457 mA/W from the photoresponse map is observed on the Ti-MoS₂ junction area.

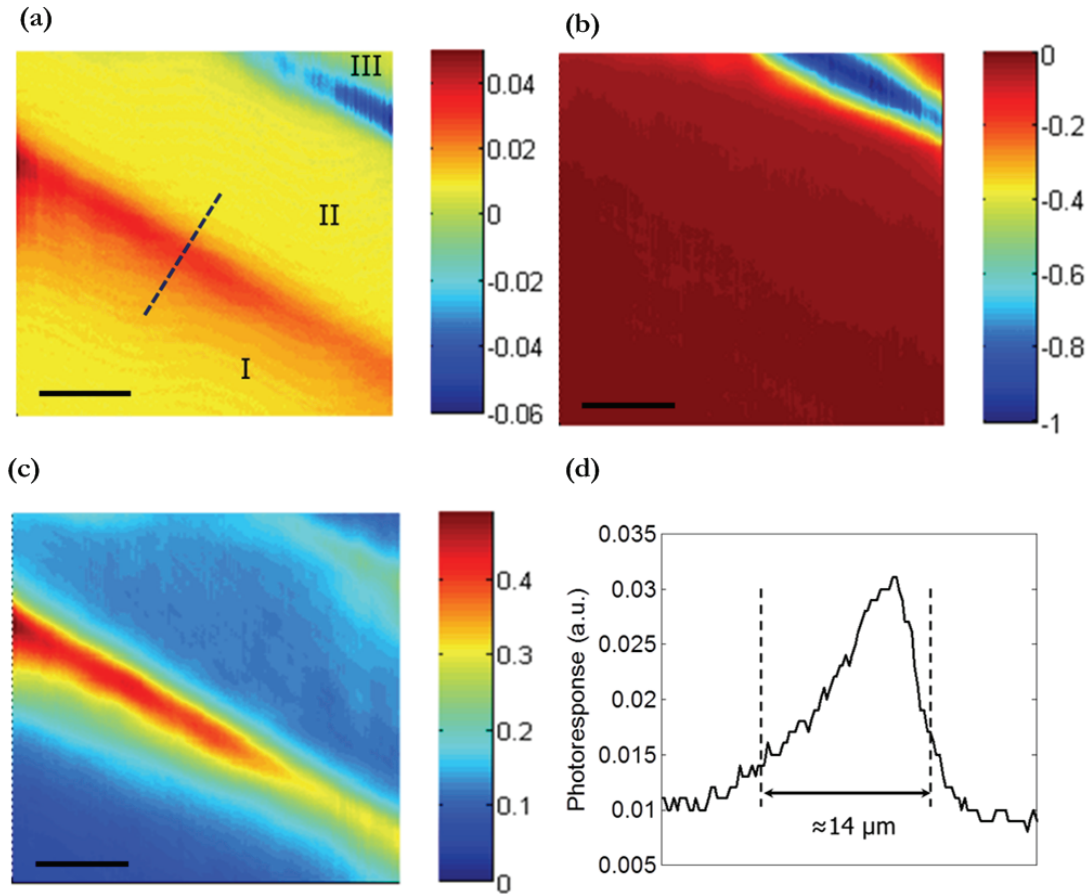


Figure 5.4: Photoresponse maps on the heterojunction area with the raster laser scan (800 nm wavelength at 0.43 mW laser power) with different biases applied. (a) The photoresponse map at $V_{DS} = 0$ V and $V_{GS} = 0$ V. Region I is the graphene-MoS₂ heterojunction region; Region II the MoS₂ channel region; and Region III the Ti-MoS₂ junction region. Photoresponse in a.u.. Scare bar, 13 μm. (b) The photoresponse map taken at $V_{DS} = -0.3$ V and $V_{GS} = 0$ V. (c) The photoresponse map taken at $V_{DS} = 0.3$ V and $V_{GS} = 0$ V. (d) Line scan of photoresponse across the heterojunction boundary from I to II in (a).

Figure 5.4d shows a line scan of photoresponse across the graphene-MoS₂ heterojunction boundary from Region I to Region II. Current enhancement due to laser illumination is observed as far as 14 μm from the edge of the graphene-MoS₂ heterojunction. This is the transfer length of the graphene-MoS₂ heterojunction.

5.4.3 Bias dependent photoresponse measurement

Figure 5.5 shows the V_{DS} dependent photoresponses after subtraction of the background photoresponse attributed to the MoS₂-only photoresponse in Region II.

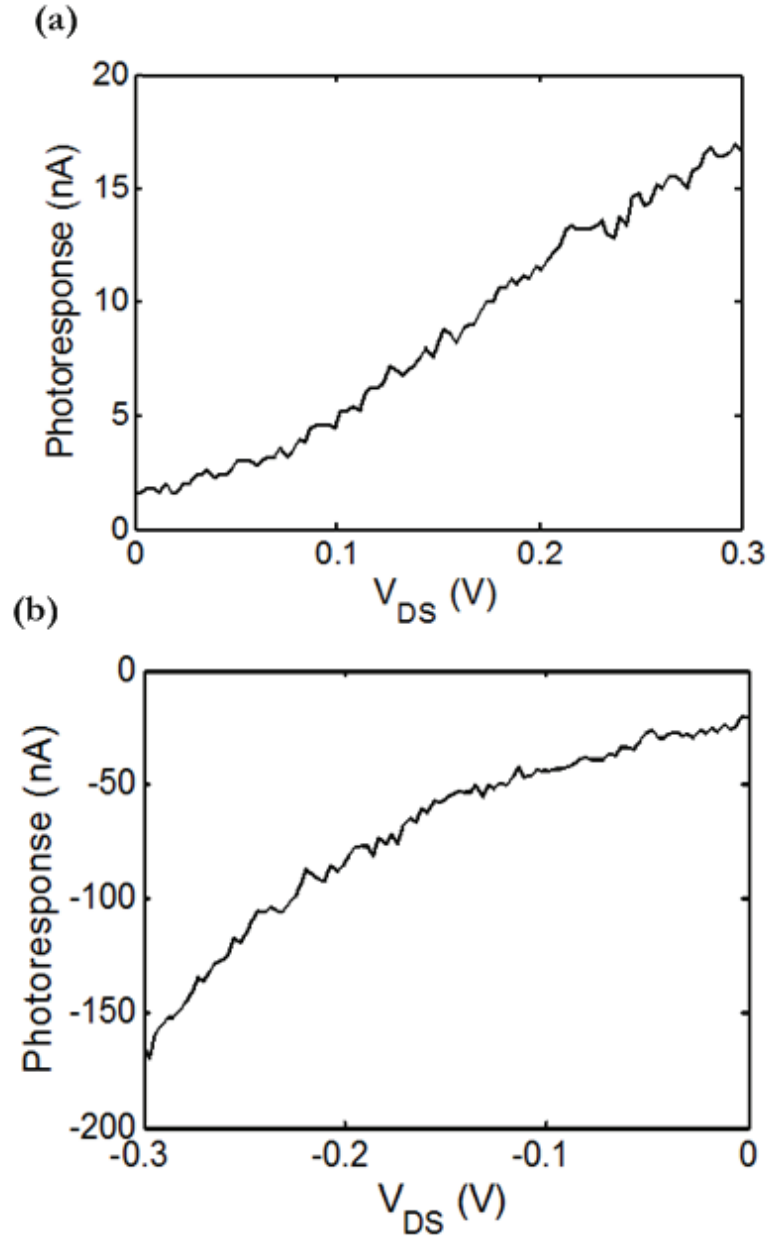


Figure 5.5: V_{DS} dependent photoresponse curves with a stationary laser illumination on each junction at $V_{GS} = 0$ V. (a) Photoresponse curve (after background subtraction) measured at one fixed point on the graphene-MoS₂ heterojunction with the bias sweep. (b) Photoresponse curve (after background subtraction) measured at one fixed point on the Ti-MoS₂ junction with the bias sweep.

The photoresponses increase as the applied bias increases for both the graphene-MoS₂ heterojunction and the Ti-MoS₂ junction. The measurements are done with the laser beam fixed on one point on each junction, with a drain-source bias at a fixed gate-source bias at 0 V. The photoresponses obtained from the stationary laser spot are different from the maximum photoresponses obtained from the spatial resolution photoresponse maps mentioned above. This is because the illuminated spots are not the same spots with the maximum photoresponses detected in the photoresponse maps.

5.5 Analysis and discussion

5.5.1 Generated voltages by the PTE effect

Equation 5.1 indicates that the PTE effect creates a voltage (V_{PTE}) due to the difference in the Seebeck coefficients between the two materials and the difference in temperature at the junction with its surroundings [149, 152].

$$V_{PTE} = (S_{Ti \text{ or } Graphene} - S_{MoS_2})\Delta T \dots (5.1)$$

where S_{Ti} , $S_{Graphene}$, and S_{MoS_2} , are the Seebeck coefficients of titanium ($\sim 7 \mu\text{V/K}$ [153]), graphene ($\sim -50 \mu\text{V/K}$ for n-type [154]), and MoS₂ ($\sim -700 \mu\text{V/K}$ for multilayer [149]) respectively, and ΔT is the local temperature increase at the junction by laser irradiation.

The photothermal-generated voltages (V_{PTE}) on the junction enable additional current flow due to the laser. They are calculated using the Schottky diode equation including the additional V_{PTE} term as in Equation 5.2, which is derived as follows. The photocurrent due to the PTE effect (I_{PC}) can be described as $I_{PC} = I_{Total} - I_{Dark}$

where $I_{Total} = I_{Dark} + I_{PC}$ and I_{Dark} is the current measured when the laser is turned off.

$$\begin{aligned}
I_{Total} &= \left\{ I_0 \left[\exp\left(\frac{qV_a}{kT}\right) - 1 \right] \right\} \exp\left(\frac{qV_{PTE}}{kT}\right) \text{ where } I_0 = AA_G T^2 \exp\left(\frac{-q\phi_B}{kT}\right) \\
I_{PC} &= \left\{ I_0 \left[\exp\left(\frac{qV_a}{kT}\right) - 1 \right] \right\} \exp\left(\frac{qV_{PTE}}{kT}\right) - I_0 \left[\exp\left(\frac{qV_a}{kT}\right) - 1 \right] \\
&= \left\{ I_0 \left[\exp\left(\frac{qV_a}{kT}\right) - 1 \right] \right\} \left[\exp\left(\frac{qV_{PTE}}{kT}\right) - 1 \right] = I_{Dark} \left[\exp\left(\frac{qV_{PTE}}{kT}\right) - 1 \right] \\
\therefore V_{PTE} &= \frac{kT}{q} \log\left(\frac{I_{PC}}{I_{Dark}} + 1\right) \dots (5.2)
\end{aligned}$$

where q is electron charge, V_a is an effective voltage applied on a junction, k is Boltzmann's constant, T is 300 K, A is junction area, A_G is Richardson constant, and ϕ_B is the barrier height of a junction. Figure 5.6 shows the calculated V_{PTE} values in the applied bias range for the graphene-MoS₂ heterojunction and the Ti-MoS₂ junction, respectively. The estimated V_{PTE} values are 0.22–0.47 mV on the graphene-MoS₂ heterojunction and 31.8–37.9 mV on the Ti-MoS₂ junction. The big difference of the V_{PTE} values in each junction is attributed to the huge difference in thermal conductivities between graphene (~ 5000 W/mK) [155] and titanium (21.8 W/mK) [153]. For instance, when the laser illuminates the graphene-MoS₂ heterojunction area, the heat generated by the laser is quickly dissipated through the graphene sheet, and therefore the localized temperature ΔT becomes small. On the other hand, when the laser shines on the Ti-MoS₂ junction area, the heat generated by the laser is quite slowly dissipated compared with the graphene case, and therefore the localized temperature ΔT is much bigger than the case of graphene-MoS₂ heterojunction. Using Equation 5.1, the estimated temperature increases are ~ 0.7 K for the graphene-MoS₂ heterojunction and ~ 50 K for the Ti-MoS₂ junction with the

0.43 mW laser.

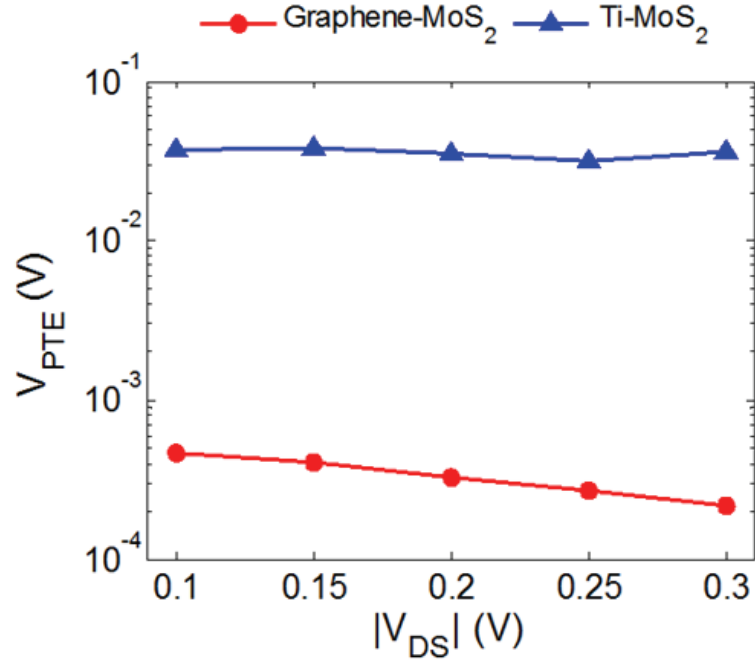


Figure 5.6: Photothermal voltages generated at each junction by the photothermal electric (PTE) effect with the applied V_{DS} from 0.1 V to 0.3 V for the graphene-MoS₂ heterojunction and from -0.1 V to -0.3 V for the Ti-MoS₂ junction, respectively.

The slight decrease in V_{PTE} in the graphene-MoS₂ by increasing V_{DS} is attributed to the changing of the Seebeck coefficient, which has the energy dependency of the conductivity by the Mott relation [148, 149, 154, 156].

$$S = -\frac{\pi^2 k^2 T}{3q} \frac{1}{\sigma} \frac{d\sigma}{dE} \Big|_{E=E_F} \quad \dots (5.3)$$

where k is Boltzmann's constant, T is temperature, q is electron charge, σ is conductance, and E is electrical potential energy. Referring to Figure 5.3, the conductivity of the device increases faster in the positive V_{DS} region where the

conductivity is dominated by the graphene-MoS₂ junction barrier, compared to the conductivity changes in the negative V_{DS} region where the Ti-MoS₂ junction barrier dominates. By the Mott relation, the increasing conductivity results in the decreasing Seebeck coefficient. As a result, the difference in the Seebeck coefficients between graphene and MoS₂ decreases as the bias increases and thus the voltage generation is reduced.

5.5.2 Photocurrent gain by PTE effect

The photocurrent gain of the heterojunction by the PTE effect is estimated to be 49.8 nA/K at V_{DS} = 0.3 V using Equation 5.4, which is derived as follows. From Equation 5.2:

$$I_{PC} = I_{Dark} \left[\exp\left(\frac{qV_{PTE}}{kT}\right) - 1 \right]$$

$$\frac{dI_{PC}}{dV_{PTE}} = I_{Dark} \frac{q}{kT} \exp\left(\frac{qV_{PTE}}{kT}\right) = I_{Dark} \frac{q}{kT} \left(\frac{I_{PC}}{I_{Dark}} + 1 \right)$$

$$= \frac{q}{kT} (I_{PC} + I_{Dark}) = \frac{q}{kT} (I_{Total})$$

Using Equation 5.1, $V_{PTE} = (S_{Graphene} - S_{MoS_2})\Delta T$ or $\frac{dV_{PTE}}{d\Delta T} = (S_{Graphene} - S_{MoS_2})$, it becomes as follows:

$$\frac{dI_{PC}}{d\Delta T} = \frac{dI_{PC}}{dV_{PTE}} \frac{dV_{PTE}}{d\Delta T} = \frac{q}{kT} (I_{PC} + I_{Dark}) (S_{Graphene} - S_{MoS_2})$$

$$\therefore \frac{dI_{PC}}{d\Delta T} = \frac{q}{kT} (I_{PC} + I_{Dark}) \Delta S \dots (5.4)$$

where q is electron charge, k is Boltzmann's constant, T is 300 K, I_{PC} is the photocurrent, I_{Dark} is the current measured when the laser is turned off, ΔS is the

difference in the Seebeck coefficients of graphene and MoS₂, respectively, and ΔT is the local temperature increase at the junction by laser irradiation.

The photocurrent gain (Equation 5.5) depends exponentially on the difference in the Seebeck coefficients between the two materials for a fixed laser power (ΔT constant). From Equations 5.1 and 5.2,

$$V_{PTE} = (S_{Graphene} - S_{MoS_2})\Delta T = \frac{kT}{q} \log \left(\frac{I_{PC}}{I_{Dark}} + 1 \right)$$

$$\left(\frac{q}{kT} \right) \Delta S \Delta T = \log \left(\frac{I_{PC}}{I_{Dark}} + 1 \right)$$

$$I_{PC} = I_{Dark} \times \left(e^{\frac{q}{kT} \Delta S \Delta T} - 1 \right)$$

$$\therefore \frac{I_{PC}}{I_{Dark}} \equiv Gain = \left(e^{\frac{q}{kT} \Delta S \Delta T} - 1 \right) \dots (5.5)$$

where q is electron charge, k is Boltzmann's constant, T is 300 K, I_{PC} is the photocurrent, I_{Dark} is the current measured when the laser is turned off, ΔS is the difference in the Seebeck coefficients between graphene and MoS₂, and ΔT is the local temperature increase at the junction by laser irradiation. As a result, a heterojunction device with graphene and monolayer MoS₂ ($-S_{MoS_2}$ is on the order of $10^4 \mu V/K$ [149, 157]) can possibly be a photodetector with a significantly higher gain than the heterojunction device with the multilayer MoS₂ ($-S_{MoS_2} \sim 7 \times 10^2 \mu V/K$). Furthermore, by thermally isolating the graphene absorption region it should be possible to increase the temperature gradient.

5.6 Summary

In this chapter, graphene-MoS₂ heterojunction transistors were designed and fabricated to study the photoresponse mechanism on the junction area. Using an 800 nm wavelength of a raster scanning laser with 0.43 mW power, the device showed photoresponses of 0.019 mA/W and 0.032 mA/W on the graphene-MoS₂ heterojunction area and the Ti-MoS₂ junction area, respectively, in the thermal equilibrium condition; and the photoresponses increase to 0.139 mA/W and 0.457 mA/W, respectively, when a bias is applied. Because of the ultrafast recombination time of graphene and the huge difference in the Seebeck coefficients between graphene and MoS₂, the photoresponse of the graphene-MoS₂ junction is due to the photothermal voltage generated by PTE effect across the graphene-MoS₂ heterojunction area, which was determined to be between 0.22–0.47 mV. The large transfer length about 14 μm from the heterojunction edge opens a possibility of making a large area photodetector. The photocurrent gain depends exponentially on the material Seebeck coefficients being different at the junction. As a result, a higher-gain graphene-MoS₂ heterojunction photodetector can be achieved with monolayer MoS₂ that has a Seebeck coefficient about two orders of magnitude higher than that of multilayer MoS₂. By proper thermal isolation it should be possible to achieve a higher thermal gradient providing additional current gain.

CHAPTER 6

SUMMARY

In this thesis, graphene-molybdenum disulfide (MoS_2) heterojunction devices were explored in terms of electrical and optical properties. Chapter 1 introduced atomically thin two-dimensional (2D) layered materials; especially, graphene and MoS_2 , which are two representative 2D materials and the main sources of this work. Chapter 2 and 3 provided necessary preparation steps for the research. Transfer, characterization, and fabrication processes of the 2D materials were described. Chapter 4 and 5 presented the measurement results on the graphene- MoS_2 heterojunction devices. Together, all these chapters investigated two main goals; electrical characteristics and optical characteristics of the heterojunction devices.

In terms of the electrical characteristics, some of the findings include: (1) an asymmetry IV curve due to the variation of the barrier heights of the two contacts, (2) Schottky barrier height extraction for the heterojunction, (3) thermionic-field emission as the charge transport mechanism at the junction in a low bias region, (4) presence of two donor levels in the exfoliated MoS_2 , and (5) barrier height lowering at the heterojunction due to charge transfer from MoS_2 to graphene.

In terms of the optical characteristics, some of the findings include: (1) photothermal electric (PTE) effect as the dominant mechanism for photoresponse in the heterojunction, (2) photocurrent induced by PTE-generated photothermal voltage, and (3) photocurrent gain depending exponentially on the product of the Seebeck

coefficient difference and the light induced temperature gradient.

Although in this work the graphene-MoS₂ heterojunction device is explored as one example of the 2D heterojunction devices, these studies may well be extrapolated to let us understand electrical and optical behaviors of other graphene and transition metal dichalcogenides (TMDC) 2D heterostructures. This work has provided some basic information necessary to properly design practical heterojunction devices for various applications.

BIBLIOGRAPHY

- [1] P. R. Wallace, "The band theory of graphite," *Physical Review*, vol. 71, p. 622, 1947.
- [2] K. S. Novoselov, A. K. Geim, S. Morozov, D. Jiang, Y. Zhang, S. Dubonos, *et al.*, "Electric field effect in atomically thin carbon films," *science*, vol. 306, pp. 666-669, 2004.
- [3] A. Geim and I. Grigorieva, "Van der Waals heterostructures," *Nature*, vol. 499, pp. 419-425, 2013.
- [4] K. I. Bolotin, K. Sikes, Z. Jiang, M. Klima, G. Fudenberg, J. Hone, *et al.*, "Ultrahigh electron mobility in suspended graphene," *Solid State Communications*, vol. 146, pp. 351-355, 2008.
- [5] B. Radisavljevic, A. Radenovic, J. Brivio, V. Giacometti, and A. Kis, "Single-layer MoS₂ transistors," *Nature nanotechnology*, vol. 6, pp. 147-150, 2011.
- [6] D. R. Cooper, B. D'Anjou, N. Ghattamaneni, B. Harack, M. Hilke, A. Horth, *et al.*, "Experimental review of graphene," *International Scholarly Research Notices*, vol. 2012, 2012.
- [7] A. Kuc, N. Zibouche, and T. Heine, "Influence of quantum confinement on the electronic structure of the transition metal sulfide T S 2," *Physical Review B*, vol. 83, p. 245213, 2011.
- [8] K. F. Mak, C. Lee, J. Hone, J. Shan, and T. F. Heinz, "Atomically thin MoS₂: a new direct-gap semiconductor," *Physical Review Letters*, vol. 105, p. 136805, 2010.
- [9] A. Splendiani, L. Sun, Y. Zhang, T. Li, J. Kim, C.-Y. Chim, *et al.*, "Emerging photoluminescence in monolayer MoS₂," *Nano letters*, vol. 10, pp. 1271-1275, 2010.
- [10] O. Lopez-Sanchez, E. Alarcon Llado, V. Koman, A. Fontcuberta i Morral, A. Radenovic, and A. Kis, "Light Generation and Harvesting in a van der Waals Heterostructure," *ACS nano*, vol. 8, pp. 3042-3048, 2014.
- [11] R. Sundaram, M. Engel, A. Lombardo, R. Krupke, A. Ferrari, P. Avouris, *et al.*, "Electroluminescence in single layer MoS₂," *Nano letters*, vol. 13, pp. 1416-1421, 2013.
- [12] P. Miró, M. Audiffred, and T. Heine, "An atlas of two-dimensional materials," *Chemical Society Reviews*, vol. 43, pp. 6537-6554, 2014.

- [13] C. Dean, A. Young, I. Meric, C. Lee, L. Wang, S. Sorgenfrei, *et al.*, "Boron nitride substrates for high-quality graphene electronics," *Nature nanotechnology*, vol. 5, pp. 722-726, 2010.
- [14] J.-H. Chen, C. Jang, S. Xiao, M. Ishigami, and M. S. Fuhrer, "Intrinsic and extrinsic performance limits of graphene devices on SiO₂," *Nature nanotechnology*, vol. 3, pp. 206-209, 2008.
- [15] A. K. Geim and K. S. Novoselov, "The rise of graphene," *Nature materials*, vol. 6, pp. 183-191, 2007.
- [16] D. Jena and A. Konar, "Enhancement of carrier mobility in semiconductor nanostructures by dielectric engineering," *Physical review letters*, vol. 98, p. 136805, 2007.
- [17] R. Nair, P. Blake, A. Grigorenko, K. Novoselov, T. Booth, T. Stauber, *et al.*, "Fine structure constant defines visual transparency of graphene," *Science*, vol. 320, pp. 1308-1308, 2008.
- [18] F. Bonaccorso, Z. Sun, T. Hasan, and A. Ferrari, "Graphene photonics and optoelectronics," *Nature photonics*, vol. 4, pp. 611-622, 2010.
- [19] W. Choi, M. Y. Cho, A. Konar, J. H. Lee, G. B. Cha, S. C. Hong, *et al.*, "High-detectivity multilayer MoS₂ phototransistors with spectral response from ultraviolet to infrared," *Advanced Materials*, vol. 24, pp. 5832-5836, 2012.
- [20] X. Li, W. Cai, J. An, S. Kim, J. Nah, D. Yang, *et al.*, "Large-area synthesis of high-quality and uniform graphene films on copper foils," *Science*, vol. 324, pp. 1312-1314, 2009.
- [21] L. Liu, H. Zhou, R. Cheng, W. J. Yu, Y. Liu, Y. Chen, *et al.*, "High-yield chemical vapor deposition growth of high-quality large-area AB-stacked bilayer graphene," *Acs Nano*, vol. 6, pp. 8241-8249, 2012.
- [22] A. Reina, X. Jia, J. Ho, D. Nezich, H. Son, V. Bulovic, *et al.*, "Large area, few-layer graphene films on arbitrary substrates by chemical vapor deposition," *Nano letters*, vol. 9, pp. 30-35, 2008.
- [23] C. Mattevi, H. Kim, and M. Chhowalla, "A review of chemical vapour deposition of graphene on copper," *Journal of Materials Chemistry*, vol. 21, pp. 3324-3334, 2011.

- [24] J. Hwang, M. Kim, V. B. Shields, and M. G. Spencer, "CVD growth of SiC on sapphire substrate and graphene formation from the epitaxial SiC," *Journal of Crystal Growth*, vol. 366, pp. 26-30, 2013.
- [25] J. Hwang, M. Kim, D. Campbell, H. A. Alsalman, J. Y. Kwak, S. Shivaraman, *et al.*, "Van der Waals epitaxial growth of graphene on sapphire by chemical vapor deposition without a metal catalyst," *Acs Nano*, vol. 7, pp. 385-395, 2012.
- [26] H. Bi, S. Sun, F. Huang, X. Xie, and M. Jiang, "Direct growth of few-layer graphene films on SiO₂ substrates and their photovoltaic applications," *Journal of Materials Chemistry*, vol. 22, pp. 411-416, 2012.
- [27] K.-K. Liu, W. Zhang, Y.-H. Lee, Y.-C. Lin, M.-T. Chang, C.-Y. Su, *et al.*, "Growth of large-area and highly crystalline MoS₂ thin layers on insulating substrates," *Nano letters*, vol. 12, pp. 1538-1544, 2012.
- [28] Y. Zhan, Z. Liu, S. Najmaei, P. M. Ajayan, and J. Lou, "Large-Area Vapor-Phase Growth and Characterization of MoS₂ Atomic Layers on a SiO₂ Substrate," *Small*, vol. 8, pp. 966-971, 2012.
- [29] J. Jeon, S. K. Jang, S. M. Jeon, G. Yoo, Y. H. Jang, J.-H. Park, *et al.*, "Layer-controlled CVD growth of large-area two-dimensional MoS₂ films," *Nanoscale*, vol. 7, pp. 1688-1695, 2015.
- [30] S. Najmaei, Z. Liu, W. Zhou, X. Zou, G. Shi, S. Lei, *et al.*, "Vapour phase growth and grain boundary structure of molybdenum disulphide atomic layers," *Nature materials*, vol. 12, pp. 754-759, 2013.
- [31] S. Wang, Y. Rong, Y. Fan, M. Pacios, H. Bhaskaran, K. He, *et al.*, "Shape Evolution of Monolayer MoS₂ Crystals Grown by Chemical Vapor Deposition," *Chemistry of Materials*, vol. 26, pp. 6371-6379, 2014.
- [32] N. Srivastava, G. He, R. M. Feenstra, and P. Fisher, "Comparison of graphene formation on C-face and Si-face SiC {0001} surfaces," *Physical Review B*, vol. 82, p. 235406, 2010.
- [33] G. G. Jernigan, B. L. VanMil, J. L. Tedesco, J. G. Tischler, E. R. Glaser, A. Davidson III, *et al.*, "Comparison of epitaxial graphene on Si-face and C-face 4H SiC formed by ultrahigh vacuum and RF furnace production," *Nano letters*, vol. 9, pp. 2605-2609, 2009.
- [34] C. Riedl, C. Coletti, T. Iwasaki, A. Zakharov, and U. Starke, "Quasi-free-standing epitaxial graphene on SiC obtained by hydrogen intercalation," *Physical review letters*, vol. 103, p. 246804, 2009.

- [35] Y.-M. Lin, A. Valdes-Garcia, S.-J. Han, D. B. Farmer, I. Meric, Y. Sun, *et al.*, "Wafer-scale graphene integrated circuit," *Science*, vol. 332, pp. 1294-1297, 2011.
- [36] S. Lee, K. Lee, C.-H. Liu, G. S. Kulkarni, and Z. Zhong, "Flexible and transparent all-graphene circuits for quaternary digital modulations," *Nature communications*, vol. 3, p. 1018, 2012.
- [37] H. Wang, D. Nezich, J. Kong, and T. Palacios, "Graphene frequency multipliers," *Electron Device Letters, IEEE*, vol. 30, pp. 547-549, 2009.
- [38] H. Wang, A. Hsu, J. Wu, J. Kong, and T. Palacios, "Graphene-based ambipolar RF mixers," *Electron Device Letters, IEEE*, vol. 31, pp. 906-908, 2010.
- [39] Y. Wu, K. A. Jenkins, A. Valdes-Garcia, D. B. Farmer, Y. Zhu, A. A. Bol, *et al.*, "State-of-the-art graphene high-frequency electronics," *Nano Letters*, vol. 12, pp. 3062-3067, 2012.
- [40] Y.-M. Lin, C. Dimitrakopoulos, K. A. Jenkins, D. B. Farmer, H.-Y. Chiu, A. Grill, *et al.*, "100-GHz transistors from wafer-scale epitaxial graphene," *Science*, vol. 327, pp. 662-662, 2010.
- [41] Y. Wu, Y.-m. Lin, A. A. Bol, K. A. Jenkins, F. Xia, D. B. Farmer, *et al.*, "High-frequency, scaled graphene transistors on diamond-like carbon," *Nature*, vol. 472, pp. 74-78, 2011.
- [42] S. Bae, H. Kim, Y. Lee, X. Xu, J.-S. Park, Y. Zheng, *et al.*, "Roll-to-roll production of 30-inch graphene films for transparent electrodes," *Nature nanotechnology*, vol. 5, pp. 574-578, 2010.
- [43] K. S. Kim, Y. Zhao, H. Jang, S. Y. Lee, J. M. Kim, K. S. Kim, *et al.*, "Large-scale pattern growth of graphene films for stretchable transparent electrodes," *Nature*, vol. 457, pp. 706-710, 2009.
- [44] D. Kuzum, H. Takano, E. Shim, J. C. Reed, H. Juul, A. G. Richardson, *et al.*, "Transparent and flexible low noise graphene electrodes for simultaneous electrophysiology and neuroimaging," *Nature communications*, vol. 5, 2014.
- [45] L. Gomez De Arco, Y. Zhang, C. W. Schlenker, K. Ryu, M. E. Thompson, and C. Zhou, "Continuous, highly flexible, and transparent graphene films by chemical vapor deposition for organic photovoltaics," *ACS nano*, vol. 4, pp. 2865-2873, 2010.

- [46] A. C. Ferrari, F. Bonaccorso, V. Falko, K. S. Novoselov, S. Roche, P. Bøggild, *et al.*, "Science and technology roadmap for graphene, related two-dimensional crystals, and hybrid systems," *Nanoscale*, 2014.
- [47] G. Fiori, F. Bonaccorso, G. Iannaccone, T. Palacios, D. Neumaier, A. Seabaugh, *et al.*, "Electronics based on two-dimensional materials," *Nature nanotechnology*, vol. 9, pp. 768-779, 2014.
- [48] H. Wang, L. Yu, Y.-H. Lee, Y. Shi, A. Hsu, M. L. Chin, *et al.*, "Integrated circuits based on bilayer MoS₂ transistors," *Nano letters*, vol. 12, pp. 4674-4680, 2012.
- [49] B. Radisavljevic, M. B. Whitwick, and A. Kis, "Integrated circuits and logic operations based on single-layer MoS₂," *ACS nano*, vol. 5, pp. 9934-9938, 2011.
- [50] R. Cheng, S. Jiang, Y. Chen, Y. Liu, N. Weiss, H.-C. Cheng, *et al.*, "Few-layer molybdenum disulfide transistors and circuits for high-speed flexible electronics," *Nature communications*, vol. 5, 2014.
- [51] G.-H. Lee, Y.-J. Yu, X. Cui, N. Petrone, C.-H. Lee, M. S. Choi, *et al.*, "Flexible and transparent MoS₂ field-effect transistors on hexagonal boron nitride-graphene heterostructures," *ACS nano*, vol. 7, pp. 7931-7936, 2013.
- [52] O. Lopez-Sanchez, D. Lembke, M. Kayci, A. Radenovic, and A. Kis, "Ultrasensitive photodetectors based on monolayer MoS₂," *Nature nanotechnology*, vol. 8, pp. 497-501, 2013.
- [53] S. Alkis, T. Öztaş, L. Aygün, F. Bozkurt, A. Okyay, and B. Ortaç, "Thin film MoS₂ nanocrystal based ultraviolet photodetector," *Optics express*, vol. 20, pp. 21815-21820, 2012.
- [54] M. Shanmugam, C. A. Durcan, and B. Yu, "Layered semiconductor molybdenum disulfide nanomembrane based Schottky-barrier solar cells," *Nanoscale*, vol. 4, pp. 7399-7405, 2012.
- [55] F. Koppens, T. Mueller, P. Avouris, A. Ferrari, M. Vitiello, and M. Polini, "Photodetectors based on graphene, other two-dimensional materials and hybrid systems," *Nature nanotechnology*, vol. 9, pp. 780-793, 2014.
- [56] Y. Hao, M. Bharathi, L. Wang, Y. Liu, H. Chen, S. Nie, *et al.*, "The role of surface oxygen in the growth of large single-crystal graphene on copper," *Science*, vol. 342, pp. 720-723, 2013.

- [57] S. Lee, K. Lee, and Z. Zhong, "Wafer scale homogeneous bilayer graphene films by chemical vapor deposition," *Nano letters*, vol. 10, pp. 4702-4707, 2010.
- [58] Z.-J. Wang, G. Weinberg, Q. Zhang, T. Lunkenbein, A. Klein-Hoffmann, M. Kurnatowska, *et al.*, "Direct Observation of Graphene Growth and Associated Copper Substrate Dynamics by In-Situ Scanning Electron Microscopy," *ACS nano*, 2015.
- [59] Q. H. Wang, K. Kalantar-Zadeh, A. Kis, J. N. Coleman, and M. S. Strano, "Electronics and optoelectronics of two-dimensional transition metal dichalcogenides," *Nature nanotechnology*, vol. 7, pp. 699-712, 2012.
- [60] A. C. Ferrari and D. M. Basko, "Raman spectroscopy as a versatile tool for studying the properties of graphene," *Nature nanotechnology*, vol. 8, pp. 235-246, 2013.
- [61] L. Malard, M. Pimenta, G. Dresselhaus, and M. Dresselhaus, "Raman spectroscopy in graphene," *Physics Reports*, vol. 473, pp. 51-87, 2009.
- [62] C. Lee, H. Yan, L. E. Brus, T. F. Heinz, J. Hone, and S. Ryu, "Anomalous lattice vibrations of single-and few-layer MoS₂," *ACS nano*, vol. 4, pp. 2695-2700, 2010.
- [63] S. Han, H. Kwon, S. K. Kim, S. Ryu, W. S. Yun, D. Kim, *et al.*, "Band-gap transition induced by interlayer van der Waals interaction in MoS₂," *Physical Review B*, vol. 84, p. 045409, 2011.
- [64] D. Ricci and P. C. Braga, "Recognizing and avoiding artifacts in AFM imaging," in *Atomic Force Microscopy*, ed: Springer, 2004, pp. 25-37.
- [65] P. Y. Huang, C. S. Ruiz-Vargas, A. M. van der Zande, W. S. Whitney, M. P. Levendorf, J. W. Kevek, *et al.*, "Grains and grain boundaries in single-layer graphene atomic patchwork quilts," *Nature*, vol. 469, pp. 389-392, 2011.
- [66] A. M. van der Zande, P. Y. Huang, D. A. Chenet, T. C. Berkelbach, Y. You, G.-H. Lee, *et al.*, "Grains and grain boundaries in highly crystalline monolayer molybdenum disulphide," *Nature materials*, vol. 12, pp. 554-561, 2013.
- [67] Y. Hernandez, V. Nicolosi, M. Lotya, F. M. Blighe, Z. Sun, S. De, *et al.*, "High-yield production of graphene by liquid-phase exfoliation of graphite," *Nature nanotechnology*, vol. 3, pp. 563-568, 2008.

- [68] J. C. Meyer, A. K. Geim, M. Katsnelson, K. Novoselov, T. Booth, and S. Roth, "The structure of suspended graphene sheets," *Nature*, vol. 446, pp. 60-63, 2007.
- [69] P. Blake, E. Hill, A. C. Neto, K. Novoselov, D. Jiang, R. Yang, *et al.*, "Making graphene visible," *Applied Physics Letters*, vol. 91, p. 063124, 2007.
- [70] S. Roddaro, P. Pingue, V. Piazza, V. Pellegrini, and F. Beltram, "The optical visibility of graphene: Interference colors of ultrathin graphite on SiO₂," *Nano letters*, vol. 7, pp. 2707-2710, 2007.
- [71] W. Ouyang, X.-Z. Liu, Q. Li, Y. Zhang, J. Yang, and Q.-s. Zheng, "Optical methods for determining thicknesses of few-layer graphene flakes," *Nanotechnology*, vol. 24, p. 505701, 2013.
- [72] Z. Ni, H. Wang, J. Kasim, H. Fan, T. Yu, Y. Wu, *et al.*, "Graphene thickness determination using reflection and contrast spectroscopy," *Nano letters*, vol. 7, pp. 2758-2763, 2007.
- [73] H. Li, Q. Zhang, C. C. R. Yap, B. K. Tay, T. H. T. Edwin, A. Olivier, *et al.*, "From bulk to monolayer MoS₂: evolution of Raman scattering," *Advanced Functional Materials*, vol. 22, pp. 1385-1390, 2012.
- [74] S. Shivaraman, M. Chandrashekar, J. J. Boeckl, and M. G. Spencer, "Thickness estimation of epitaxial graphene on SiC using attenuation of substrate raman intensity," *Journal of electronic materials*, vol. 38, pp. 725-730, 2009.
- [75] M. Bernardi, M. Palumbo, and J. C. Grossman, "Extraordinary sunlight absorption and one nanometer thick photovoltaics using two-dimensional monolayer materials," *Nano letters*, vol. 13, pp. 3664-3670, 2013.
- [76] A. Zurutuza and C. Marinelli, "Challenges and opportunities in graphene commercialization," *Nature nanotechnology*, vol. 9, pp. 730-734, 2014.
- [77] C. Logofatu, C. C. Negri, R. V. Ghita, F. Ungureanu, C. Cotirlan, C. G. A. S. Manea, *et al.*, "Study of SiO₂/Si Interface by Surface Techniques," *Crystalline silicon—properties and uses*, ed. by S. Basu (InTech, Croatia, 2011), pp. 23-42, 2011.
- [78] L. Liao, J. Bai, Y. Qu, Y.-c. Lin, Y. Li, Y. Huang, *et al.*, "High-κ oxide nanoribbons as gate dielectrics for high mobility top-gated graphene transistors," *Proceedings of the national academy of sciences*, vol. 107, pp. 6711-6715, 2010.

- [79] L. Liao, J. Bai, R. Cheng, Y.-C. Lin, S. Jiang, Y. Huang, *et al.*, "Top-gated graphene nanoribbon transistors with ultrathin high-k dielectrics," *Nano letters*, vol. 10, pp. 1917-1921, 2010.
- [80] V. Georgakilas, M. Otyepka, A. B. Bourlinos, V. Chandra, N. Kim, K. C. Kemp, *et al.*, "Functionalization of graphene: covalent and non-covalent approaches, derivatives and applications," *Chemical reviews*, vol. 112, pp. 6156-6214, 2012.
- [81] Z. H. Ni, H. M. Wang, Y. Ma, J. Kasim, Y. H. Wu, and Z. X. Shen, "Tunable stress and controlled thickness modification in graphene by annealing," *ACS nano*, vol. 2, pp. 1033-1039, 2008.
- [82] D. B. Farmer and R. G. Gordon, "Atomic layer deposition on suspended single-walled carbon nanotubes via gas-phase noncovalent functionalization," *Nano letters*, vol. 6, pp. 699-703, 2006.
- [83] B. Lee, S.-Y. Park, H.-C. Kim, K. Cho, E. M. Vogel, M. J. Kim, *et al.*, "Conformal Al₂O₃ dielectric layer deposited by atomic layer deposition for graphene-based nanoelectronics," *Applied Physics Letters*, vol. 92, p. 203102, 2008.
- [84] Y.-M. Lin, K. A. Jenkins, A. Valdes-Garcia, J. P. Small, D. B. Farmer, and P. Avouris, "Operation of graphene transistors at gigahertz frequencies," *Nano letters*, vol. 9, pp. 422-426, 2008.
- [85] S. Kim, J. Nah, I. Jo, D. Shahrjerdi, L. Colombo, Z. Yao, *et al.*, "Realization of a high mobility dual-gated graphene field-effect transistor with Al₂O₃ dielectric," *Applied Physics Letters*, vol. 94, pp. 062107-062107-3, 2009.
- [86] L. Liao and X. Duan, "Graphene–dielectric integration for graphene transistors," *Materials Science and Engineering: R: Reports*, vol. 70, pp. 354-370, 2010.
- [87] M. Wang, S. K. Jang, W. J. Jang, M. Kim, S. Y. Park, S. W. Kim, *et al.*, "A Platform for Large-Scale Graphene Electronics—CVD Growth of Single-Layer Graphene on CVD-Grown Hexagonal Boron Nitride," *Advanced Materials*, vol. 25, pp. 2746-2752, 2013.
- [88] S. Roth, F. Matsui, T. Greber, and J. Osterwalder, "Chemical vapor deposition and characterization of aligned and incommensurate graphene/hexagonal boron nitride heterostack on Cu (111)," *Nano letters*, vol. 13, pp. 2668-2675, 2013.

- [89] Z. Liu, L. Song, S. Zhao, J. Huang, L. Ma, J. Zhang, *et al.*, "Direct growth of graphene/hexagonal boron nitride stacked layers," *Nano letters*, vol. 11, pp. 2032-2037, 2011.
- [90] S.-J. Han, Z. Chen, A. A. Bol, and Y. Sun, "Channel-length-dependent transport behaviors of graphene field-effect transistors," *Electron Device Letters, IEEE*, vol. 32, pp. 812-814, 2011.
- [91] J. Bai, L. Liao, H. Zhou, R. Cheng, L. Liu, Y. Huang, *et al.*, "Top-gated chemical vapor deposition grown graphene transistors with current saturation," *Nano letters*, vol. 11, pp. 2555-2559, 2011.
- [92] S. Adam, E. Hwang, V. Galitski, and S. D. Sarma, "A self-consistent theory for graphene transport," *Proceedings of the National Academy of Sciences*, vol. 104, pp. 18392-18397, 2007.
- [93] J. Martin, N. Akerman, G. Ulbricht, T. Lohmann, J. Smet, K. Von Klitzing, *et al.*, "Observation of electron-hole puddles in graphene using a scanning single-electron transistor," *Nature Physics*, vol. 4, pp. 144-148, 2008.
- [94] J. Xia, F. Chen, J. Li, and N. Tao, "Measurement of the quantum capacitance of graphene," *Nature nanotechnology*, vol. 4, pp. 505-509, 2009.
- [95] J. Lee, H.-J. Chung, D. H. Seo, J. Lee, H. Shin, S. Seo, *et al.*, "Is quantum capacitance in graphene a potential hurdle for device scaling?," *Nano Research*, vol. 7, pp. 1-9, 2014.
- [96] K. Novoselov, D. Jiang, F. Schedin, T. Booth, V. Khotkevich, S. Morozov, *et al.*, "Two-dimensional atomic crystals," *Proceedings of the National Academy of Sciences of the United States of America*, vol. 102, pp. 10451-10453, 2005.
- [97] K. S. Novoselov, V. Fal, L. Colombo, P. Gellert, M. Schwab, and K. Kim, "A roadmap for graphene," *Nature*, vol. 490, pp. 192-200, 2012.
- [98] I. Meric, M. Y. Han, A. F. Young, B. Ozyilmaz, P. Kim, and K. L. Shepard, "Current saturation in zero-bandgap, top-gated graphene field-effect transistors," *Nature nanotechnology*, vol. 3, pp. 654-659, 2008.
- [99] C. Lee, X. Wei, J. W. Kysar, and J. Hone, "Measurement of the elastic properties and intrinsic strength of monolayer graphene," *science*, vol. 321, pp. 385-388, 2008.
- [100] L. Britnell, R. V. Gorbachev, R. Jalil, B. D. Belle, F. Schedin, M. I. Katsnelson, *et al.*, "Electron tunneling through ultrathin boron nitride crystalline barriers," *Nano letters*, vol. 12, pp. 1707-1710, 2012.

- [101] L. Britnell, R. Gorbachev, R. Jalil, B. Belle, F. Schedin, A. Mishchenko, *et al.*, "Field-effect tunneling transistor based on vertical graphene heterostructures," *Science*, vol. 335, pp. 947-950, 2012.
- [102] F. Amet, J. Williams, A. Garcia, M. Yankowitz, K. Watanabe, T. Taniguchi, *et al.*, "Tunneling spectroscopy of graphene-boron-nitride heterostructures," *Physical Review B*, vol. 85, p. 073405, 2012.
- [103] W. J. Yu, Z. Li, H. Zhou, Y. Chen, Y. Wang, Y. Huang, *et al.*, "Vertically stacked multi-heterostructures of layered materials for logic transistors and complementary inverters," *Nature materials*, vol. 12, pp. 246-252, 2013.
- [104] N. Myoung, K. Seo, S. J. Lee, and G. Ihm, "Large current modulation and spin-dependent tunneling of vertical graphene/mos2 heterostructures," *ACS nano*, vol. 7, pp. 7021-7027, 2013.
- [105] J. Kang, S. Tongay, J. Zhou, J. Li, and J. Wu, "Band offsets and heterostructures of two-dimensional semiconductors," *Applied Physics Letters*, vol. 102, p. 012111, 2013.
- [106] C.-C. Chen, C.-C. Chang, Z. Li, A. Levi, and S. B. Cronin, "Gate tunable graphene-silicon Ohmic/Schottky contacts," *Applied Physics Letters*, vol. 101, p. 223113, 2012.
- [107] H. Yang, J. Heo, S. Park, H. J. Song, D. H. Seo, K.-E. Byun, *et al.*, "Graphene barristor, a triode device with a gate-controlled Schottky barrier," *Science*, vol. 336, pp. 1140-1143, 2012.
- [108] C.-C. Chen, M. Aykol, C.-C. Chang, A. Levi, and S. B. Cronin, "Graphene-silicon Schottky diodes," *Nano letters*, vol. 11, pp. 1863-1867, 2011.
- [109] M. S. Choi, G.-H. Lee, Y.-J. Yu, D.-Y. Lee, S. H. Lee, P. Kim, *et al.*, "Controlled charge trapping by molybdenum disulphide and graphene in ultrathin heterostructured memory devices," *Nature communications*, vol. 4, p. 1624, 2013.
- [110] K. Roy, M. Padmanabhan, S. Goswami, T. P. Sai, G. Ramalingam, S. Raghavan, *et al.*, "Graphene-MoS2 hybrid structures for multifunctional photoresponsive memory devices," *Nature nanotechnology*, vol. 8, pp. 826-830, 2013.
- [111] S. Bertolazzi, D. Krasnozhan, and A. Kis, "Nonvolatile memory cells based on MoS2/graphene heterostructures," *ACS nano*, vol. 7, pp. 3246-3252, 2013.

- [112] W. J. Yu, Y. Liu, H. Zhou, A. Yin, Z. Li, Y. Huang, *et al.*, "Highly efficient gate-tunable photocurrent generation in vertical heterostructures of layered materials," *Nature nanotechnology*, vol. 8, pp. 952-958, 2013.
- [113] J. Y. Kwak, J. Hwang, M. Graham, H. Alsalman, N. Munoz, B. Calderon, *et al.*, "A high response MoS₂-graphene hetero-junction photodetector with broad spectral range," in *Device Research Conference (DRC), 2013 71st Annual*, 2013, pp. 1-2.
- [114] M. R. Esmaeili-Rad and S. Salahuddin, "High performance molybdenum disulfide amorphous silicon heterojunction photodetector," *Scientific reports*, vol. 3, 2013.
- [115] E. Dubois and G. Larrieu, "Measurement of low Schottky barrier heights applied to metallic source/drain metal-oxide-semiconductor field effect transistors," *Journal of applied physics*, vol. 96, pp. 729-737, 2004.
- [116] B. Sachs, L. Britnell, T. Wehling, A. Eckmann, R. Jalil, B. Belle, *et al.*, "Doping mechanisms in graphene-MoS₂ hybrids," *Applied Physics Letters*, vol. 103, p. 251607, 2013.
- [117] J. Y. Kwak, J. Hwang, B. Calderon, H. Alsalman, N. Munoz, B. Schutter, *et al.*, "Electrical Characteristics of Multilayer MoS₂ FET's with MoS₂/Graphene Heterojunction Contacts," *Nano letters*, vol. 14, pp. 4511-4516, 2014.
- [118] J. W. Suk, A. Kitt, C. W. Magnuson, Y. Hao, S. Ahmed, J. An, *et al.*, "Transfer of CVD-grown monolayer graphene onto arbitrary substrates," *ACS nano*, vol. 5, pp. 6916-6924, 2011.
- [119] A. Ferrari, J. Meyer, V. Scardaci, C. Casiraghi, M. Lazzeri, F. Mauri, *et al.*, "Raman spectrum of graphene and graphene layers," *Physical review letters*, vol. 97, p. 187401, 2006.
- [120] I. Calizo, I. Bejenari, M. Rahman, G. Liu, and A. A. Balandin, "Ultraviolet Raman microscopy of single and multilayer graphene," *Journal of Applied Physics*, vol. 106, pp. 043509-043509-5, 2009.
- [121] S. Kim, A. Konar, W.-S. Hwang, J. H. Lee, J. Lee, J. Yang, *et al.*, "High-mobility and low-power thin-film transistors based on multilayer MoS₂ crystals," *Nature communications*, vol. 3, p. 1011, 2012.
- [122] Y.-J. Yu, Y. Zhao, S. Ryu, L. E. Brus, K. S. Kim, and P. Kim, "Tuning the graphene work function by electric field effect," *Nano letters*, vol. 9, pp. 3430-3434, 2009.

- [123] G. Giovannetti, P. Khomyakov, G. Brocks, V. Karpan, J. Van den Brink, and P. Kelly, "Doping graphene with metal contacts," *Physical Review Letters*, vol. 101, p. 026803, 2008.
- [124] P. Khomyakov, G. Giovannetti, P. Rusu, G. Brocks, J. Van den Brink, and P. Kelly, "First-principles study of the interaction and charge transfer between graphene and metals," *Physical Review B*, vol. 79, p. 195425, 2009.
- [125] A. Padovani, L. Larcher, V. Della Marca, P. Pavan, H. Park, and G. Bersuker, "Charge trapping in alumina and its impact on the operation of metal-alumina-nitride-oxide-silicon memories: Experiments and simulations," *Journal of Applied Physics*, vol. 110, p. 014505, 2011.
- [126] J. Robertson and B. Falabretti, "Band offsets of high K gate oxides on high mobility semiconductors," *Materials Science and Engineering: B*, vol. 135, pp. 267-271, 2006.
- [127] K. Kaasbjerg, K. S. Thygesen, and A.-P. Jauho, "Acoustic phonon limited mobility in two-dimensional semiconductors: Deformation potential and piezoelectric scattering in monolayer MoS₂ from first principles," *Physical Review B*, vol. 87, p. 235312, 2013.
- [128] S. McDonnell, R. Addou, C. Buie, R. M. Wallace, and C. L. Hinkle, "Defect-dominated doping and contact resistance in MoS₂," *ACS nano*, vol. 8, pp. 2880-2888, 2014.
- [129] J. G. Champlain, "A first principles theoretical examination of graphene-based field effect transistors," *Journal of Applied Physics*, vol. 109, p. 084515, 2011.
- [130] F. Padovani and R. Stratton, "Field and thermionic-field emission in Schottky barriers," *Solid-State Electronics*, vol. 9, pp. 695-707, 1966.
- [131] S. Chand and J. Kumar, "Current transport in Pd₂Si/n-Si (100) Schottky barrier diodes at low temperatures," *Applied Physics A*, vol. 63, pp. 171-178, 1996.
- [132] S. Das, H.-Y. Chen, A. V. Penumatcha, and J. Appenzeller, "High performance multilayer MoS₂ transistors with scandium contacts," *Nano letters*, vol. 13, pp. 100-105, 2012.
- [133] A. V. Kretinin, Y. Cao, J.-S. Tu, G. Yu, R. Jalil, K. S. Novoselov, *et al.*, "Electronic properties of graphene encapsulated with different two-dimensional atomic crystals," *Nano letters*, vol. 14, pp. 3270-3276, 2014.

- [134] F. Schwierz, "Graphene transistors," *Nature nanotechnology*, vol. 5, pp. 487-496, 2010.
- [135] T. Georgiou, R. Jalil, B. D. Belle, L. Britnell, R. V. Gorbachev, S. V. Morozov, *et al.*, "Vertical field-effect transistor based on graphene-WS₂ heterostructures for flexible and transparent electronics," *Nature nanotechnology*, vol. 8, pp. 100-103, 2013.
- [136] Q. He, Z. Zeng, Z. Yin, H. Li, S. Wu, X. Huang, *et al.*, "Fabrication of Flexible MoS₂ Thin-Film Transistor Arrays for Practical Gas-Sensing Applications," *Small*, vol. 8, pp. 2994-2999, 2012.
- [137] Z. Yin, H. Li, H. Li, L. Jiang, Y. Shi, Y. Sun, *et al.*, "Single-layer MoS₂ phototransistors," *ACS nano*, vol. 6, pp. 74-80, 2011.
- [138] N. R. Pradhan, D. Rhodes, Y. Xin, S. Memaran, L. Bhaskaran, M. Siddiq, *et al.*, "Ambipolar Molybdenum Diselenide Field-Effect Transistors: Field-Effect and Hall Mobilities," *ACS nano*, vol. 8, pp. 7923-7929, 2014.
- [139] S. Fathipour, N. Ma, W. Hwang, V. Protasenko, S. Vishwanath, H. Xing, *et al.*, "Exfoliated multilayer MoTe₂ field-effect transistors," *Applied Physics Letters*, vol. 105, p. 192101, 2014.
- [140] M.-L. Tsai, S.-H. Su, J.-K. Chang, D.-S. Tsai, C.-H. Chen, C.-I. Wu, *et al.*, "Monolayer MoS₂ Heterojunction Solar Cells," *ACS nano*, vol. 8, pp. 8317-8322, 2014.
- [141] L. Britnell, R. Ribeiro, A. Eckmann, R. Jalil, B. Belle, A. Mishchenko, *et al.*, "Strong light-matter interactions in heterostructures of atomically thin films," *Science*, vol. 340, pp. 1311-1314, 2013.
- [142] W. Zhang, C.-P. Chuu, J.-K. Huang, C.-H. Chen, M.-L. Tsai, Y.-H. Chang, *et al.*, "Ultrahigh-gain photodetectors based on atomically thin graphene-MoS₂ heterostructures," *Scientific reports*, vol. 4, 2014.
- [143] X. Hong, J. Kim, S.-F. Shi, Y. Zhang, C. Jin, Y. Sun, *et al.*, "Ultrafast charge transfer in atomically thin MoS₂/WS₂ heterostructures," *Nature nanotechnology*, 2014.
- [144] R. Cheng, D. Li, H. Zhou, C. Wang, A. Yin, S. Jiang, *et al.*, "Electroluminescence and Photocurrent Generation from Atomically Sharp WSe₂/MoS₂ Heterojunction p-n Diodes," *Nano letters*, vol. 14, pp. 5590-5597, 2014.

- [145] M. M. Furchi, A. Pospischil, F. Libisch, J. Burgdörfer, and T. Mueller, "Photovoltaic effect in an electrically tunable van der Waals heterojunction," *Nano letters*, vol. 14, pp. 4785-4791, 2014.
- [146] P. A. George, J. Strait, J. Dawlaty, S. Shivaraman, M. Chandrashekar, F. Rana, *et al.*, "Ultrafast optical-pump terahertz-probe spectroscopy of the carrier relaxation and recombination dynamics in epitaxial graphene," *Nano letters*, vol. 8, pp. 4248-4251, 2008.
- [147] J. M. Dawlaty, S. Shivaraman, M. Chandrashekar, F. Rana, and M. G. Spencer, "Measurement of ultrafast carrier dynamics in epitaxial graphene," *Applied Physics Letters*, vol. 92, p. 042116, 2008.
- [148] M. Freitag, T. Low, F. Xia, and P. Avouris, "Photoconductivity of biased graphene," *Nature Photonics*, vol. 7, pp. 53-59, 2013.
- [149] M. Buscema, M. Barkelid, V. Zwiller, H. S. van der Zant, G. A. Steele, and A. Castellanos-Gomez, "Large and tunable photothermoelectric effect in single-layer MoS₂," *Nano letters*, vol. 13, pp. 358-363, 2013.
- [150] H. Xu, J. Wu, Q. Feng, N. Mao, C. Wang, and J. Zhang, "High responsivity and gate tunable graphene-MoS₂ hybrid phototransistor," *Small*, vol. 10, pp. 2300-2306, 2014.
- [151] S. Ghatak, A. N. Pal, and A. Ghosh, "Nature of electronic states in atomically thin MoS₂ field-effect transistors," *Acs Nano*, vol. 5, pp. 7707-7712, 2011.
- [152] N. M. Gabor, J. C. Song, Q. Ma, N. L. Nair, T. Taychatanapat, K. Watanabe, *et al.*, "Hot carrier-assisted intrinsic photoresponse in graphene," *Science*, vol. 334, pp. 648-652, 2011.
- [153] M. Ito, D. Setoyama, J. Matsunaga, H. Muta, K. Kurosaki, M. Uno, *et al.*, "Electrical and thermal properties of titanium hydrides," *Journal of alloys and compounds*, vol. 420, pp. 25-28, 2006.
- [154] Y. M. Zuev, W. Chang, and P. Kim, "Thermoelectric and magnetothermoelectric transport measurements of graphene," *Physical review letters*, vol. 102, p. 096807, 2009.
- [155] A. A. Balandin, S. Ghosh, W. Bao, I. Calizo, D. Teweldebrhan, F. Miao, *et al.*, "Superior thermal conductivity of single-layer graphene," *Nano letters*, vol. 8, pp. 902-907, 2008.

- [156] M. M. Furchi, D. K. Polyushkin, A. Pospischil, and T. Mueller, "Mechanisms of photoconductivity in atomically thin MoS₂," *Nano letters*, vol. 14, pp. 6165-6170, 2014.
- [157] J. Wu, H. Schmidt, K. K. Amara, X. Xu, G. Eda, and B. Özyilmaz, "Large Thermoelectricity via Variable Range Hopping in Chemical Vapor Deposition Grown Single-Layer MoS₂," *Nano letters*, vol. 14, pp. 2730-2734, 2014.